Dipl.-Ing. Jaromir Anatol Kotzurek

Structural anisotropy and lattice defects in submicrocrystalline metals studied by difference dilatometry and neutron scattering

DOCTORAL THESIS

to achieve the university degree of

Doktor der technischen Wissenschaften

submitted to

Graz University of Technology

Supervisor

Univ.-Prof. Dipl.-Ing. Dr.rer.nat Roland Würschum

Institute of Materials Physics

Graz, March 2017

"Synchronicity comes out of repeated coincidences at the lowest level. Further examination shows it is the utter power of the sheer number of coincidences that leads one to the idea that synchronicity is guided by something more than chance."

—The Thirty-Six Lessons of Vivec, Sermon Four

Kurzfassung

Mittels High-Pressure Torsion (HPT) Methode kann eine Metallscheibe per Torsion unter hohem Druck stark plastisch verformt werden. Das Ergebnis dieser Scherverformung ist eine ultrafeinkörnige Mikrostruktur mit hoher Defektdichte und ein mit diesen Defekten verbundenes hohes Überschussvolumen. Dieses Volumen ist ein wesentlicher Parameter für das Verständnis von Materialeigenschaften. Diese Arbeit erweitert frühere Differenzdilatometrieergebnisse an HPT-verformtem, hochreinem Nickel mit Dilatometriemessungen an Nickel verformt mit Equal-Channel Angular Pressing (ECAP), und versucht den Zusammenhang zwischen anisotropem Ausheilverhalten und anisotroper Mikrostruktur nach HPT und ECAP zu erklären.

Systematische Differenzdilatometriemessungen mit einer hohen Probenanzahl wurden an Nickel nach Verformung mit HPT und ECAP durchgeführt. Der Vergleich der beiden Methoden, liefert eine generelle Ähnlichkeit: in beiden Fällen ist das Ausheilen in drei Stufen unterteilt, dabei handelt es sich bei der ersten um Erholung und der zweiten um Rekristallisation. Die erste Stufe zeigt eine anisotrope Längenzunahme in bestimmten Orientierungen und eine Längenabnahme in allen anderen. Generell führt ECAP zu einem niedrigeren Verformungsgrad und niedrigeren Defektdichten, was niedrigere Längenänderungen und eine Verschiebung der Stufen zu höheren Temperaturen zur Folge hat. Durch HPT und durch ECAP kommt es zu einer typischen Verlängerung der Körner in Scherrichtung. Diese ist nach HPT stärker als nach ECAP, welche auch zu größeren Körnern führt als HPT.

Der Einfluss der Probenorientierung relativ zur Scherrichtung, der Verformungsmethode, der Position innerhalb der HPT-Scheibe oder des ECAP-Stabes, und des Verformungsgrades wurden systematisch untersucht. Restspannungen konnten dank Messungen mit HPT-verformtem Nickel, welches

elastisch oder plastisch nachverformt wurde, als mögliche Ursache für das anisotrope Ausheilverhalten ausgeschlossen werden. Differenzdilatometriemessungen an Proben mit spezieller Geometrie, welche durch Spannungen ausgelöste Verstauchungen der Probe identifizieren kann, bestätigten dies.

Neutronenstreuungsmessungen am FRM-II in Garching unterstützen diese Ergebnisse. Zwar konnten innerhalb einer HPT-Scheibe Restspannungen gemessen werden, aber Proben, welche mit identischen Dimensionen wie Proben für Differenzdilatometriemessungen aus einer HPT-Scheibe geschnitten wurden, zeigten keine makroskopischen Restspannungen. Stattdessen wurde ein Modell entwickelt, demnach Leerstellen aufgrund der anisotropen, verlängerten Kornform anisotrop an Korngrenzen ausheilen. Dieses anisotrope Ausheilen kann zusammen mit einer nach außen gerichteten Gitterausdehnung die Längenzunahme in Proben, in denen die Körner in Messrichtung verlängert sind, erklären. Mit diesem Modell ist es möglich, das Volumen relaxierter Leerstellen aus Dilatometrieergebnissen und Mikrostrukturdaten direkt zu ermitteln.

Die Ergebnisse der Dilatometriemessungen gingen in ein numerisches Modell des Ausheilverhaltens von ultrafeinkörnigem Nickel durch Ausheilen von Leerstellen an Korngrenzen, Rekristallisation und Schrumpfen von Voids ein. Die Existenz letzterer wird nahegelegt durch SQUID-Messungen des Magnetisierungsverhaltens von ultrafeinkörnigem Nickel. Zusammengefasst zeigt diese Arbeit, dass Differenzdilatometrie von hochreinem, ultrafeinkörnigem Nickel die exakte Bestimmung von Überschussvolumen und davon abgeleiteten Materialeigenschaften ermöglicht. Erste orientierungsabhängige Differenzdilatometriemessungen von ultrafeinkörnigem Titan von kommerzieller Reinheit zeigen ebenfalls vielversprechende Ergebnisse.

Abstract

The method of High-Pressure Torsion (HPT) results in large plastic deformation by applying shear through torsion of a metal disc under pressure. The result of this deformation is an ultrafine-grained microstructure with high defect concentrations and thus high excess volume associated with those lattice defects. The excess volume of defects is a key parameter in understanding materials properties. Based on previous works focused on difference dilatometry measurements of high-purity nickel deformed by HPT, this present work expands these measurements on nickel deformed by Equal-Channel Angular Pressing (ECAP), and aims at the understanding of the correlation between the anisotropy of the annealing behavior and the anisotropic microstructure resulting from HPT and ECAP.

Systematic studies of difference dilatometry using a large set of samples have been performed on HPT- and ECAP-deformed nickel. Comparing the two deformation methods, a general similarity was observed: both resulted in a three-stage annealing behavior with the first one due to recovery and the second due to recrystallization. Of these the first stage shows an anisotropic length increase in samples of certain orientations and a length decrease in all other orientations. In general, ECAP-deformation resulted in a smaller strain and lower defect concentrations which manifests in smaller length changes and a shift of the stages to higher temperatures. The microstructure after both HPT and ECAP is governed by an elongation of the crystallites along shear direction. This elongation is more pronounced after HPT than after ECAP which also results in larger crystallite sizes compared to HPT.

The influence of the sample orientation in relation to shear direction, method of deformation, position of the sample within the HPT disc or ECAP rod, and the applied strain were systematically studied. A possible influence of

residual stress on the anisotropy of the annealing behavior could be ruled out based on comparisons with HPT-deformed nickel which was subjected to elastic or plastic post-deformation. This was further confirmed by difference dilatometry measurements on samples with specifically prepared geometries to detect stress-induced sample distortions.

These results are supported by neutron diffraction measurements performed at the FRM-II in Garching. While residual stresses was observed in a bulk HPT disc, dilatometry-shaped samples cut from such a disc do not exhibit any macroscopic residual stress. Instead, a model of anisotropic vacancy annealing at grain boundaries due to the anisotropic crystallite shape was developed. In combination with an outward expansion of the lattice this anisotropic vacancy annealing can indeed explain the length increase observed in samples where the crystallites are elongated along the measurement direction. This model allows the direct determination of the volume of a relaxed vacancy by combining difference dilatometry with microstructure data.

The results from the dilatometry measurements were entered into a numerical model of the annealing of ultrafine-grained nickel by means of vacancy annealing at grain boundaries, recrystallization and void shrinkage. The existence of voids is supported by results from SQUID measurements of the magnetization behavior of ultrafine-grained nickel. In conclusion, difference dilatometry applied to ultrafine-grained, high-purity nickel proved a powerful tool for precisely determining the excess volume of this material and key material parameters derived thereof. Preliminary orientation-dependent difference dilatometry measurements on commercial-purity, ultrafine-grained titanium also showed promising results as well.

AFFIDAVIT

I declare that I have authored this thesis independently, that I have not used other than the declared sources/resources, and that I have explicitly indicated all material which has been quoted either literally or by content from the sources used. The text document uploaded to TUGRAZonline is identical to the present doctoral thesis.

Date	Signature

Contents

1

Introduction

Since about 25 years bulk ultrafine-grained materials have garnered interest due to their highly attractive properties [1] such as high strength in combination with good ductility [2], or good corrosion resistance [3]. To gain these benefits, though, one has to resort to methods of Severe Plastic Deformation or SPD. The most common methods of SPD are High-Pressure Torsion or HPT [4] and Equal-Channel Angular Pressing or ECAP [5].

During SPD large amounts of defects – most notably grain boundaries, dislocations and vacancies – are generated which are the source of the outstanding properties of ultrafine-grained materials [6]. However, due to this large defect concentrations the ultrafine-grained microstructure produced by SPD is a metastable state. Accordingly, recovery of defects and recrystallization of the microstructure take place at reduced temperatures [7]. This reduced thermal stability of ultrafine-grained materials poses a major limitation to their potential application [8].

In order to overcome this limitation basic research in the area of the annealing of defects becomes highly important. Especially, when one considers that defects not only govern the final properties of ultrafine-grained materi-

als [9], but are also the key to the deformation process itself [10]. It quickly becomes apparent how detailed knowledge about the behavior of defects benefits the optimization of SPD processes [11]. And it is therefore that this and previous work has been devoted to the study of defects by the method of high-precision difference dilatometry [12].

The method of difference dilatometry is capable of measuring the excess volume – that is the additional volume compared to a perfect lattice – that is associated with almost any defect [13]. The application of dilatometry to volume changes in the pico- and nanometer regime is made possible by a combination of high-precision equipment and the high defect concentrations in ultrafine-grained materials [14]. Due to these advantages difference dilatometry has already been used to measure the absolute concentrations of defects after SPD deformation [15] or to measure the excess volume of grain boundaries [16].

In this previous work it was found that the annealing behavior of ultrafine-grained materials prepared by SPD is more complex than expected [17]. Further investigations into the interplay between annealing defects and the structure created during different kinds of plastic deformation became necessary. Especially the behavior of vacancies and dislocations regarding the orientation and shape of the crystallites required further attention. The latter being heavily dependent on the conditions of plastic deformation a material undergoes [18, 19, 20].

The core of these investigations was again represented by the combination of difference dilatometry and electron microscopy which has already proven its merit in the previous work [21, 17, 22]. The complementary technique of neutron diffraction – performed with STRESS-SPEC at the FRM-II of the TU München – allows for the precise measurement of lattice parameters. This combination of measuring volume change and lattice parameter has

already been applied prominently [23], and was now applied for ultrafine-grained materials.

This work was realized in cooperation with:

- Erich Schmid Institute of Materials Science, Austrian Academy of Sciences, Leoben, Austria
- Institute of Materials Physics, University of Münster, Münster, Germany
- Department for Advanced Implant Solutions, AIT Austrian Institute of Technology, Wiener Neustadt, Austria
- Department of Advanced Structural Materials, Institute of Physics of ASCR, Prague, Czech Republic
- Austrian Centre for Electron Microscopy, Graz University of Technology, Graz, Austria
- FRM-II, Technical University Munich, Garching, Germany

Parts of this dissertation are already published in the following journals:

- J. Kotzurek, E.-M. Steyskal, B. Oberdorfer, A. Hohenwarter, R. Pippan, W. Sprengel and R. Würschum: *Direct measurement of vacancy relaxation by dilatometry*, Appl. Phys. Lett. **109** (2016) 021906
- J. Kotzurek, W. Sprengel, M. Krystian, S. Simič, P. Pölt, A. Hohenwarter, R. Pippan and R. Würschum: *Structural anisotropy in equal-channel angular extruded nickel revealed by dilatometric study of excess volume*, Int. J. Mater. Res. **108** (2017) 81-88

2

Previous Work and State of Research

In the PhD thesis of B. Oberdorfer [17] and the publications [15, 24, 25, 26] resulting thereof high-precision difference dilatometry has been applied to ultrafine-grained materials in combination with positron annihilation. The ultrafine-grained materials were high-purity iron, nickel and copper, as well as Armco-iron. Severe Plastic Deformation was performed by HPT in cooperation with the group of R. Pippan at the Erich Schmid Institute in Leoben, and the group of M. Zehetbauer at the University of Vienna.

In the case of iron it was found that the lower purity in Armco-iron resulted in a finer crystallite size than in high-purity iron. The ultrafine-grained microstructure is stable up to roughly 400 K with the high-purity iron slightly less stable than Armco-iron. Starting at 400 K a recovery and recrystallization step up to temperatures of about 800 K takes place after which a coarse-grained microstructure remains [15]. Overall length changes between -8.6×10^{-4} and -10.8×10^{-4} were observed for high-purity iron.

Positron lifetime measurements, as well as *in-situ* measurements of the *S*-parameter at the NEPOMUC instrument at the FRM-II reactor in Garching support these observations. The positron annihilation measurements were performed on Armco-iron and showed characteristics of positron trapping and annihilation in dislocations. This was the first time that such measurements were performed on SPD-deformed ultrafine-grained materials.

For ultrafine-grained copper first a recovery stage (henceforth denoted as stage A) and then a well-separated recrystallization stage (henceforth denoted as stage B) are observed [26]. Stage A lasts up to a temperature of about 410 K, but shows no clear onset. Stage B which immediately follows stage A is markedly sharp and only lasts up to about 450 K. These two stages are followed by another, very broad stage (henceforth denoted as stage C) which extends beyond the maximum temperature measured (673 K).

Positron lifetime measurements of copper indicate annealing at vacancies and dislocations. After heating to 458 K the bulk lifetime is similar to literature values pointing towards a defect-free microstructure after stage B. *In-situ* measurements at the NEPOMUC instrument show no change of the *S*-parameter up to about 400 K which is again explained by saturation trapping [24]. After that temperature the *S*-parameter starts to drop with the largest change between 430 K and 450 K. The delay in the onset is explained by the still small crystallite size at the beginning of recrystallization.

Further measurement methods were applied to ultrafine-grained copper to compare the results with results from difference dilatometry measurements. Differential Scanning Calorimetry show an exothermic peak during the recrystallization that happens in stage B. From the area under the peak the grain boundary energy was derived and found to nicely match the literature values. Electrical resistance measurements show a drop of the resistance beginning at about 380 K and ending at the end of stage B.

A significant amount of research has been dedicated to high-purity, ultrafine-grained nickel prepared by HPT. Similar to copper the annealing behavior of nickel also shows a distinct stage A between about 350 K and 450 K. Electron microscopy images show no significant change of the crystallite size during this stage. However, during the subsequent stage B which ranges from about 450 K and 490 K the crystallite size increases clearly. The final stage C going up to 773 K then shows a further growth of the coarse-grained microstructure.

Positron annihilation measurements show a very similar result for ultrafine-grained nickel compared to copper [24]. The lifetime measurements result in a positron lifetime between the values for annihilation at vacancies and at dislocations. The *in-situ* measurements result in a stable S-parameter up to stage B with a sharp drop during that stage. However, during stage A a slight decrease of the S-parameter can be observed too. This points toward the annealing of vacancies and dislocations happening during stage A.

Difference dilatometry also allows the measurement of kinetic parameters such as activation energies [25]. Kissinger analyses were performed with the dilatometry results from all ultrafine-grained materials: for the fcc metals nickel and copper the activation energies of the recrystallization were determined. These two metals showed well-separated recovery and recrystallization peaks. On the other hand, for the bcc metal iron (both Armco-iron and high-purity iron) recovery and recrystallization stages were considered to coincide and a combined activation energy was determined.

It was found that the activation energies derived from the difference dilatometry measurements excellently agree with literature values. Furthermore, in the case of ultrafine-grained copper the results from the calorimetry and resistance measurements matched with the difference dilatometry results too. For ultrafine-grained nickel a Johnson-Mehl-Avrami-Kolmogorov kinet-

ics model modified for linear heating was applied to stage B as well. The numerical analysis yielded an activation energy identical to the activation energy from the Kissinger analysis.

Ultrafine-grained copper and nickel show very distinct annealing stages with recrystallization taking place in the second stage. It can be assumed that the length change of this stage is caused only by the reduction of the number of grain boundaries and their aggregated excess volume. Therefore, it becomes possible to derive the grain boundary excess volume from the length change and the crystallite sizes before and after stage B [16].

Measured values for the grain boundary excess volume are very scarce, but the values found by difference dilatometry nicely match results from computer simulations. For ultrafine-grained iron recrystallization takes place parallel to recovery thus a direct measurement of the grain boundary excess volume – taking into account only the second half of the single stage – must be considered less accurate.

During the difference dilatometry measurements of high-purity, ultrafine-grained iron and nickel an unexpected behavior was observed. Depending in which direction the length change was measured either a length decrease or a length increase was observed. In high-purity iron samples this length increase occurs over the first half of the single annealing stage. At a temperature of about 510 K the length increase stops and the expected length decrease happens. In nickel samples the length increase occurs during stage A of the annealing.

Macroscopic residual stresses were considered as potential explanation for this behavior, but X-Ray Diffraction measurements did not reveal any hints of such stresses. Instead it was suggested that the length increase is caused by a directional diffusion of vacancies due to a strong shape anisotropy of

the crystallites. A similar anisotropic annealing behavior which was observed in ultrafine-grained copper processed by equal-channel angular pressing by Klement [27] was interpreted as thermally activated Bauschinger effect in which parts of the plastic deformation is reverted [28].

In view of the unclarified issue regarding the anisotropic annealing behavior, the present thesis aims at extensive difference dilatometry measurements with respect to sample orientation and processing method were decided on. The first goal of these extensive measurements was to generate results from a larger sample size than in all previous measurements. The second goal was to expand the difference dilatometry measurements to ultrafine-grained nickel prepared equal-channel angular pressing. The third and final goal was to shed more light into the tentative explanations brought up by Oberdorfer, Steyskal and Klement.

The results from the difference dilatometry measurements performed to achieve said goals are presented in this work. Additionally, neutron diffraction measurements and SQUID measurements which were performed to complement the difference dilatometry results are expounded. Furthermore, the difference dilatometry method is extended on the hcp metal titanium after preparation by equal-channel angular pressing. The results from these measurements prove the merit of difference dilatometry in discerning key material parameters after plastic deformation.

3

Experimental Methods

3.1 High-Pressure Torsion

The route of High-Pressure Torsion or HPT is a commonly applied SPD method since it is possible to apply large strains without an overall change of the specimen geometry. That means that extreme strains can be achieved [29] without material loss. Besides that, the method of HPT has continuously been scaled up to specimen of up to 50 mm diameter.

The concept of HPT is to apply a shear deformation on a disc-shaped specimen by placing the specimen between two anvils, applying a pressure of a few GPa, and rotating one of the anvils multiple times (see figure 3.1). For this work HPT deformations were performed at the Erich Schmid Institute in Leoben. The disc specimens prepared in this laboratory had diameters of 30 mm at heights of 7 mm.

Before HPT deformation the disc specimens were pressed in shape between the anvils. Afterwards the specimens were annealed under ultrahigh vacuum chamber placed on a resistance-heated tungsten boat at about 920 K (mea-

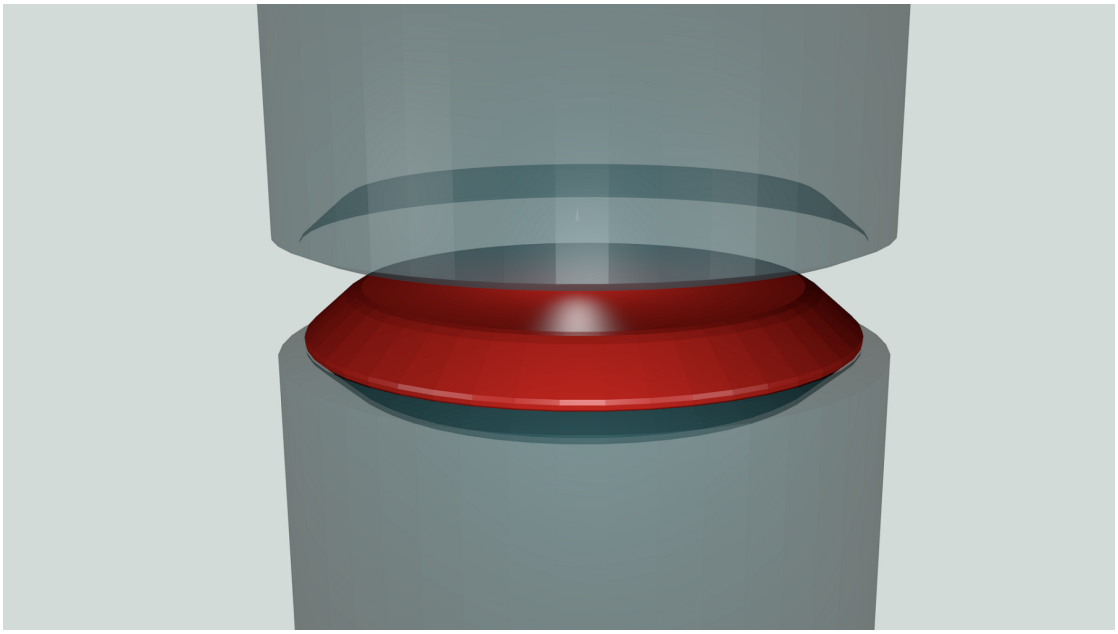

Figure 3.1: Model of a High-Pressure Torsion (HPT) facility. The disc (red) has a diameter of 30 mm and a height of 7 mm. The two steel anvils (blue) are pressed against each other and the lower one is rotated.

sured by a pyrometer) which equals to about $0.6\,T_m$. The annealing becomes necessary since a large number of dislocations are created when the disc specimens are pressed into shape. But for reproducible results it is important to start the deformation process from a well-annealed microstructure. After annealing the specimens, they were sandblasted to guarantee enough friction between the disc and the anvils.

The equivalent strain ε applied on the disc during deformation by HPT can be calculated by [30]:

$$\varepsilon = \frac{n}{\sqrt{3}} \frac{2\pi r}{h} \tag{3.1}$$

where n denotes the number of turns applied, r the radius on the disc spec-

imen, and h the height of the disc specimen. Since the height of the disc specimens slightly decreases from the center of the disc to its edge, and since the disc specimens are slightly compacted during the deformation, the calculated ε-values have to be considered as approximations.

At the beginning of the deformation process dislocations are generated allowing plastic deformation. With increasing numbers of dislocations they assemble into cell walls within larger crystallites [31, 32]. Eventually, the misalignment between cells becomes larger and new grain boundaries evolve forming new, refined crystallites. However, the refinement quickly reaches a threshold at which the crystallites size becomes stable.

In this steady-state an equilibrium between the crystallite refinement and the growth of preferential crystallites is reached [33]. The microstructure at this point of the deformation is in a state of saturation and further straining does not lead to further crystallite refinement. All disc specimens prepared by HPT that were used in this work were deformed to steady-state.

3.2 Equal-Channel Angular Pressing

Besides HPT the second common method for SPD is Equal-Channel Angular Pressing or ECAP. This method is sometimes also called Equal-Channel Angular Extrusion or ECAE. By deformation with ECAP large strains can be achieved too, but usually not to the same degree as with HPT. The difficulty with ECAP is that during the deformation a change of the specimen geometry occurs which cannot be neglected. Nonetheless, it is a popular method due its relatively simple machinery and the multiple parameters affecting the deformation.

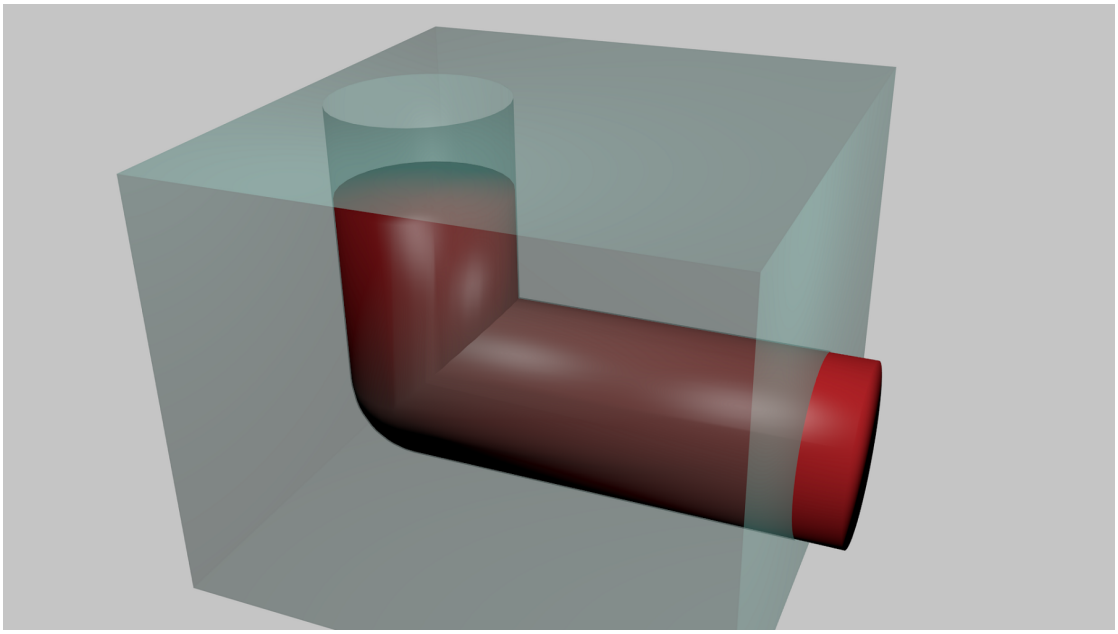

Figure 3.2: Model of a Equal-Channel Angular Pressing (ECAP) facility. The rod (red) has a diameter of 20 mm and a length of 100 mm. The plunger which pushes the rod through the channel inside the die (blue) is not pictured.

The concept of this method is to press a rod-shaped specimen through an angled channel of similar diameter in a die (see figure 3.2). This procedure is usually repeated for multiple passes accumulating the applied strain. Between each of these passes the rod specimen may or may not be rotated around its cylinder axis – resulting in various "routes" of deformation by ECAP.

The most common routes are the route A in which the rod specimen is not rotated at all, the route B in which the specimen is rotated by 90°, and the route C in which the specimen is rotated by 180° (see figure 3.3). Route B can be divided further into the route B_A and the route B_C. For route B_A the rotation direction alternates between clockwise and counterclockwise. For route B_C the rotation direction is kept the same after each pass. Route B_C is the most popular route for deformation by ECAP.

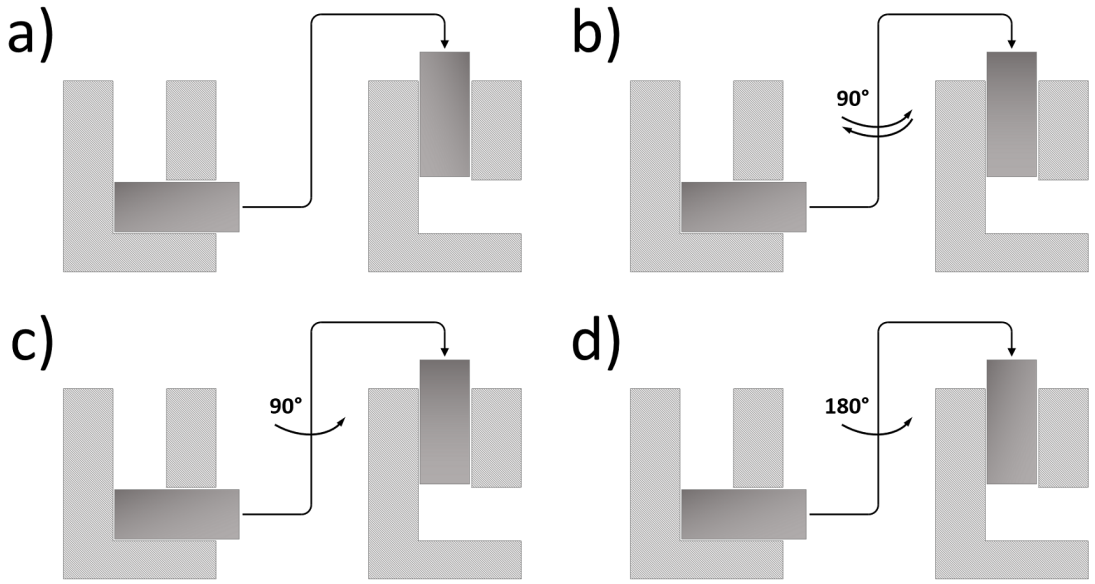

Figure 3.3: Comparison of the most common ECAP routes. (a) Route A: the rod specimen is not rotated between the passes. (b) Route B_A: the rod specimen is alternately rotated by +90° and -90° after each pass. (c) Route B_C: the rod specimen is rotated by 90° after each pass. (d) Route C: the rod specimen is rotated by 180° after each pass.

The channel through which the rod specimen is pressed usually has a circular shape, but quadratic shapes are possible as well. The angle in the channel is denoted "inner angle" and often an angle of 90° is chosen, but other angles are not uncommon either. Furthermore, the channel may show a curvature at the outside of the angle which is described by an "outer angle". An outer angle of 0° means no curvature at all (see figure 3.4). Further parameters affecting the deformation are the pressure applied, as well as whether or not back-pressure is applied.

Deformations by ECAP for this work were performed at the Department for Advanced Implant Solutions in Wiener Neustadt, a subdivision of the AIT Austrian Institute of Technology. The rod specimens had diameters of 20 mm and lengths of 100 mm. The channel had an inner angle of 120° and an outer angle of 27.8°.

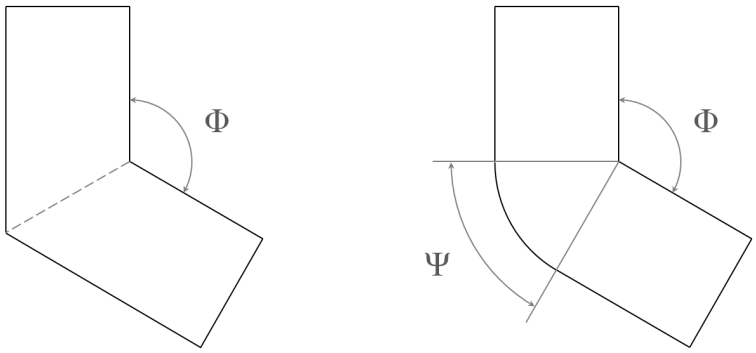

Figure 3.4: Geometry of the ECAP channel. The "inner angle" Φ denotes the angle between the inlet and outlet channels. The "outer angle" Ψ defines the curvature of the channel at the outside.

The equivalent strain ε applied on the rod specimen during deformation by ECAP can be calculated by [34]:

$$\varepsilon = \frac{n}{\sqrt{3}} \left[2 \cot\left(\frac{\Phi}{2} + \frac{\Psi}{2}\right) + \Psi \operatorname{cosec}\left(\frac{\Phi}{2} + \frac{\Psi}{2}\right) \right] \tag{3.2}$$

where n denotes the number of passes, Φ the inner angle, and Ψ (in rad) the outer angle. Unlike deformation by HPT (as seen in equation 3.1), the equivalent strain ε applied during deformation by ECAP is uniform through the whole specimen. However, the applied strains are generally lower after deformation by ECAP. Since at the ends of the rod specimens the geometry changes significantly after each pass, they have to be cut off after processing. Therefore, the length of the specimens is reduced for each pass and thus their number is limited.

In contrast to HPT the shear deformation in ECAP happens during discontinuous passes and, with the exception of route C, the shear plane changes after each pass [35]. As a result the saturation microstructure depends on

the route of deformation. The route B_C is often chosen because it usually results in a very homogeneous microstructure. In general, however, the saturation microstructure after deformation by ECAP is less refined than by HPT [36].

3.3 Difference Dilatometry

3.3.1 Principle of dilatometry

The primary method employed to investigate the annealing behavior of materials prepared by HPT or ECAP in this study was high-precision difference dilatometry. The gist of difference dilatometry is that the samples can be measured simultaneously with a reference sample in a single oven. With this setup the irreversible length changes that are caused by the annealing of free volume-type defects can be measured directly.

Both the sample and the reference sample are of the same material and therefore reversible effects leading to a length change (e.g. thermal expansion or phase changes) are identical. The sample additionally shows irreversible effects leading to a one-time length change. Sample and reference sample are heated simultaneously and the difference of the relative length changes between them is calculated:

$$\frac{\Delta L}{L_0} = \left.\frac{\Delta L}{L_0}\right|_{\text{Sample}} - \left.\frac{\Delta L}{L_0}\right|_{\text{Reference}} \tag{3.3}$$

The total difference of the relative length changes $\frac{\Delta L}{L_0}$ is the sum of the irreversible length changes associated with the annealing of different defect

types. If perfectly isotropic annealing of the defects is assumed (which is the case e.g. in ultrafine-grained copper), then the contribution of vacancies can be written as:

$$\left.\frac{\Delta L}{L_0}\right|_{\text{Vacancies}} = -\frac{1}{3} C_V \, (1 - r) \tag{3.4}$$

with C_V being the vacancy concentration, and r being the relaxation factor of the lattice relaxation at a vacancy. The length change described in equation 3.4 constitutes of an isotropic length decrease due to relaxed vacancies being replaced by atoms of the atomic volume Ω. The atoms enter the crystallite equally from each of the three space directions.

After SPD-deformation high dislocation densities are usually observed [14]. The dislocations can exist as geometrically necessary dislocations (GNDs) or as mobile dislocations (MDs) [37]. The annealing or (to a certain degree) the polygonization of mobile dislocations also leads to an irreversible length change. This length change can be written as:

$$\left.\frac{\Delta L}{L_0}\right|_{\text{Dislocations}} = \frac{1}{3} \, \gamma_{MD} \, \rho_{MD} \tag{3.5}$$

with γ_{MD} being the size of the core of a mobile dislocation, and ρ_{MD} being the density of mobile dislocations.

The irreversible length changes of vacancies (equation 3.4) and dislocations (equation 3.5) occur during stage A. The length change during stage B is caused by recrystallization i.e. the reduction of the number of grain bound-

aries. This length change can be written as [16]:

$$\left.\frac{\Delta L}{L_0}\right|_{\text{Grain Boundaries}} = \epsilon_{GB}\left[\left(\frac{1}{d_{ini}}\right) - \left(\frac{1}{d_{fin}}\right)\right] \tag{3.6}$$

with ϵ_{GB} being the grain boundary excess volume, d_{ini} being the crystallite size before recrystallization, and d_{fin} being the crystallite size after recrystallization. In order for equation 3.6 to be valid it has to be assumed that the majority of vacancies and mobile dislocations have been annealed during stage A.

3.3.2 Experimental setup

The high-precision difference dilatometer used for the bulk of the measurements presented in this work is a model LV75 VD LT from the manufacturer Linseis. The setup of the dilatometer is displayed in figure 3.5. Sample and reference are placed below two quartz push rods which transfer the vertical displacement to a pair of inductive position sensors. The sample temperatures are measured by a type K thermocouple placed between the push rods.

Due to an inevitable temperature lag the actual sample temperatures are lower than the temperatures measured. This lag can be observed during heating rate-dependent measurements of a heating rate-independent phase transition e.g. the Curie transition of nickel [38]. From these measurements a heating rate-dependent temperature correction can be derived. The correction values are listed in table 3.1; values for other heating rates can be interpolated from these values.

(a) Linseis LV75 VD LT dilatometer.

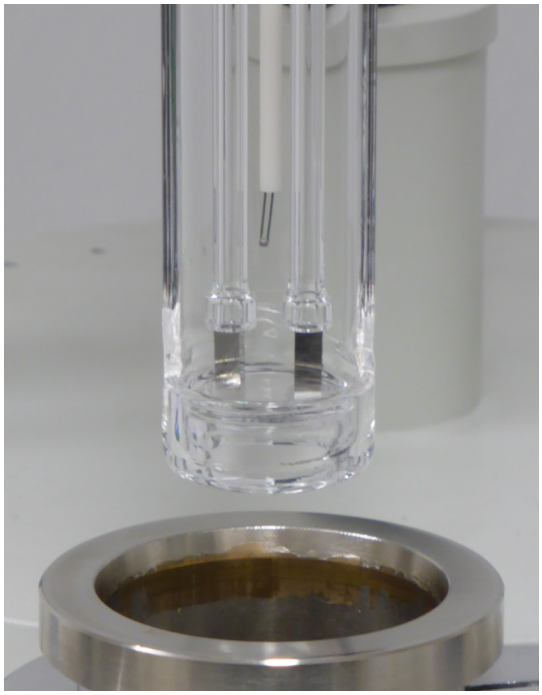

(b) Close-up of the measuring unit.

Figure 3.5: The setup for the difference dilatometry measurements. (a) The dilatometry unit with oven, argon gas supply, gas flow controller and liquid nitrogen dewar. (b) Two samples mounted beneath the push rods with thermocouple between them.

For the measurements the sample holder is lowered into a resistance-heated oven chamber. The chamber and the samples are usually flushed with pure argon gas (purity 5.0) before and during measurements. Slow cooling is achieved by use of a fan and rapid cooling by flushing the oven chamber with liquid nitrogen.

3.3.3 Preparation of dilatometry samples

The samples used for difference dilatometry measurements are prism-shaped with dimensions of roughly $3\times3\times7\,\mathrm{mm}^3$ (as seen in figure 3.5). The quadratic

Table 3.1: Temperature lag between thermocouple and nickel samples (of dimensions $3\times3\times7\,\mathrm{mm}^3$) depending on the heating rate. Other heating rates were interpolated.

φ /K min^{-1}	Δ /K
1.5	1.4
3.0	2.9
6.0	5.7

base planes have to be plane and parallel in order for stable measurements. The samples can be cut from the HPT and ECAP specimens in three principal directions or orientations in respect to their measurement direction (along the long side).

For disc-shaped specimens prepared by HPT the three principal directions are the axial, radial and tangential (A, R and T) direction as seen in figure 3.6. For rod specimen prepared by ECAP the three principal directions are the transverse, normal and extrusion (V, N and E) direction as seen in figure 3.7. For the electron micrographs the two directions spanning the plane are quoted e.g. figure 3.8 shows the A-R plane (viewed from T direction).

During deformation by HPT and ECAP the specimen undergo a shear deformation [39]. Dilatometry samples with axial and radial orientations are positioned within the specimens perpendicular to the shearing direction. Dilatometry samples with tangential orientation are positioned parallel to the shearing direction. For deformation by ECAP the relation between sample orientation and shearing direction is more complex.

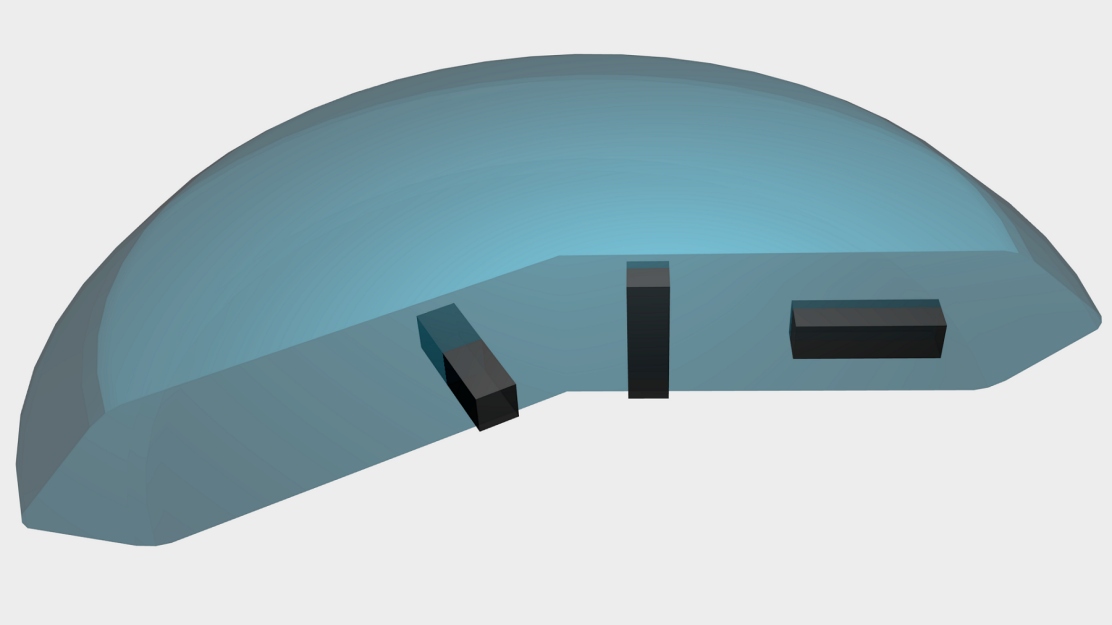

Figure 3.6: The three possible orientations for dilatometry samples cut from a disc specimen processed by HPT: axial (left), tangential (center) and radial (right) orientation.

3.4 Electron Microscopy

Analyses of the ultrafine-grained microstructure were performed based on Scanning Electron Microscopy (SEM) images created in cooperation with the Austrian Centre for Electron Microscopy and Nanoanalysis (FELMI-ZFE) at Graz University of Technology. The instrument in question is a Zeiss Ultra 55 with a resolution of 1.0 nm at 15 kV according to specifications. In order to gain microstructure information the images were acquired by using an Backsactter Electron Detector (BSE).

The images acquired by SEM were processed and analyzed by the program "ImageJ" [40]. The standard procedure involved an automated edge detection as well as manual correction (e.g. incomplete edges, doubles) of the

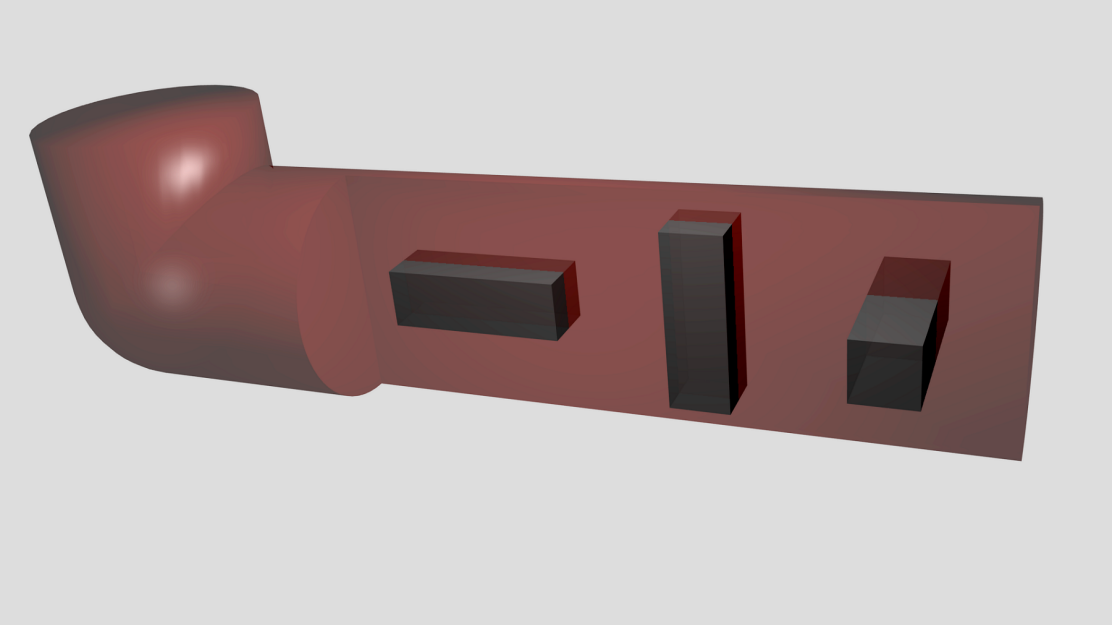

Figure 3.7: The three possible orientations for dilatometry samples cut from a disc specimen processed by ECAP: extrusion (left), normal (center) and transverse (right) orientation.

results obtained numerically. The result of this procedure is an 8-Bit black-and-white line art image (see figure 3.8) from which the crystallite size can be determined by the line intercept method [17].

Additionally, on two samples Electron Backscatter Diffraction (EBSD) measurements were performed on the same instrument. This method not only provides information about the crystallite size and shape, but also about the crystallite orientation [41]. Thus, preferential crystallite orientations or textures which are usually a byproduct of plastic deformation can be determined.

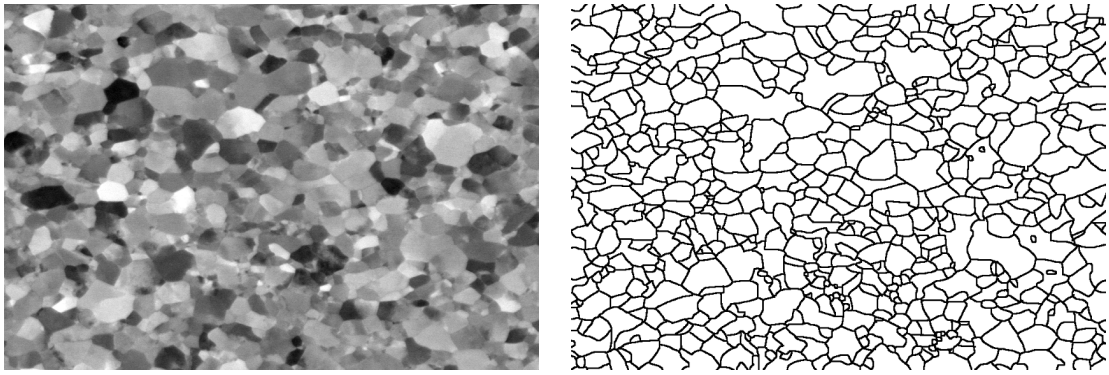

(a) Raw SEM image. (b) Image after processing.

Figure 3.8: Input and result of the ImageJ image analysis procedure. (a) The unprocessed image (showing the A-R plane) from the SEM measurement. (b) The same image after the grain boundaries have been identified.

3.5 Neutron Diffraction

Diffraction techniques are a standard method in materials science with the most common being X-Ray Diffraction (XRD). Due to the wave character of subatomic particles electrons or neutrons can be used for diffraction experiments as well.

The method of neutron diffraction has some advantages that make it a unique tool in materials science. First, neutrons do not have an electric charge and therefore interact with the atomic core and not the electron shell of the atom. As a result, neutrons penetrate materials very well and delivers information about the bulk of the material (in contrast XRD only gives information of layers near the surface). Furthermore, neutrons possess a magnetic moment and can be used to probe magnetic properties of materials.

A major advantage of neutron diffraction is the fact that the wavelength of thermal neutrons is of the same scale as interatomic distances in solids.

Therefore, neutron diffraction is well suited to investigate properties of atomic lattices. For example the lattice constants of a crystalline solid can be measured very exactly. Consequently, deviations from the equilibrium lattice constants in the form of residual stresses can be measured exactly as well.

The basic principle of residual stress measurement by neutron diffraction is given by the Bragg equation [42]:

$$2d_{hkl} \sin\theta = n\lambda \tag{3.7}$$

where d_{hkl} denotes the spacing between two crystallographic planes of the orientation $\{hkl\}$, 2θ the diffraction angle, n an integer and λ the wavelength of the neutrons.

Assuming monochromatic neutrons the diffraction angle 2θ only depends on the lattice spacing d_{hkl}. The lattice strain ε in the direction of the scattering (i.e. at half angle between incident and scattered neutron beam) is then given by [43]:

$$\varepsilon = \frac{\Delta d_{hkl}}{d_{hkl}} = -\Delta\theta \cot\theta \tag{3.8}$$

where Δd_{hkl} denotes the change to the stress-free lattice spacing d_{hkl}, and $\Delta\theta$ the shift of the diffraction angle.

A measurable change of the lattice spacing requires either residual stress of the 1st (stress field of the same size scale as the sample) or of the 2nd kind (stress field of similar size scale as single crystallites). Only a change of the lattice constants by such stresses results in a $\Delta\theta$ shift of the diffracted

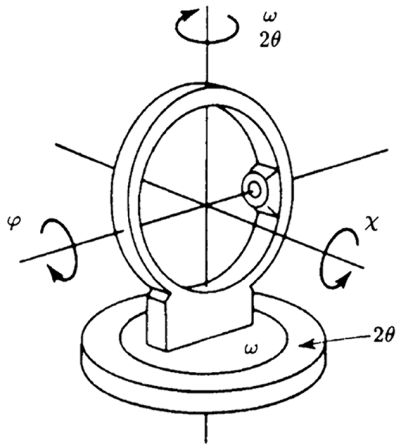

Figure 3.9: The rotation angles ϕ, χ and ω in the coordinate system used for the neutron diffraction measurements (image taken from [46]). In the text ω is denoted ψ for the $\sin^2\psi$ measurements.The diffraction angle 2θ (see equation 3.7) uses the same axis as the angle ω.

peak. Residual stress of the 3rd kind (stress field originating at defects) only results in a broadening of the diffracted peak [44].

A more accurate way to determine residual stresses than by measuring the $\Delta\theta$ shift is the $\sin^2\psi$ method [44, 45]. This method is based on the effect that the lattice spacing d_{hkl} of the plane $\{hkl\}$ is different between crystallites. Depending on the orientation of the crystallites different components of the total stress tensor are affecting the lattice spacing.

This effect is used by measuring the shift $\Delta\theta$ of a selected reflection peak 2θ at various angles ψ or ω (see figure 3.9). A plot of the acquired 2θ shift as a function of $\sin^2\psi$ results in a linear relationship with a slope proportional to the stress component acting on the lattice. Instead of 2θ the equivalent quantities lattice spacing d_{hkl}, lattice constant a, or strain ε acting on the lattice can be used.

Neutron diffraction is also suitable to determine the texture of a material. The sample is positioned in an Eulerian cradle (see figure 3.9) and

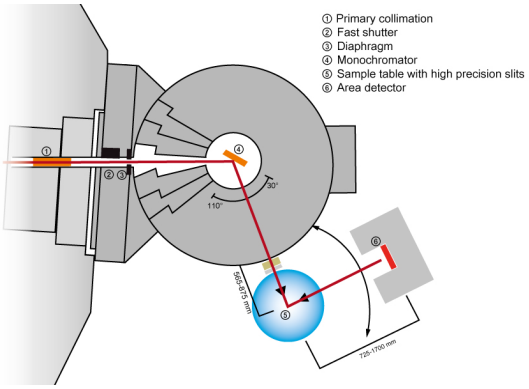

Figure 3.10: Schematic overview of the STRESS-SPEC instrument at the neutron reactor FRM-II (image taken from [48]).

the diffracted intensities of one or more low indexed peaks are measured while scanning over ϕ at defined χ angles. In order to display the recorded intensities as pole figures, the angles ϕ and χ are converted into the pole figure angles $\Delta\alpha$ and $\Delta\beta$ [47].

The residual stress and the texture measurements were both performed at the STRESS-SPEC instrument at the neutron reactor FRM-II of the Technical University Munich in Garching (a schematic can be seen in figure 3.10) [48]. The FRM-II reactor produces fast neutrons by nuclear fission which are then thermalized to an energy of a few meV before being used for measurements.

The STRESS-SPEC instrument which can be used to investigate both residual stresses as well as textures uses thermalized neutrons (beam line SR3). The instrument furthermore utilizes one out of three monochromators: either Ge(511), bent Si(400) or pyrolitic graphite(002) allowing neutron wavelengths of 1 to 2.4 Å. The diffraction angle 2θ can be varied between 35° and 110°. The detector is a $200\times200\,\mathrm{mm}^2$ position-sensitive ^{3}He detector (PSD) with a spatial resolution of $1.5\times1.5\,\mathrm{mm}^2$ (256×256 pixel).

The diffraction pattern obtained from the PSD is analyzed by the program *StressTextureCalculator* [46]. The program corrects the curvature of the diffraction pattern (in the form of three-dimensional Debye-Scherrer cones) on the two-dimensional detector at diffraction angles 2θ which deviate from 90°. The program also corrects differences of the pixel sensitivities and applies a background correction.

4

Experimental Results

In this chapter exemplary results from all measurements will be presented. Moreover, averages derived from the difference dilatometry data will be used. A complete listing of all measurements as well as the results from the difference dilatometry measurements and data determined therefrom can be found in the appendix. For the sake of completeness, results from the diploma thesis of the author [22] will be referenced in this chapter too.

4.1 Difference dilatometry after High-Pressure Torsion

The material for all measurements performed on ultrafine-grained nickel was high-purity (99.99+%) nickel purchased from Goodfellow Cambridge Ltd. The exact chemical composition of the material as provided by the manufacturer is given in table 4.1. The HPT deformations were all performed at the Erich Schmid Institute of Materials Science in Leoben.

Table 4.1: Chemical composition of the high-purity nickel used for the majority of the measurements below. The composition was provided by the supplier Goodfellow Cambridge Ltd.

Element	Concentration /wt. ppm
Ni	Balance
Sb	0.54
C	7.5
Co	1.1
Cu	0.29
Ir	0.32
Fe	1.55
Os	0.36
Re	0.495
Si	0.205
Ta	<1.0
Ti	0.41
Y	0.1

4.1.1 Annealing behavior of samples in tangential orientation

During the diploma theses of Steyskal [21] and the author [22] dilatometry measurements of four respectively six samples in tangential orientation were performed. At the same time 13 respectively 16 measurements on samples in axial orientation were performed. Therefore, a measurement series with statistically significant numbers of samples in tangential samples became desirable.

The required nickel disc of 30 mm diameter and ca. 8 mm height was prepared by five revolutions of HPT under a quasi-hydrostatic pressure of 2.2 GPa. The parameters for this deformation were chosen in order to match

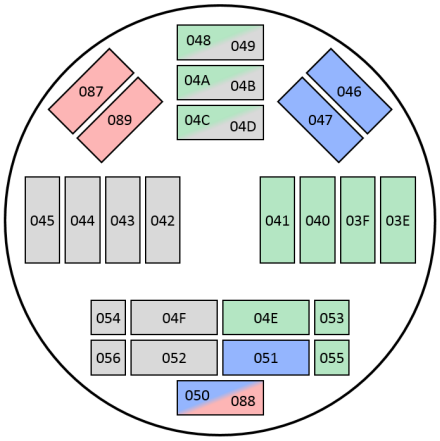

Figure 4.1: Overview of the disc specimen 'Ni5Tan'. The sample designations refer to the list of measurements in the appendix. The color code used in this and following overviews is as follows: blue indicates a heating rate of 1.5 K min^{-1}, yellow of 2.5 K min^{-1}, green of 3.0 K min^{-1}, red of 5.0 K min^{-1}, and gray/black of 6.0 K min^{-1}. Other colors indicate different, irregularly used heating rates.

the deformation parameters from the diploma thesis of Steyskal [21]. From this disc four axial and 20 samples in tangential orientation were prepared. Furthermore, four samples in tangential orientation were prepared which were slightly tilted towards radial direction. The measurement series was labeled 'Ni5Tan': a schematic of the disc and of the samples cut from the disc for the series can be seen in figure 4.1.

Figure 4.2 shows the difference dilatometry curves of samples in tangential orientation from the edge of the specimen Ni5Tan ($\varepsilon = 40$) respectively of samples in axial orientation from that specimen. The samples in tangential and axial orientation show markedly different behaviors: a length increase (T) respectively length decrease (A) in stage A. This characteristic orientation dependence of the annealing behavior has been observed by Steyskal [21], Oberdorfer [17] and the author [22] earlier already. The recovery in stage A is followed by recrystallization in stage B and a broad length de-

Table 4.2: Average length changes during the three annealing stages A, B and C for samples of different orientations (Or.) cut from the disc specimen Ni5Tan. No. indicates the number of samples measured in this orientation.

Or.	No.	$\frac{\Delta L}{L_0}\Big\|_A$ /10^{-4}	$\frac{\Delta L}{L_0}\Big\|_B$ /10^{-4}	$\frac{\Delta L}{L_0}\Big\|_C$ /10^{-4}
A	4	-2.44±0.70	-2.93±0.48	-1.56±0.52
T	20	+0.89±0.33	-1.32±0.43	-1.34±0.54

crease in stage C. The average length changes for this measurement series is listed in table 4.2.

Samples in tangential orientation from closer to the center of the specimen disc also reproducibly reveal the length increase in stage A. However, the amplitudes of the length increases of different samples appear to spread stronger with decreasing distance to the center. So far, this has not been observed for earlier measurements in which mostly samples in axial orientation were used [21].

Apart from the spread of the amplitude in stage A of samples in tangential orientation, the dilatometry measurements yield the expected results. The maximum of the length decrease in stage B is shifted to higher temperatures with increasing heating rate [25] (the effect is easier observed in the temperature derivative curves which are not shown here). A Kissinger analysis [49] of the acquired data (from four samples in axial and 14 samples in tangential orientation) delivers an activation energy of (1.04±0.08) eV. This value is lower than the earlier results [21, 17].

Furthermore, different amplitudes of stage B can be observed (see table 4.2) which are attributed to the difference in the numbers of grain boundaries annealing during this stage [16, 26]. In samples of axial orientation the av-

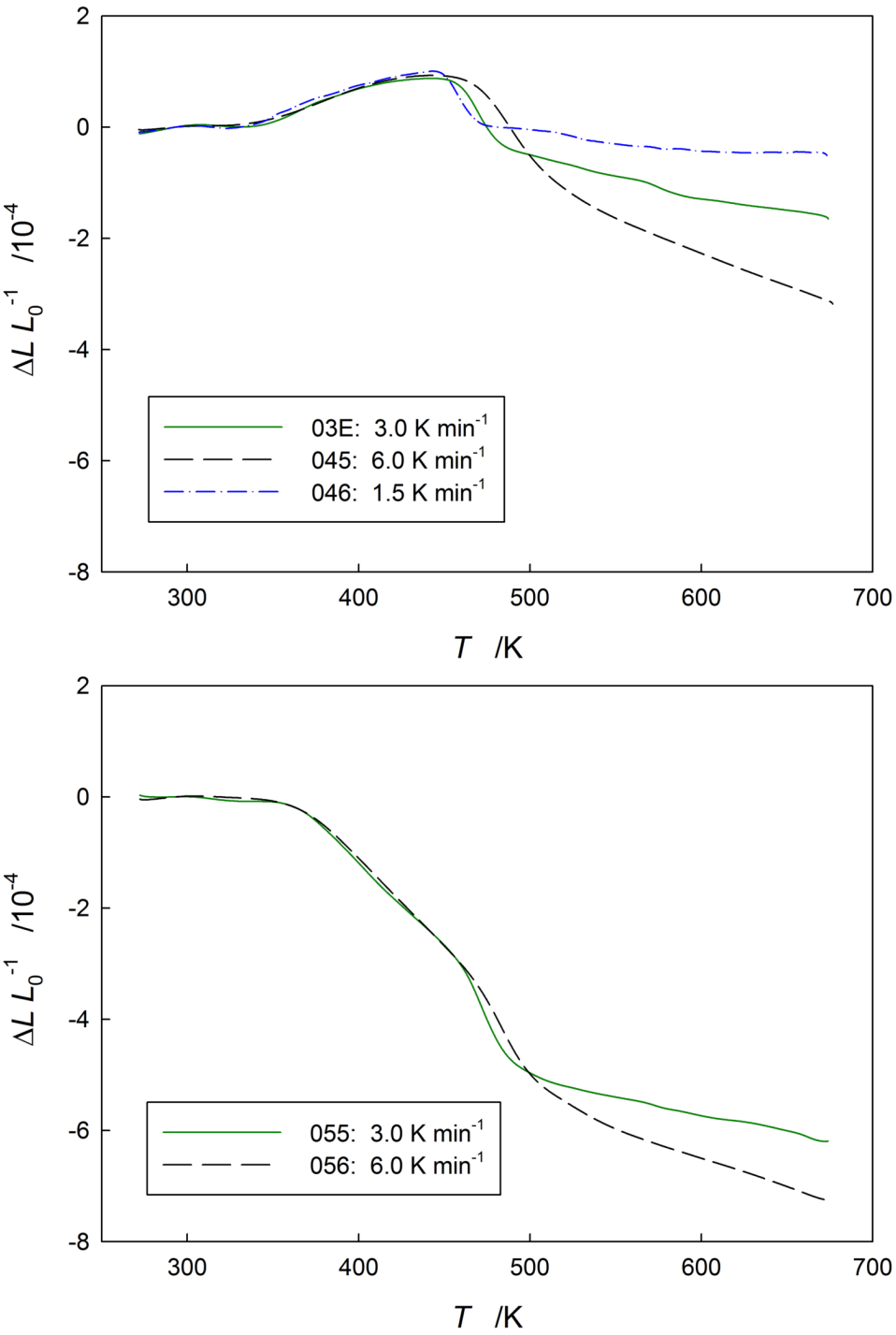

Figure 4.2: Exemplary difference dilatometry curves of samples in tangential (top) and axial (bottom) orientations cut from the specimen Ni5Tan (deformation by HPT, 5 turns). The color code is the same as in 4.1.

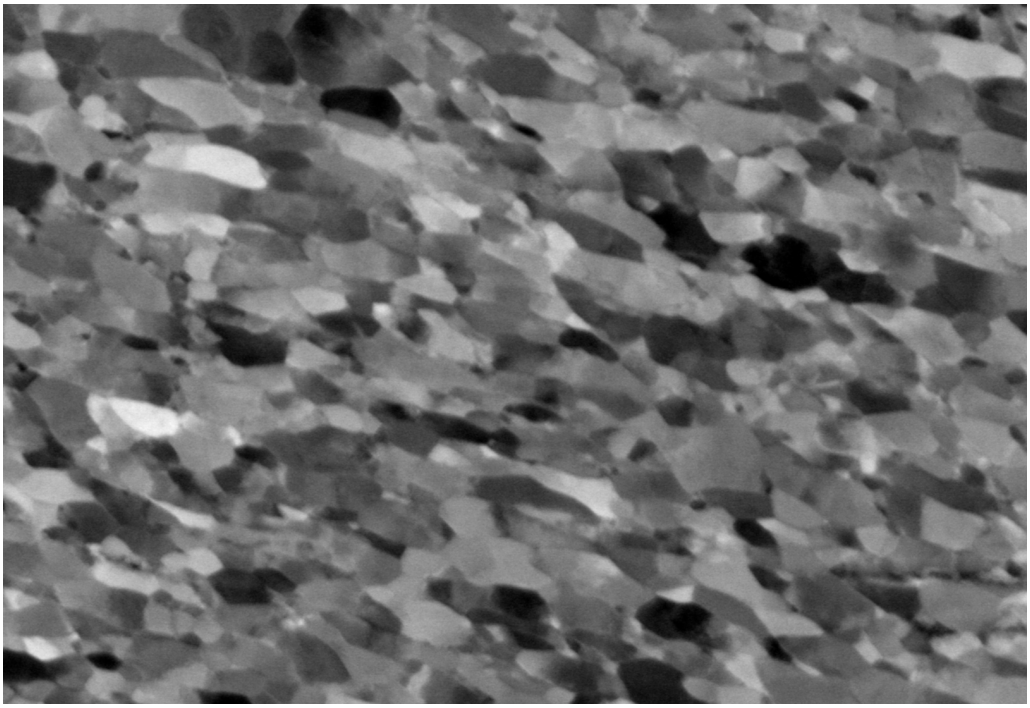

Figure 4.3: Scanning electron microscopy image of high-purity nickel deformed by HPT (specimen Ni5Tan). The image shows the A-T plane of the specimen. The image width is 5.72 µm.

erage length decrease equals ${}^{\Delta L}/_{L_0}|_B = -2.93\times10^{-4}$. Whereas in samples of tangential orientation the length decrease equals to ${}^{\Delta L}/_{L_0}|_B = -1.32\times10^{-4}$. These length changes in combination with crystallite sizes before and after stage B allow to calculate the grain boundary excess volume (see equation 3.6).

Figure 4.3 shows a SEM image of the axial-tangential plane of the specimen Ni5Tan. The elongation of the crystallites is well visible. Images of the radial-axial and the tangential-radial planes show relatively equiaxed crystallites instead. Therefore, the crystallites appear to be elongated along the shear direction with a slight tilt (according to Oberdorfer [17] by 10°) towards the axial direction.

The line intercept method yields crystallite sizes of (217±15) nm along the elongated direction and (120±18) nm perpendicular to the elongated direction. For each direction (parallel and perpendicular to the elongation) five lines were applied each spanning roughly 60 crystallites. This result would equal to an aspect ratio of 1.8 which is well in line with earlier results for nickel processed under similar parameters [17] although the actual crystallite sizes were reported to be larger.

Additionally, EBSD measurements were performed on the axial-tangential plane with an orientation difference of 5° considered a grain boundary. Figure 4.4a shows the acquired orientation distribution image. According to the data from this measurement the average crystallite size equals to (260±150) nm along the elongated direction and (100±30) nm perpendicular to the elongated direction. These values amount to an aspect ratio of 2.7. Figure 4.4b shows the corresponding pole figure.

4.1.2 High-Pressure Torsion and subsequent tensile deformation

When the anisotropic annealing behavior in HPT-deformed nickel was observed by Steyskal [21] and Oberdorfer [17], one of the proposed explanations was macroscopic residual stress caused by the plastic deformation. A macroscopic residual stress can be detected indirectly by applying a small, preferentially elastic deformation to the material after being processed by HPT. An elastic deformation increases the overall stress (being the sum of internal and external stresses) acting on the material. Once the overall stress exceeds the material's yield stress plastic flow occurs which reduces the residual stress.

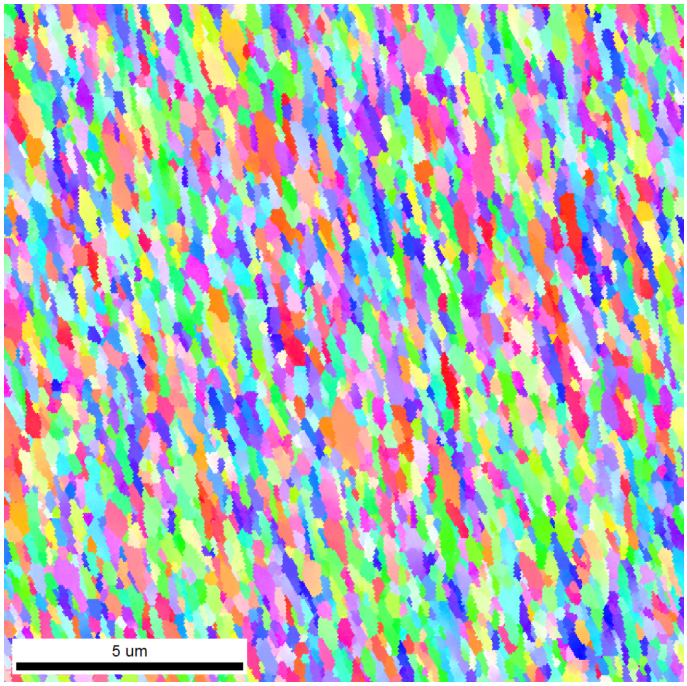

(a) Inverse pole figures map.

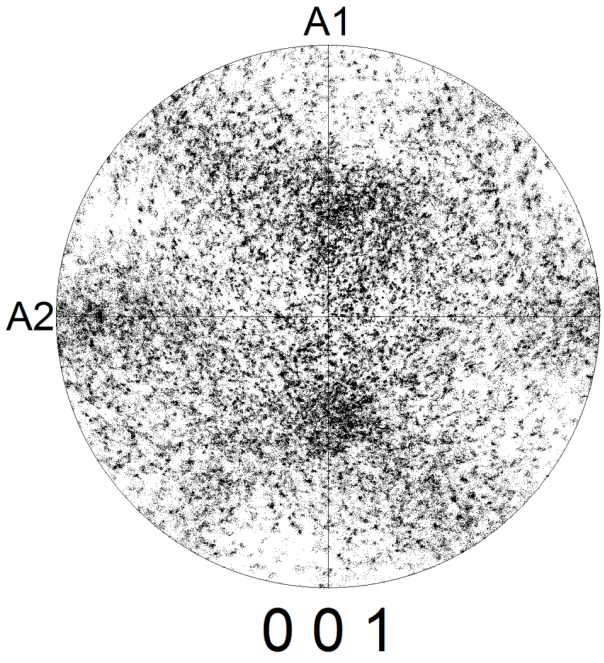

(b) Orientation map.

Figure 4.4: Results of the EBSD measurements performed on high-purity nickel deformed by HPT (specimen Ni5Tan). (a) The image shows the A-T plane of the specimen. (b) The image shows the orientation distribution map of the image (a).

Figure 4.5: Two tensile test samples were cut from the disc specimen Ni10Ten. One of which was elastically deformed ('Ni10Ten') and one which was not ('Ni10NTen'). Difference dilatometry samples were cut from the two tensile test samples.

According to this principle a nickel disc labeled 'Ni10Ten' (parts of the series were labeled 'Ni10NTen') was deformed by HPT for 10 turns under otherwise identical conditions as described in section 4.1.1. From this disc two tensile test samples were cut at the Erich Schmid Institute of Materials Science in Leoben. The tensile test samples are pictured in figure 4.5. One of the tensile test samples was left as is while the other was elastically deformed during a tensile test (the test was stopped when plastic deformation set in).

Four dilatometry samples in tangential orientation were cut from the undeformed tensile test sample ('Ni10NTen'). Two dilatometry samples in tangential orientation were cut from the elastically deformed tensile test sample ('Ni10Ten'). Figure 4.6 shows the result of the difference dilatometry measurments of the series Ni10NTen and Ni10Ten. The combined average length changes are listed in table 4.3.

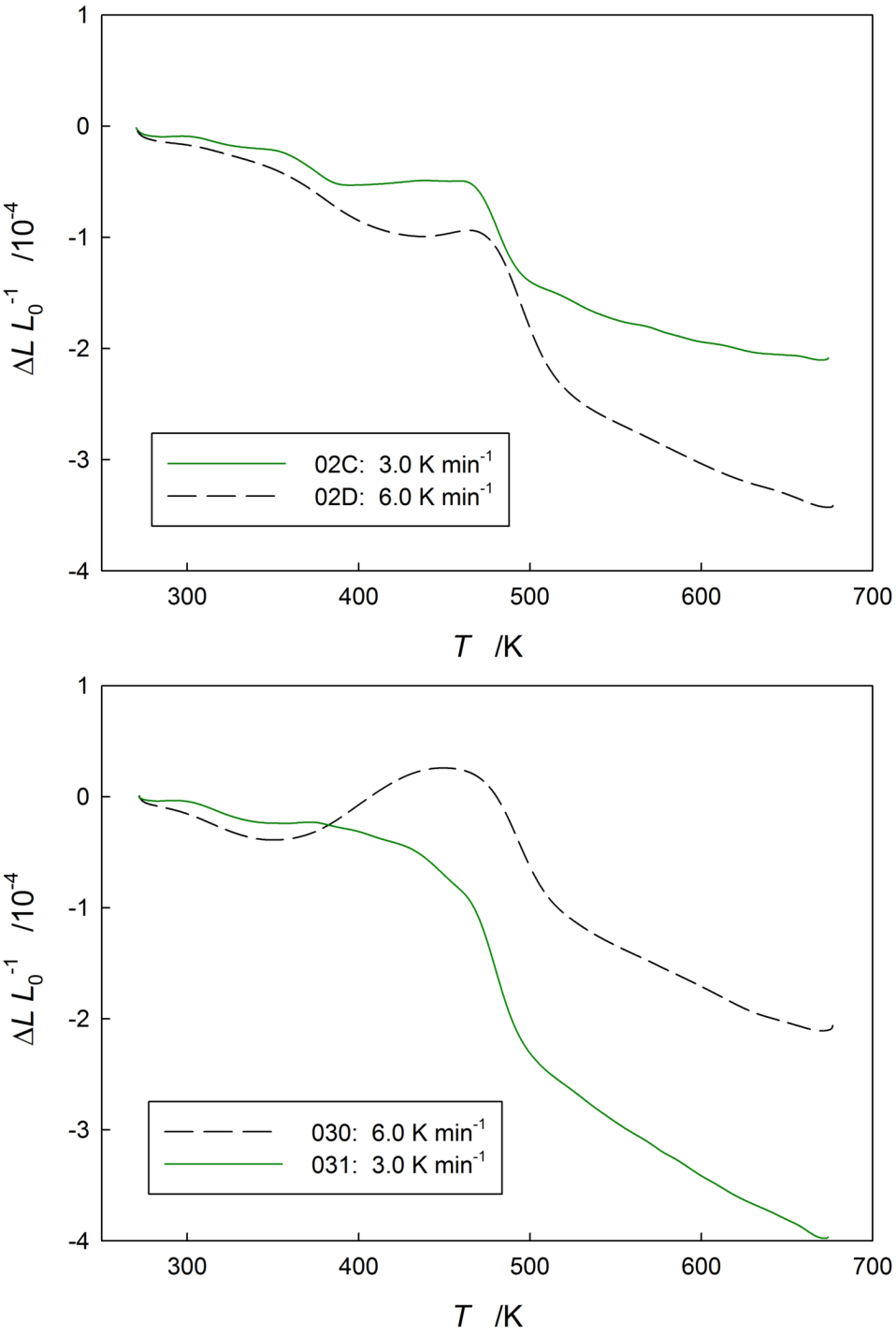

Figure 4.6: Exemplary difference dilatometry curves of samples in tangential orientation cut from the specimens Ni10Ten (top, deformation by HPT, 10 turns, subsequent tensile straining) and Ni10NTen (bottom, deformation by HPT, 10 turns).

Table 4.3: Average length changes during the three annealing stages A, B and C for samples of different orientations (Or.) cut from the disc specimen Ni10Ten. No. indicates the number of samples measured in this orientation.

Or.	No.	$\frac{\Delta L}{L_0}\Big\vert_A$ /10^{-4}	$\frac{\Delta L}{L_0}\Big\vert_B$ /10^{-4}	$\frac{\Delta L}{L_0}\Big\vert_C$ /10^{-4}
A	3	-1.11±0.34	-1.95±0.33	-1.57±0.16
T	3	-0.15±0.37	-1.03±0.24	-0.90±0.11

All measurements except for one show a plateau-like behavior during stage A. Only the sample from the elastically deformed tensile test sample measured at a heating rate of $6.0\,\mathrm{K\,min^{-1}}$ shows a pronounced length increase. Unfortunately, the results of these measurements are negatively affected by the requirements of the elastic deformation by tensile test: due to the shape of the tensile test samples the dilatometry samples are from a position close to the center of the specimen disc, and the dilatometry samples are not ideally tangential. However, the irreversible length increase in stage A can clearly be observed both in samples which were and which were not subjected to elastic post-deformation.

4.1.3 High-Pressure Torsion and subsequent cold rolling

As described in section 4.1.2 deformation by HPT with subsequent elastic deformation limits the available dilatometry samples to ones from the center of the disc specimen. In order to gain access to samples from the edge of a disc specimen, the elastic tensile deformation can be replaced by plastic deformation such as cold rolling. It is assumed that once plastic flow occurs in the deformed specimen the residual stress is relieved by the plastic flow [50].

Table 4.4: Average length changes during the three annealing stages A, B and C for samples of different orientations (Or.) cut from the disc specimen Ni16Tan. No. indicates the number of samples measured in this orientation.

Or.	No.	$\frac{\Delta L}{L_0}\Big\vert_A$ /10^{-4}	$\frac{\Delta L}{L_0}\Big\vert_B$ /10^{-4}	$\frac{\Delta L}{L_0}\Big\vert_C$ /10^{-4}
A	3	-2.78±0.08	-2.41±0.95	-2.55±0.14
T	24	+0.38±0.95	-0.80±0.38	-2.44±1.08

This measurement series consisted of two disc specimens being deformed by HPT which were labeled 'Ni16Tan' and 'Ni16CR'. Both discs were deformed for 16 turns of HPT each and the latter one ('Ni16CR') was plastically deformed by cold rolling afterwards. The disc was reduced to a thickness of 6 mm by multiple passes of 0.1 mm reduction each. From the disc specimen Ni16Tan 24 dilatometry samples in tangential and three samples in axial orientation were cut. From the cold rolled specimen Ni16CR eleven dilatometry samples in tangential orientation were cut. The figures 4.7a and 4.7b show overviews of the sample positions within the specimens Ni16Tan and Ni16CR respectively.

Figure 4.8 shows results from the measurements of samples in tangential orientation from the specimen Ni16Tan and Ni16CR. Unlike the results from the measurement series Ni5Tan (section 4.1.1) the results of these series show large differences in the annealing behavior during stage A. At low heating rates (1.5 K min^{-1}, 2.5 K min^{-1} and 3.0 K min^{-1}) the same length increase during stage A is observed as in the measurement series Ni5Tan. At high heating rates (5.0 K min^{-1} and 6.0 K min^{-1}) a plateau-like behavior is observed similar to the results from the measurement series Ni10Ten (section 4.1.2). The average length changes measured in samples from the two disc specimens are listed in the tables 4.4 (without cold rolling) and 4.5 (with cold rolling).

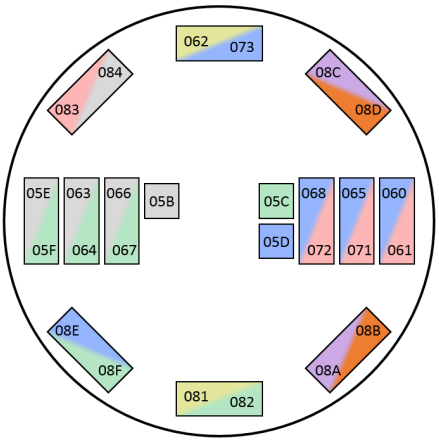

(a) Overview of the specimen 'Ni16Tan'.

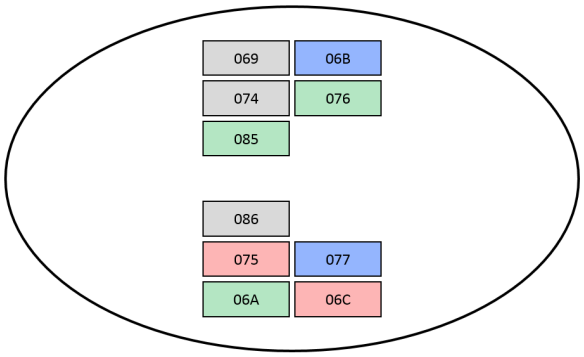

(b) Overview of the specimen 'Ni16CR'.

Figure 4.7: Overviews of the disc specimen 'Ni16Tan' (a) and the cold-rolled disc specimen 'Ni16CR' (b). The sample designations refer to the list of measurements in the appendix. The colors indicate the heating rates.

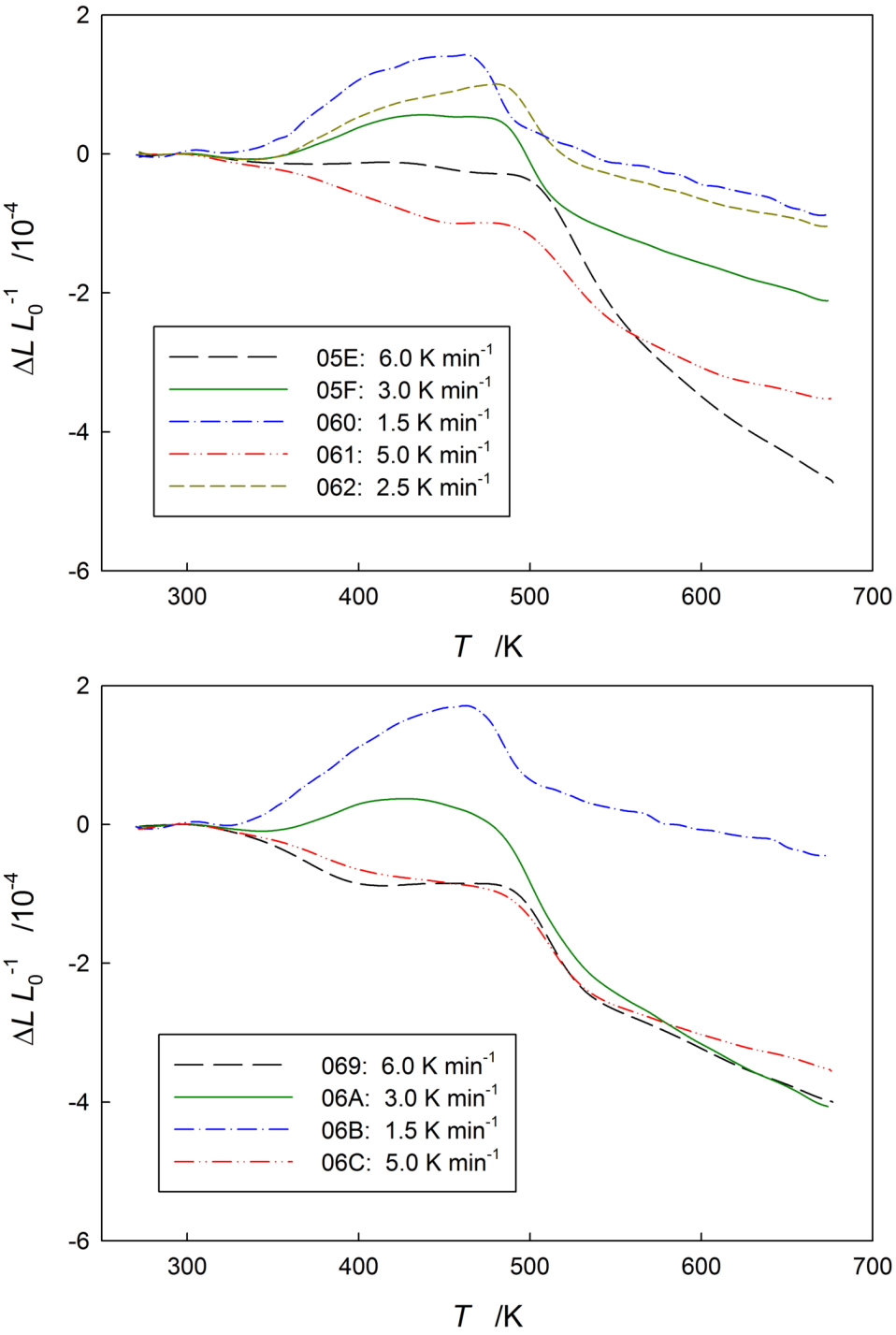

Figure 4.8: Exemplary difference dilatometry curves of samples in tangential orientation cut from the specimens Ni16Tan (top, deformation by HPT, 16 turns, without cold rolling) and Ni16CR (bottom, deformation by HPT, 16 turns, with cold rolling).

Table 4.5: Average length changes during the three annealing stages A, B and C for samples of tangential orientation (Or.) cut from the disc specimen Ni16CR. No. indicates the number of samples measured in this orientation.

Or.	No.	$\frac{\Delta L}{L_0}\Big\vert_A$ /10^{-4}	$\frac{\Delta L}{L_0}\Big\vert_B$ /10^{-4}	$\frac{\Delta L}{L_0}\Big\vert_C$ /10^{-4}
T	10	+0.33±0.87	-0.71±0.36	-2.03±0.44

Comparing the results from the specimen Ni16Tan with the results from the cold rolled specimen Ni16CR no difference can be observed. Figure 4.8 shows the results for dilatometry samples from the edges of the discs ($\varepsilon = 100$). Samples from closer to the center of the discs do not show the same heating rate dependence of samples from the edges. Nonetheless, still no difference between samples from the disc specimen Ni16Tan and the post-processed disc specimen Ni16CR is observed when samples from the center of the discs are considered.

Scanning electron microscopy images of samples cut from Ni16Tan as well as from Ni16CR were prepared. Figure 4.9 shows the microstructure of the Ni16Tan specimen in the axial-tangential plane. Figure 4.10 shows the microstructure of the Ni16CR specimen. Both images suffer from surface artifacts introduced during the surface preparation. The crystallite elongation is still well visible in both images.

For the sample from the Ni16Tan specimen an EBSD image was prepared too. This image is depicted in figure 4.11a. From the EBSD data an average crystallite size of (280±180) nm along the elongated direction and (110±40) nm perpendicular to the elongated direction can be calculated. This crystallite size gives an aspect ratio of 2.6. Figure 4.11b shows the corresponding pole figure derived from the EBSD data.

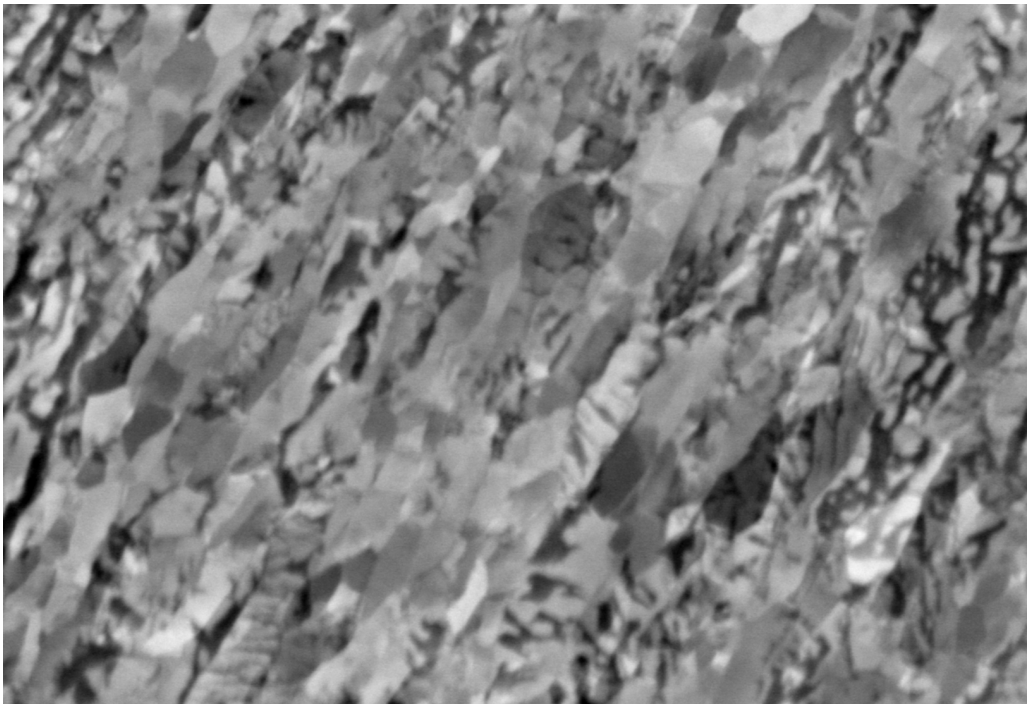

Figure 4.9: Scanning electron microscopy image of high-purity nickel deformed by HPT (specimen Ni16Tan). The image shows the A-T plane of the specimen. The image width is 5.72 µm.

A Kissinger analysis of stage B (data from 13 samples in tangential orientation from the measurement series Ni16Tan) reveals a strongly reduced activation energy of only $Q = (0.65 \pm 0.11)$ eV. This value is only half as high as the values derived from all earlier measurement series conducted on HPT-processed nickel. However, the temperatures at which the recrystallization rate is at a maximum are the same as the in the other measurement series.

4.1.4 Samples with bar-shaped bases

The above sections 4.1.2 and 4.1.3 describe the comparison of measurements with and without the relieve of potential macroscopic residual stresses by elastic or plastic deformation. If these stresses exist as stress gradients in the

Figure 4.10: Scanning electron microscopy image of high-purity nickel deformed by HPT and subsequent cold rolling (specimen Ni16CR). The image shows the A-T plane of the specimen. The image width is 5.72 µm.

dilatometry samples, they may be detected directly by difference dilatometry too. During heating such stress gradients would result in a distortion of the sample which could be mistaken for a length increase. In order to test this hypothesis, another series of measurements was performed.

Assuming that the observed length increase in samples of tangential orientation is instead a distortion of the sample by e.g. twisting or bending, then measuring the length change by differently shaped push rods will lead to different results. If only a rectangular area (about $0.75 \times 3\,\mathrm{mm}^2$) of the base is used to acquire the length change, then the position of the measurement area relative to the sample orientation influences the observed length change. In case the sample bends or twists in the AR plane, then the observed length increase will be lower when the long side of the acquisition

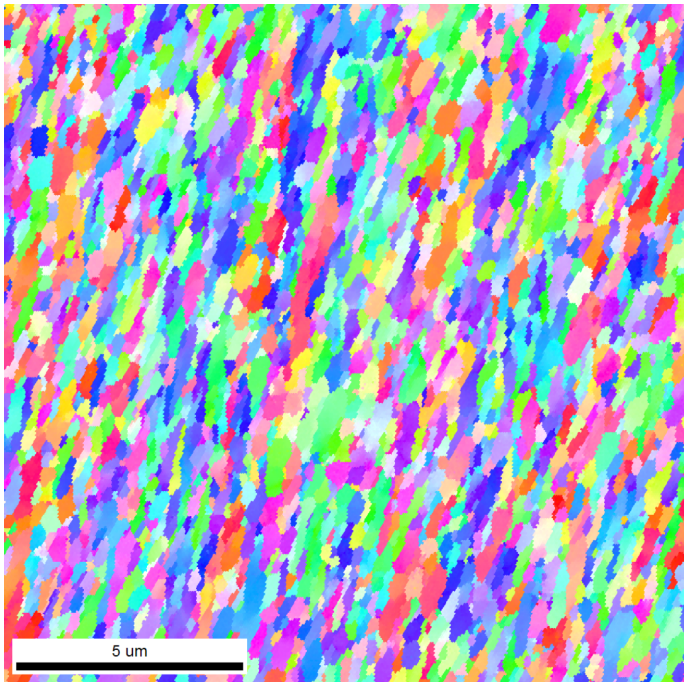

(a) Inverse pole figures map.

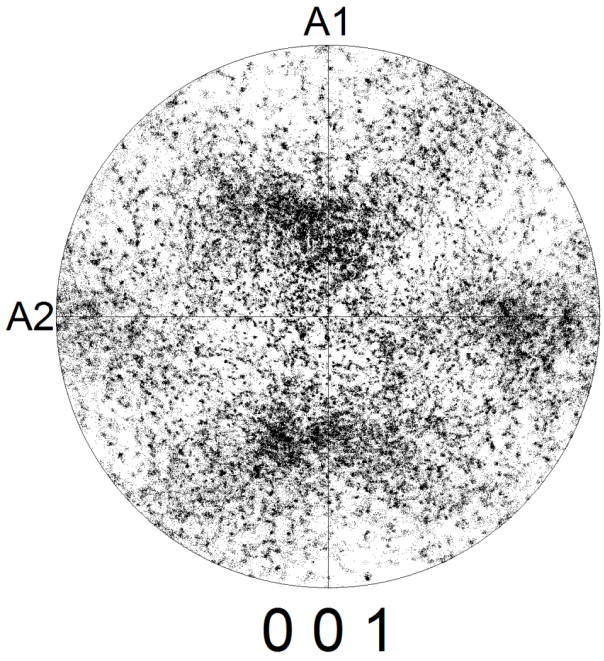

(b) Orientation map.

Figure 4.11: Results of the EBSD measurements performed on high-purity nickel deformed by HPT (specimen Ni16Tan). (a) The image shows the A-T plane of the specimen. (b) The image shows the orientation distribution map of the image (a).

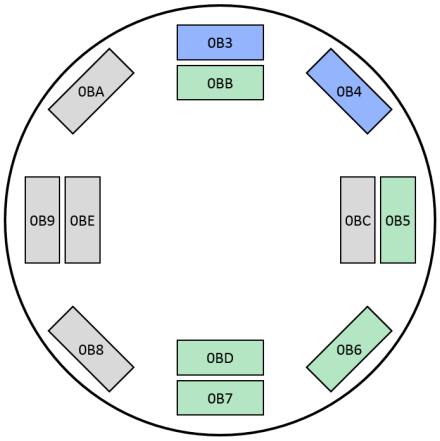

Figure 4.12: Overview of the disc specimen 'Ni5BB'. The sample designations refer to the list of measurements in the appendix. The colors indicate the heating rates.

area is parallel to the axial direction than when the long side is parallel to the radial direction

The concept described above relies on a rectangularly shaped push rod to acquire the length change of a dilatometry sample with a square base. The same result can be achieved by measuring a sample with a rectangular base with a traditional push rod, and the long side of the rectangular base being parallel to the axial or radial direction respectively. This can be simplified even further by using regular samples with square bases but a rectangular bar at the top base to acquire the length change from.

For this experiment a high-purity nickel disc was deformed under identical conditions as described in section 4.1.1 and cut into twelve dilatometry samples in tangential orientation. Figure 4.12 shows the relative positions of the dilatometry samples cut from this disc. The samples and measurements from this series were labeled 'Ni5BB'.

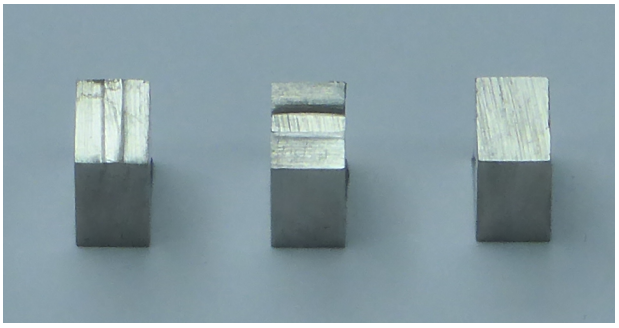

Figure 4.13: Close-up of the top bases of three samples cut from the measurement series Ni5BB. The left sample has a bar parallel to axial direction. The center sample has a bar parallel to radial direction. The right sample has a plane base.

Table 4.6: Average length changes during the three annealing stages A, B and C for samples of tangential orientation (Or.) cut from the disc specimen Ni5BB. No. indicates the number of samples measured in this orientation.

Or.	No.	$\frac{\Delta L}{L_0}\Big\vert_{\mathrm{A}}$ /10^{-4}	$\frac{\Delta L}{L_0}\Big\vert_{\mathrm{B}}$ /10^{-4}	$\frac{\Delta L}{L_0}\Big\vert_{\mathrm{C}}$ /10^{-4}
T	12	+0.63±0.48	-1.26±0.42	-2.23±0.76

After cutting out the dilatometry samples, one base each of the ten samples was ground until it was bar-shaped instead of plane. Figure 4.13 shows a close-up of three samples of the 'Ni5BB' series two of which have a bar-shaped base. The bases of these samples were ground down by about 0.5 mm on two sides of a roughly 0.75 mm wide bar. For five of those samples the bar was ground parallel to the axial direction and for the other five samples the bar was ground parallel to the radial direction

Figure 4.14 shows the difference dilatometry results of the measurement series Ni5BB. All samples show the length increase during stage A which is observed in samples with planar bases as well. No difference can be observed between samples with plane base, samples with an axially oriented bar, and samples with a radially oriented bar. The average length

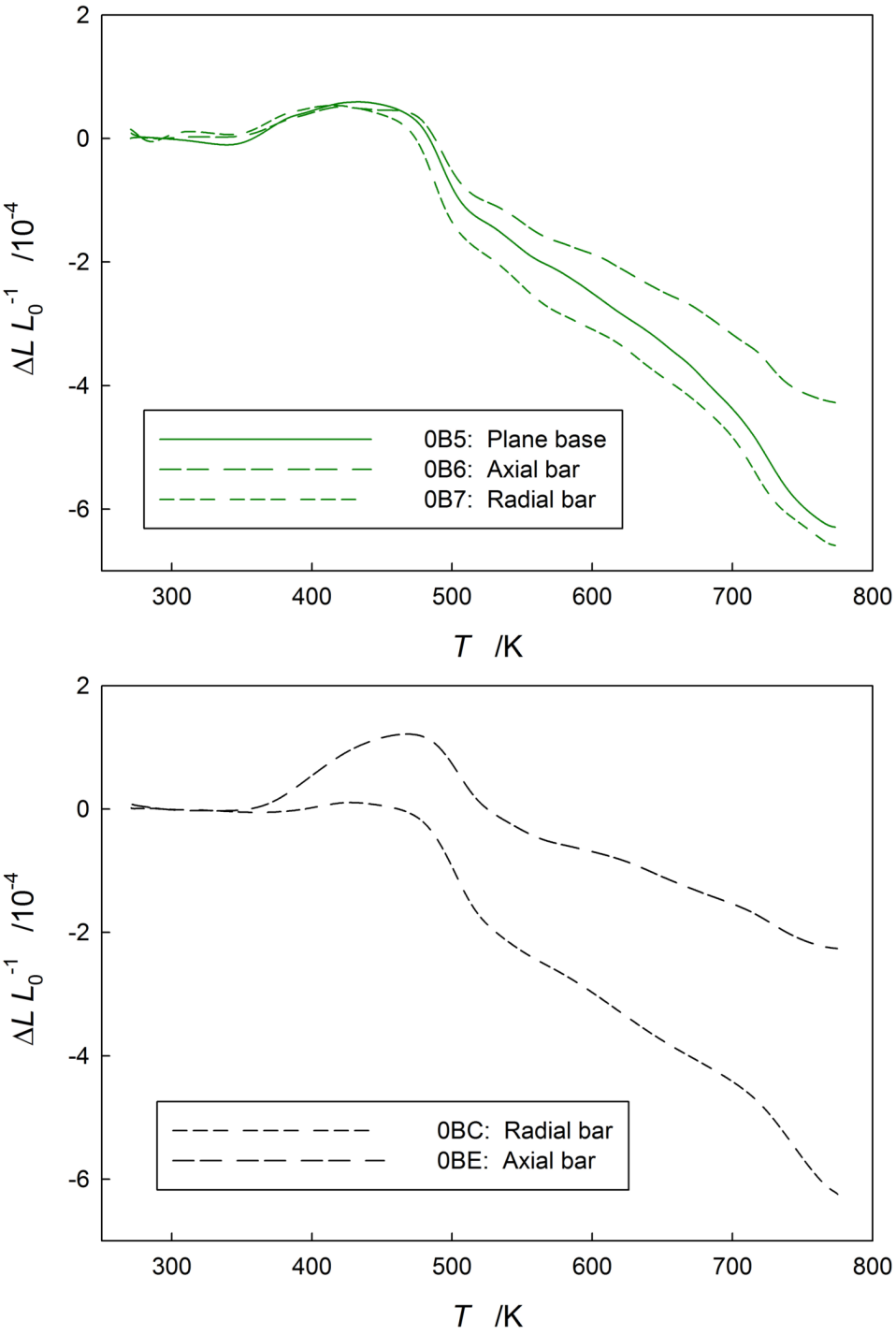

Figure 4.14: Exemplary difference dilatometry curves of samples in tangential orientation with bar-shaped bases cut from the specimen Ni5BB (deformation by HPT, five passes) with applied strains of $\varepsilon = 40$ (top, $\varphi = 3.0\,\mathrm{K\,min^{-1}}$) and of $\varepsilon = 30$ (bottom, $\varphi = 6.0\,\mathrm{K\,min^{-1}}$).

changes measured are listed in table 4.6. For stage B an activation energy of $Q = (1.17 \pm 0.11)\,\mathrm{eV}$ is calculated (from twelve samples in tangential orientation). This value is closer to the results from Steyskal [21] than the measurement series Ni5Tan.

4.2 Difference dilatometry after Equal-Channel Angular Pressing

For the ECAP deformations the same material was used as for the HPT deformations (see section 4.1). The deformations were performed either at the Institute of Materials Physics in Münster (section 4.2.1) or at the AIT Austrian Institute of Technology (section 4.2.2).

4.2.1 Preliminary results for deformation by ECAP

A measurement run for the purpose of overview was performed on nickel deformed by four passes of ECAP using the B_C route. The deformation was carried out by the group of G. Wilde from the Institute of Materials Physics at the University of Münster. From the resulting rod specimen four dilatometry samples were cut in extrusion orientation, three in transverse orientation and six in normal orientation. Figure 4.15 shows the positions and orientations of the samples cut from the rod specimen. The measurement run was labeled 'Ni4BC'.

Figure 4.16 shows a comparison of one sample each in extrusion, normal and transverse orientation from the series Ni4BC. Samples in transverse orientation feature an annealing behavior very similar to samples in axial

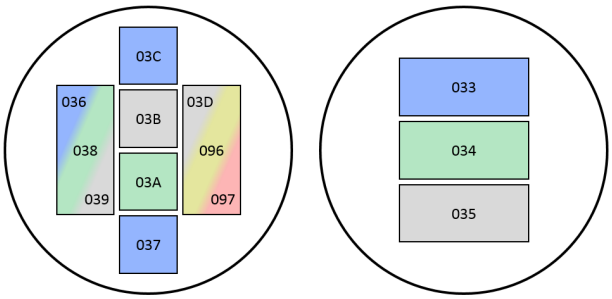

Figure 4.15: Overview of the rod specimen 'Ni4BC' viewed in the diameter. The rod specimen was initially cut into two parts of 7 mm (left) and 3 mm (left) height. The sample designations refer to the list of measurements in the appendix. The colors indicate the heating rates.

and radial orientation after deformation by HPT (compare figure 4.2). Again the annealing of defects can be divided into three well-separated stages. However, compared to deformation by HPT the stages are shifted to higher temperatures by almost 50 K.

Samples in normal and extrusion orientations, on the other hand, show neither a pronounced length decrease nor increase during stage A. In both orientations some of the samples show a slight length increase like samples in tangential orientation after deformation by HPT. However, other samples do not change their length irreversibly until shortly before the onset of recrystallization in stage B. The average length changes for each stage and orientation can be found in table 4.7.

The heterogeneity observed in the annealing behavior of the series Ni4BC also occurs in the microstructure of the rod specimen. Figure 4.17 shows an EBSD image of the E-N plane of the rod specimen. The image was taken by O. Renk from the Institute of Materials Science in Münster. The microstruc-

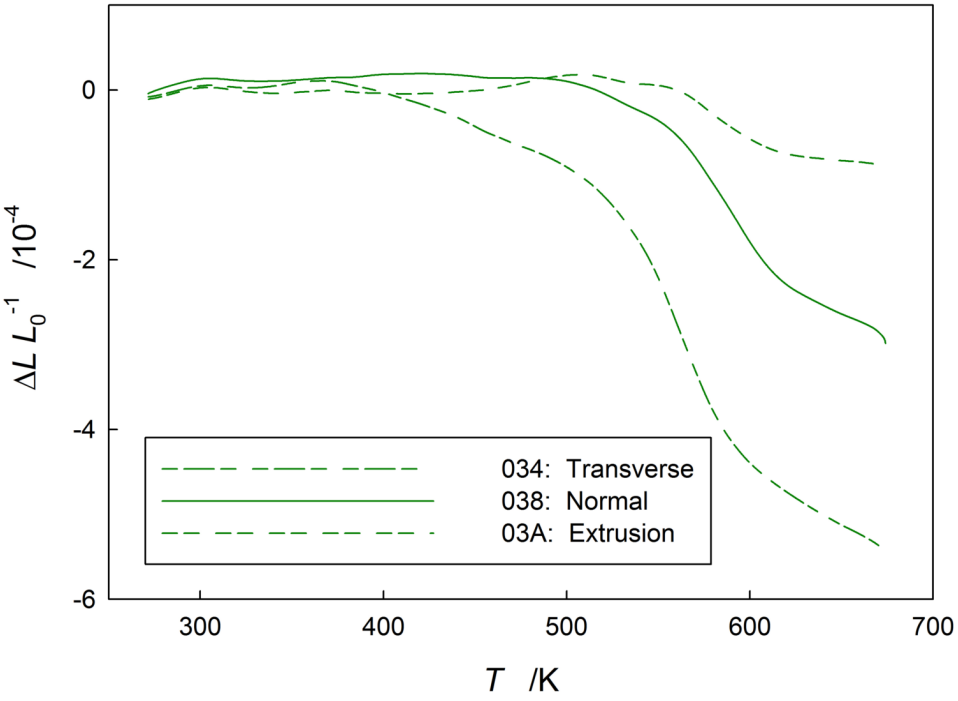

Figure 4.16: Exemplary difference dilatometry curves of samples in extrusion, normal and transverse orientations measured at heating rates of $\varphi = 3.0\,\mathrm{K\,min^{-1}}$ cut from the specimen Ni4BC (deformation by ECAP, four passes, route B_C).

Table 4.7: Average length changes during the three annealing stages A, B and C for samples of extrusion, normal and transverse orientations (Or.) cut from the rod specimen Ni4BC. No. indicates the number of samples measured in this orientation.

Or.	No.	$\frac{\Delta L}{L_0}\Big\vert_A$ /10^{-4}	$\frac{\Delta L}{L_0}\Big\vert_B$ /10^{-4}	$\frac{\Delta L}{L_0}\Big\vert_C$ /10^{-4}
E	4	+0.26±0.49	-0.42±0.18	-1.38±0.79
N	6	-0.11±0.47	-1.01±0.54	-1.92±1.10
V	3	-0.69±0.34	-2.14±0.70	-1.48±0.56

ture resulting from four passes by the B_C route is still very inhomogeneous which demands for a stronger deformation as presented in the following section.

4.2.2 Annealing behavior depending on orientation

In order to achieve more reproducible results by difference dilatometry, two more rod specimens were prepared by M. Krystian at the Center of Advanced Implant solution of the AIT Austrian Institute of Technology. In this case twelve passes of ECAP were applied using the routes A and B_C. These specimens and the corresponding measurement series were labeled 'Ni12A' and 'Ni12BC' respectively. An overview of all samples cut from the rod specimen can be seen in figures 4.18a for the series Ni12A and 4.18b for the series Ni12BC.

A total of 15 samples were cut from each of the rod specimens, five each in extrusion, normal and transverse orientation. In figure 4.19 the results for dilatometry measurements of differently oriented samples from both rod specimens are compared. The results of these measurement series are more

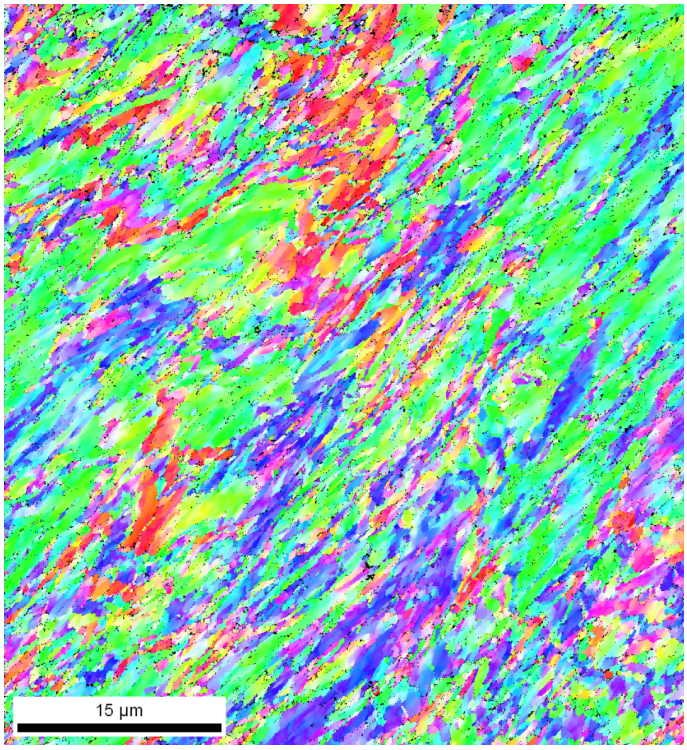

Figure 4.17: Results of the EBSD measurements performed on high-purity nickel deformed by ECAP (specimen Ni4BC). The image shows the E-N plane of the specimen.

reproducible than the first series after only four passes of ECAP. However, outliers did still occur in rare cases even after twelve passes of ECAP.

Compared to the annealing behavior after deformation by HPT even after twelve passes of ECAP the annealing stages are still shifted to higher temperatures (by about 50 K). Apart from this temperature shift the samples deformed by ECAP behave very similar to samples deformed by HPT. The three stages A, B and C are well separated, and a clear orientation dependence can be observed.

In normal and transverse orientation a similar behavior with an irreversible length decrease in stage A is observed as in axial and radial orientation af-

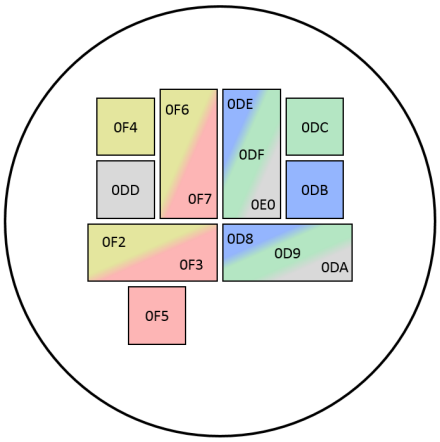

(a) Overview of the specimen 'Ni12A'.

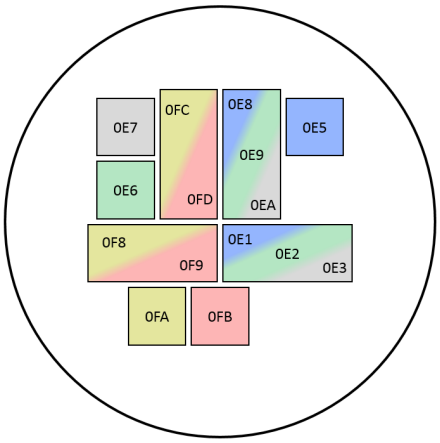

(b) Overview of the specimen 'Ni12BC'.

Figure 4.18: Overviews of the rod specimens 'Ni12A' (a) and 'Ni12BC' (b) both deformed by ECAP. The sample designations refer to the list of measurements in the appendix. The colors indicate the heating rates.

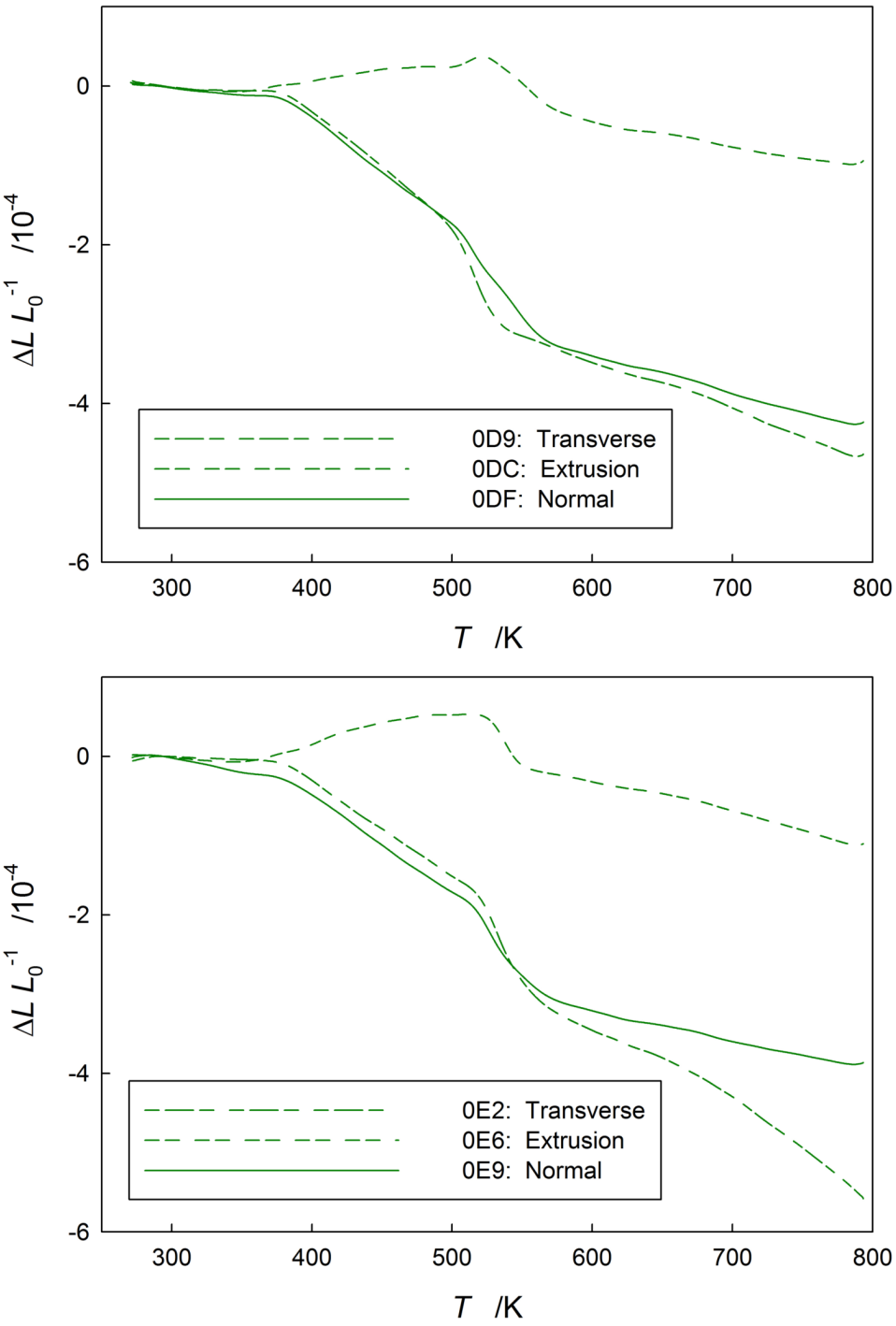

Figure 4.19: Exemplary difference dilatometry curves of samples in extrusion, normal and transverse orientations measured at heating rates of $\varphi = 3.0\,\mathrm{K\,min^{-1}}$ cut from the specimens Ni12A (top, deformation by ECAP, 12 passes, route A) and Ni12BC (bottom, deformation by ECAP, 12 passes, route B_C).

Table 4.8: Average length changes during the three annealing stages A, B and C for samples of extrusion, normal and transverse orientations (Or.) cut from the rod specimen Ni12A. No. indicates the number of samples measured in this orientation.

Or.	No.	$\frac{\Delta L}{L_0}\Big\vert_{\mathrm{A}}$ /10^{-4}	$\frac{\Delta L}{L_0}\Big\vert_{\mathrm{B}}$ /10^{-4}	$\frac{\Delta L}{L_0}\Big\vert_{\mathrm{C}}$ /10^{-4}
E	4	+0.37±0.22	-0.59±0.10	-0.36±0.08
N	4	-1.53±1.00	-1.76±0.21	-0.48±0.18
V	5	-1.65±0.20	-1.55±0.37	-0.47±0.09

ter deformation by HPT. In extrusion orientation a similar behavior with an irreversible length increase in stage A occurs as in tangential orientation after deformation by HPT. However, the amplitudes of those length changes is smaller after deformation by ECAP as can be seen in table 4.8 for the measurement series Ni12A and in table 4.9 for the measurement series Ni12BC.

After deformation by route B_C (Ni12BC) an average length decrease of ${}^{\Delta L}/_{L_0}|_A = -1.21\times10^{-4}$ in transverse and an average length increase of ${}^{\Delta L}/_{L_0}|_A = +0.30\times10^{-4}$ in extrusion orientation is found. After deformation by route A (Ni12A) a length decrease of ${}^{\Delta L}/_{L_0}|_A = -1.65\times10^{-4}$ in transverse and a length increase of ${}^{\Delta L}/_{L_0}|_A = +0.37\times10^{-4}$ in extrusion orientation is measured. For comparison after deformation by HPT length changes of ${}^{\Delta L}/_{L_0}|_A = -2.44\times10^{-4}$ in axial and ${}^{\Delta L}/_{L_0}|_A = +0.89\times10^{-4}$ in tangential orientation are observed.

A similarly reduced amplitude is observed during stage B as well. In the Ni12A series, average length changes of ${}^{\Delta L}/_{L_0}|_B = -1.55\times10^{-4}$ in transverse and of ${}^{\Delta L}/_{L_0}|_B = -0.59\times10^{-4}$ in extrusion orientation are measured. In the Ni12BC series, similar values of ${}^{\Delta L}/_{L_0}|_B = -1.54\times10^{-4}$ in transverse

Table 4.9: Average length changes during the three annealing stages A, B and C for samples of extrusion, normal and transverse orientations (Or.) cut from the rod specimen Ni12BC. No. indicates the number of samples measured in this orientation.

Or.	No.	$\frac{\Delta L}{L_0}\Big\vert_A$ /10^{-4}	$\frac{\Delta L}{L_0}\Big\vert_B$ /10^{-4}	$\frac{\Delta L}{L_0}\Big\vert_C$ /10^{-4}
E	5	+0.30±0.39	-0.88±0.20	-0.42±0.16
N	5	-1.39±0.45	-1.60±0.40	-0.39±0.20
V	5	-1.21±0.22	-1.54±0.52	-0.42±0.29

and of $^{\Delta L}/_{L_0}|_B = -0.88{\times}10^{-4}$ in extrusion orientation are observed. Deformation by HPT on the other hand results in average length changes of $^{\Delta L}/_{L_0}|_B = -2.93{\times}10^{-4}$ in axial and of $^{\Delta L}/_{L_0}|_B = -1.32{\times}10^{-4}$ in tangential orientation.

Since the length change occurring in stage B is tied to the grain boundary excess volume and the crystallite size, the lower amplitudes resulting from deformation by ECAP imply a smaller crystallite size. Figures 4.20 and 4.21 show electron microscopy images of the microstructure after deformation by ECAP using the A route (figure 4.20) and the B_C route (figure 4.21). Compared to the microstructure resulting from deformation by HPT (figure 4.3) the crystallite size appears indeed larger.

Applying the line intercept method under the same parameters as described in section 4.1 on the image from the microstructure after deformation by the A route yields crystallite sizes of (423±49) nm along the elongated direction and (270±16) nm perpendicular to the elongated direction. After deformation by the B_C route the crystallite size equals to (372±61) nm along the elongated direction and (298±41) nm perpendicular to the elongated direction.

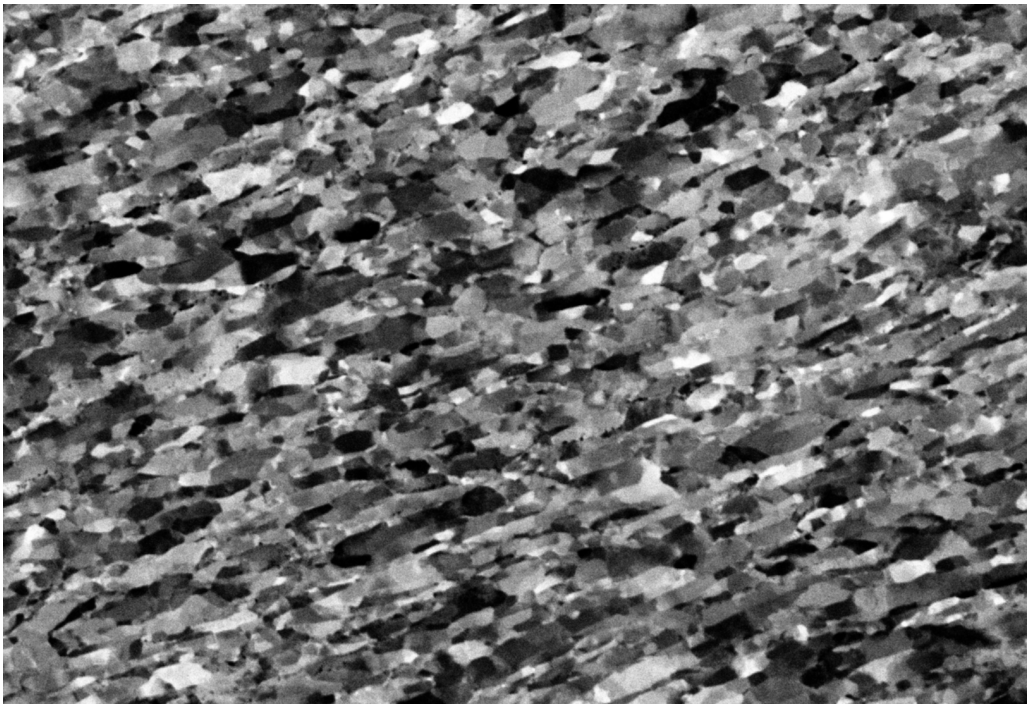

Figure 4.20: Scanning electron microscopy image of high-purity nickel deformed by ECAP (specimen Ni12A). The images show the E-N plane of the specimen. The image width is 5.72 µm.

The aspect ratios are therefore 1.6 for the Ni12A series and 1.2 for the Ni12BC series. These values are well below the aspect ratio typically found after deformation by HPT. In case of the Ni12A series (figure 4.20) the microstructure appears quite homogeneous and the crystallites appear elongated uniformly. However, in case of the Ni12BC series (figure 4.21) the microstructure shows areas of large, strongly elongated crystallites as well as areas of smaller, rather equiaxed crystallites.

A Kissinger analysis of stage B using the results from the samples of normal and transverse directions (five samples each for each measurement series) yield activation energies of (1.21±0.10) eV for the specimen Ni12A and (1.42±0.24) eV for the specimen Ni12BC. The activation energy of the rod specimen deformed by twelve passes of ECAP along the route A (Ni12A)

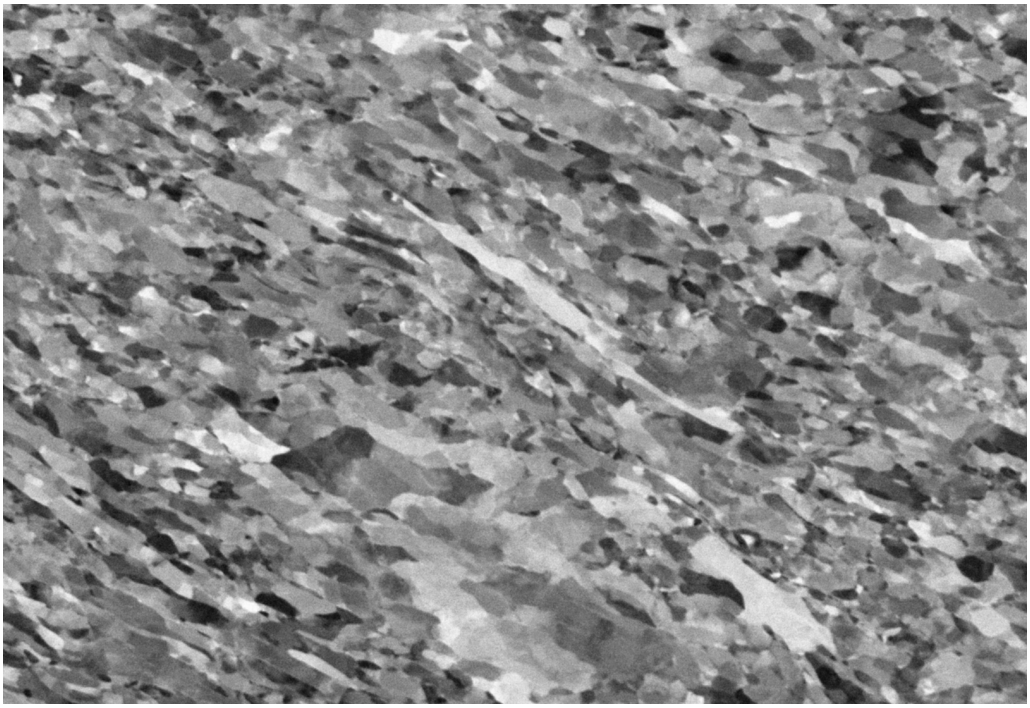

Figure 4.21: Scanning electron microscopy image of high-purity nickel deformed by ECAP (specimen Ni12BC). The images show the E-N plane of the specimen. The image width is 5.72 µm.

matches the activation energy of the disc specimen deformed by five turns of HPT (Ni5Tan) very well. The second rod specimen deformed along the route B_C shows a slightly higher activation energy though.

4.2.3 Ultrafine-grained titanium

A single series of measurements were also performed on commercially pure titanium. The deformation of the titanium specimen by ECAP and the sample preparation were performed at the Institute of Physics of ASCR (Czech Academy of Sciences) in Prague. The composition of the material is listed in table 4.10 (according to Jäger et al [51]), and the deformation consisted of four passes of ECAP by the A route. The measurement series was labeled Ti4A.

Table 4.10: Chemical composition of the commercial-purity titanium used for the majority of the measurements below. The composition was provided by the group of Tesař [51].

Element	Concentration /wt. ppm
Ti	Balance
Fe	0.165
C	0.009
N	<0.001
O	0.049
H	<0.001

In total three samples in normal orientation were measured, as well as two samples each in transverse and extrusion orientation. Figure 4.22 shows a comparison of the annealing behavior for the different sample orientations. In contrast to high-purity nickel, commercial-purity titanium is an hcp metal and deformation by ECAP leads to a strong texture [52, 53]. Therefore, titanium processed by ECAP shows an orientation-dependence of the coefficient of thermal expansion. This effect is clearly seen by the different slopes at the beginning of the difference curves. Furthermore, recovery stages span larger temperature windows than recrystallization stages and are thus more difficult to identify. Because of these named reasons, in the difference dilatometry of titanium the derivative curves gain significance compared to the difference curves.

As seen in figure 4.22 titanium processed by ECAP also shows an anisotropic annealing behavior. Samples in normal orientation behave similarly to nickel samples in extrusion orientation: an irreversible length increase is observed in the temperature regime of 350 to 450 K, followed by a drawn-out length decrease up to about 740 K, and a subsequent sharp length decrease. In transverse orientation a length decrease is observed between about 350 to

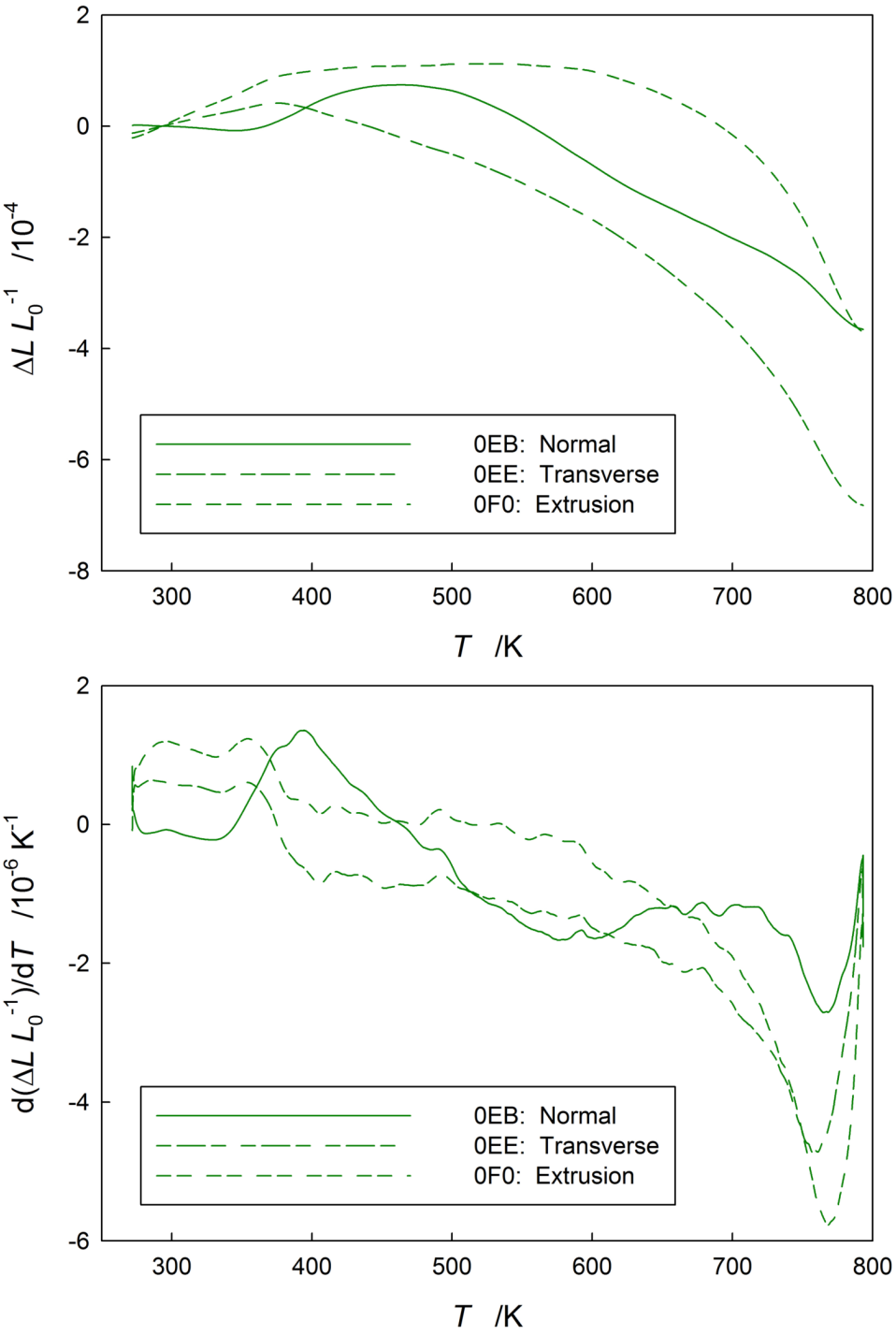

Figure 4.22: Exemplary difference dilatometry curves (top) and their derivatives (bottom) of ultrafine-grained titanium samples in extrusion, normal and transverse orientations cut from the specimen Ti4A (deformation by ECAP, four passes, route A); heating rate $\varphi = 3.0\,\mathrm{K\,min^{-1}}$.

740 K which is again followed by a sharp length decrease. In extrusion orientation a plateau-like behavior occurs in the temperature regime of 350 to 600 K, followed by a slight length decrease up to about 740 K, and a sharp length decrease.

However, for samples in extrusion orientation a strong heating rate dependence of the annealing behavior is observed. With a heating rate of 3.0 K min^{-1} (depicted in figure 4.22) a plateau-like behavior is observed from 350 to 600 K. With a heating rate of 6.0 K min^{-1} instead a length decrease up to about 470 K occurs followed by a length decrease up to about 600 K. The full set of difference dilatometry curves can be found in the appendix (figures 6.27, 6.28 and 6.29).

The three derivative curves of the difference curves show a slope close to zero up to about 350 K, but the orientation dependence in this temperature regime is presumably caused by a strong texture. At about 350 to 370 K the values drop both in transverse and extrusion direction. In normal direction a maximum is observed beginning at this temperature regime which might indicate a recovery process due to the broadness of the peak. At about 490 K a change of the slope indicates the beginning of an annealing process which lasts to the onset of recrystallization at about 720 K.

4.3 Neutron diffraction measurements of ultrafine-grained nickel

Difference dilatometry can only indirectly detect residual stresses by the volume change during the annealing of residual stress. In order to directly detect residual stresses by non-destructive means one has to use ultrasonic

testing [54] or diffraction techniques [55]. During this thesis neutron diffraction measurements were performed at the FRM-II in Garching on nickel processed by HPT and by ECAP.

For these measurements two disc specimens were prepared by HPT under the same conditions as described in section 4.1.1. From one of the disc specimens nine dilatometry-shaped samples were cut – three of each orientation. For the samples processed by ECAP remaining parts from the measurement series ('Ni12BC') described in section 4.2 were used. Six dilatometry-shaped samples were cut out of this rod specimen – two of each orientation. Figure 4.23 shows the positions of the samples relative to the disc specimen. In preparation of the neutron diffraction measurements, six of these dilatometry-shaped samples – three processed by HPT and three by ECAP – of different orientations were annealed at 770 K. Furthermore, two dilatometry-shaped samples were cut from an unused disc specimen which was processed by HPT under the conditions described before. One of those was annealed at about 950 K in a high vacuum oven beforehand to be used as reference.

During the first measurement run the complete disc specimen was scanned four times through the center of the disc. The first scan measured the lattice spacing d_{311} in tangential orientation by the angular shift 2θ of the (311) plane reflection. The second scan determined the lattice spacing in radial orientation, and in the third and fourth scans the procedure was repeated for the lattice spacing in axial orientation. Figure 4.24a shows the measurement setup applied during the scan runs.

Figure 4.25 shows the scan of the peak position 2θ along the disc specimen i.e. relative to the distance from the center of the disc specimen processed by HPT. At the center of the disc specimen a diffraction angle of about $2\theta = 93.99°$ independent of the direction can be observed. A similar value is observed at the edges of the disc specimen as well. Between the center

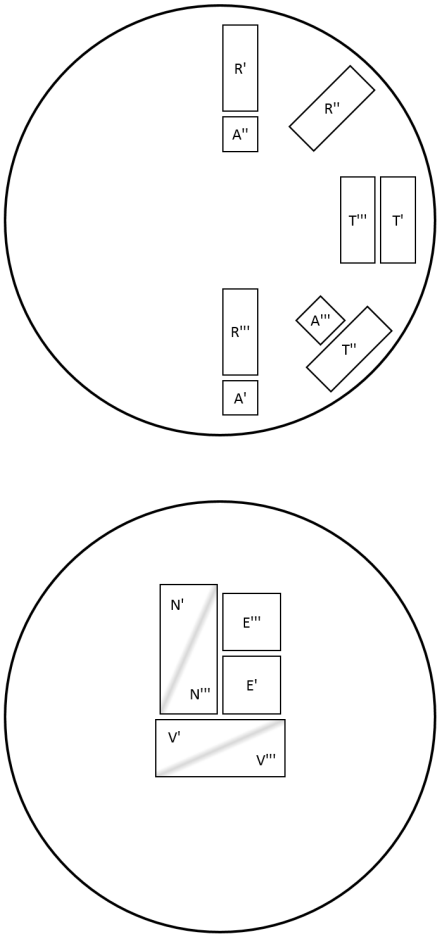

Figure 4.23: Overviews of the disc specimen prepared by HPT (top) and the rod specimen prepared by ECAP (bottom) for the neutron diffraction measurements. The samples marked with single and double primes were used for annealing measurements where the latter were annealed to 770 K beforehand. The samples marked with triple primes were used for $\sin^2 \psi$ measurements.

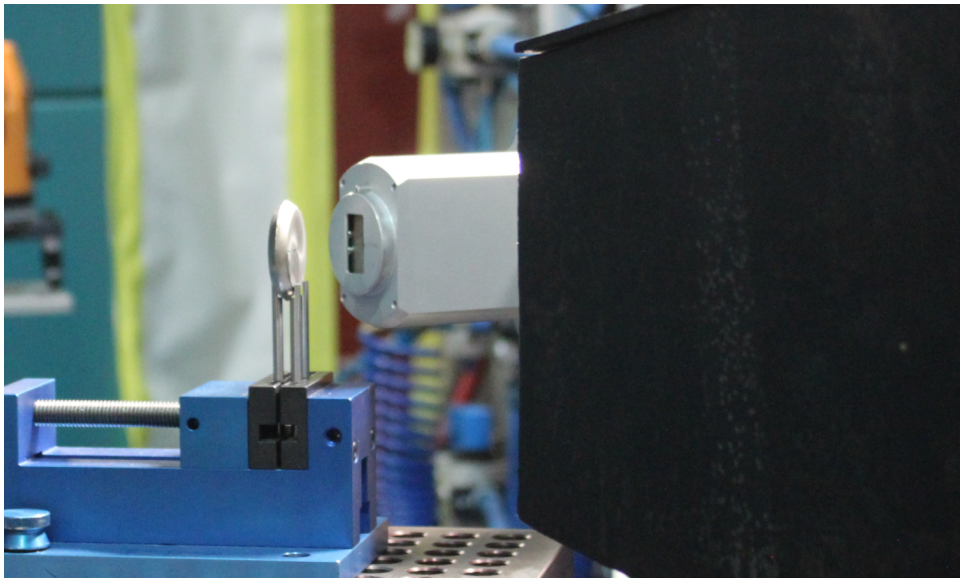

(a) Setup for the neutron diffraction measurements of the disc specimen.

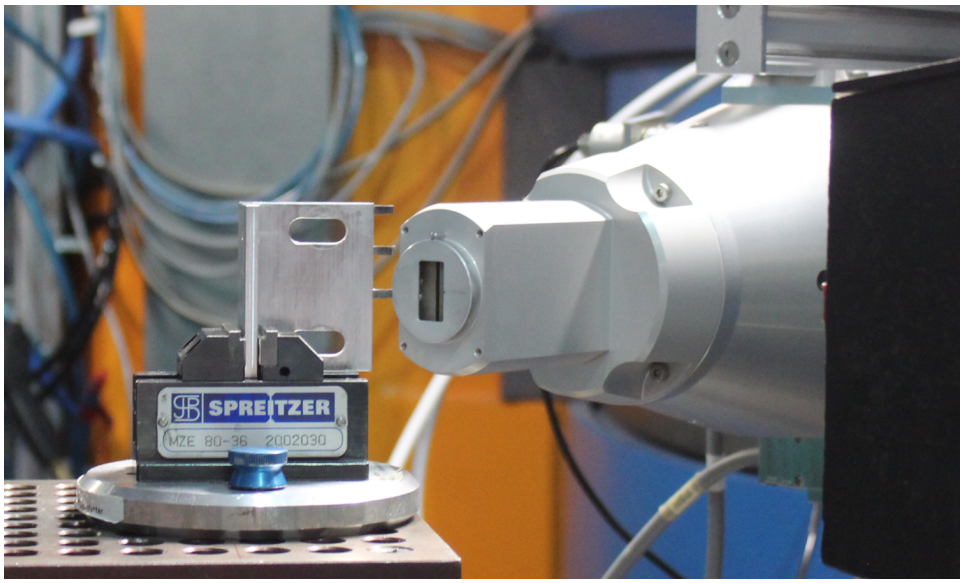

(b) Setup for the neutron diffraction measurements of dilatometry-shaped samples.

Figure 4.24: Measurement setup for the neutron diffraction measurements (see figure 3.10 for an overview). The detector can bee seen on the right hand side and the secondary collimator in the background. (a) Measurement of the bulk disc specimen. (b) Measurement of dilatometry-shaped samples (three per holder).

and the edges though the 2θ angles strongly depend on the orientation. In tangential orientation the 2θ angles are reduced while in axial orientation the 2θ angles are increased. In radial orientation neither an increase nor a reduction is observed.

From figure 4.25 one can assume that the center and edges are stress-free. In that case the results indicate the absence of macroscopic residual stresses in the radial direction, compressive stresses in axial direction (in areas between the center and the edge) and tensile stresses in tangential direction (in the same areas). The increase and decrease of 2θ in axial and tangential directions would suggest macroscopic residual stresses in the order of 1.2×10^{-2} and -1.6×10^{-2} respectively.

The second measurement run consisted of measuring the 2θ shift of the (311) peak in dilatometry-shaped samples depending on sample orientation and annealing state. The setup for this measurement run can be seen in figure 4.24b. Two sets, each of three dilatometry samples of different orientations one prepared by HPT and the other set of samples prepared by ECAP, were used. These six samples were measured at three annealing states each: the as-prepared state, after annealing to the end of stage A, and after annealing to the end of stage B. These measurements were complemented by measurement of a set of dilatometry-shaped samples (three each) pre-annealed at 770 K.

Figure 4.26 shows the measurement results of the 2θ position of the six described dilatometry-shaped samples at the four annealing states. Additionally, both figures also contain the 2θ value for the dilatometry-shaped sample cut from the unused disc specimen which was annealed at 950 K. Furthermore, the top figure (samples prepared by HPT) contains the second dilatometry-shaped sample from the unused disc specimen (this sample was not annealed to 950 K). Three additional dilatometry-shaped samples

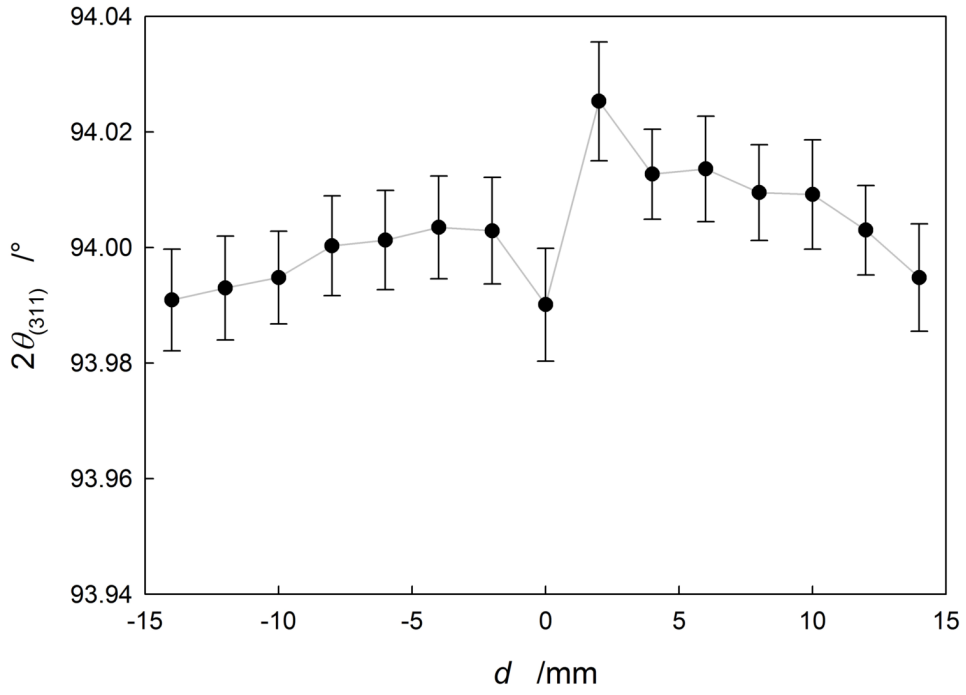
94.04
94.02
94.00
93.98
93.96
93.94
$2\theta_{(311)}$ /°
-15
-10
-5
0
5
10
15
d /mm

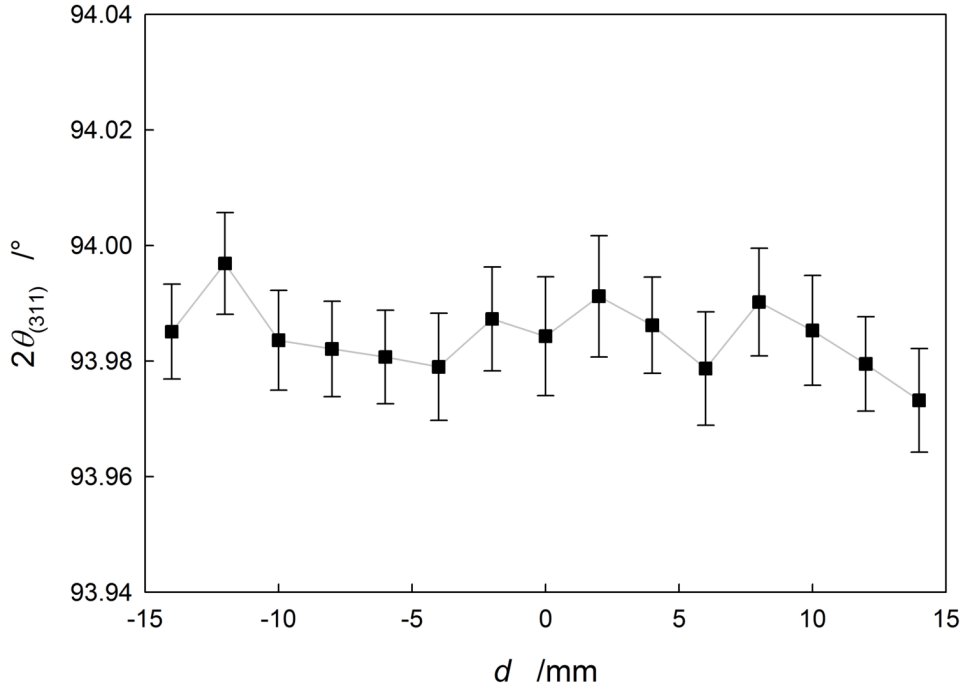
94.04
94.02
94.00
93.98
93.96
93.94
$2\theta_{(311)}$ /°
-15
-10
-5
0
5
10
15
d /mm

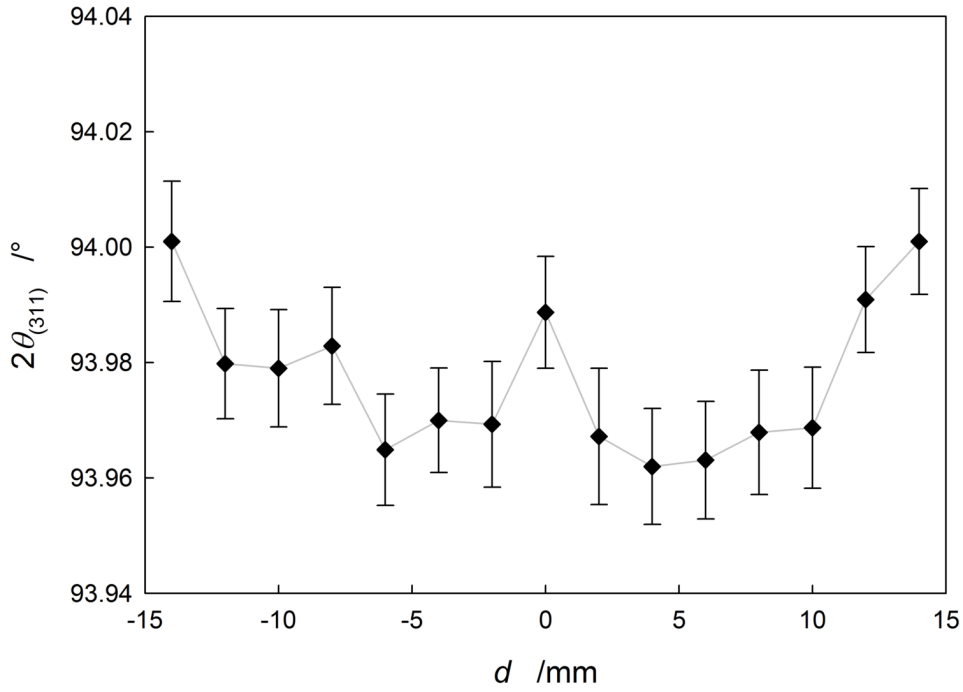

Figure 4.25: Scan of the peak position 2θ of the (311) reflection along the disc where d is the distance from the center of the bulk disc specimen. Measurement in axial (top left), radial (bottom left) and tangential (right) orientations.

in the as-prepared state (which were used for $\sin^2\psi$ measurements later) of different orientations prepared by HPT are shown in the top image as well.

In the as-prepared state no clear orientation dependence can be observed in samples processed by HPT. Furthermore, annealing up to completion of stage A and of stage B does not seem to have a significant influence on the measured 2θ values. After annealing to the end of stage C the 2θ values spread very strongly. This effect can be explained by the marked increase of the crystallite size which reduces the number of actively diffracting crystallites.

The samples processed by ECAP on the other hand indicate an orientation dependence. In the as-prepared state as well as after annealing to 500 K (end of stage A), the sample in extrusion orientation shows a higher 2θ value than the sample in normal orientation which in turn shows a higher value than the sample in transverse orientation (see figure 4.26). This effect is removed by annealing to 570 K (end of stage B).

The 2θ position is obtained by fitting a Gaussian function to the (311) peak in the 2θ spectrum. However, only residual stresses of the first or second order (macroscopic residual stress) lead to a shift of the peak. Residual stresses of the third order (microscopic residual stress), on the other hand, lead to a broadening of the peak. Therefore, plotting the full width at half maximum (FWHM) over the annealing state gives an insight into the defect concentrations after each stage.

Figure 4.27 shows the peak broadening in dependence to the annealing state. The shape of the curves closely resemble the annealing curves obtained from difference dilatometry. During stage A the FWHM is reduced only slightly in the samples processed by HPT and even less in the samples processed by

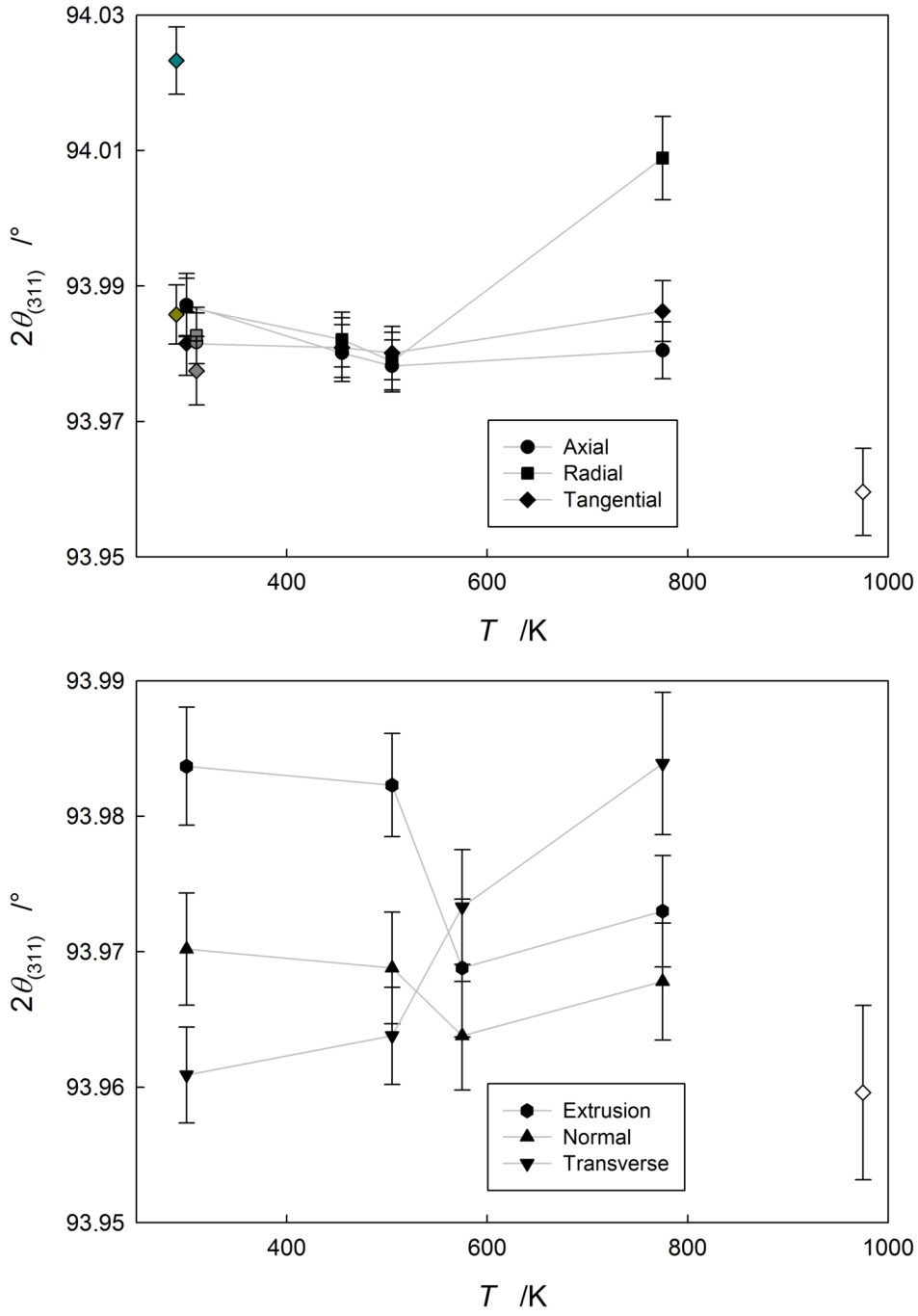

Figure 4.26: Variation of the peak position 2θ of the (311) reflection with annealing temperature T of dilatometry-shaped samples processed by HPT (top) and ECAP (bottom). The top graph contains three samples prepared for later measurements (grey) and a sample cut from an unused disc specimen (green). Both graphs also contain a dilatometry-shaped sample cut from an unused disc specimen and annealed at 950 K (white).

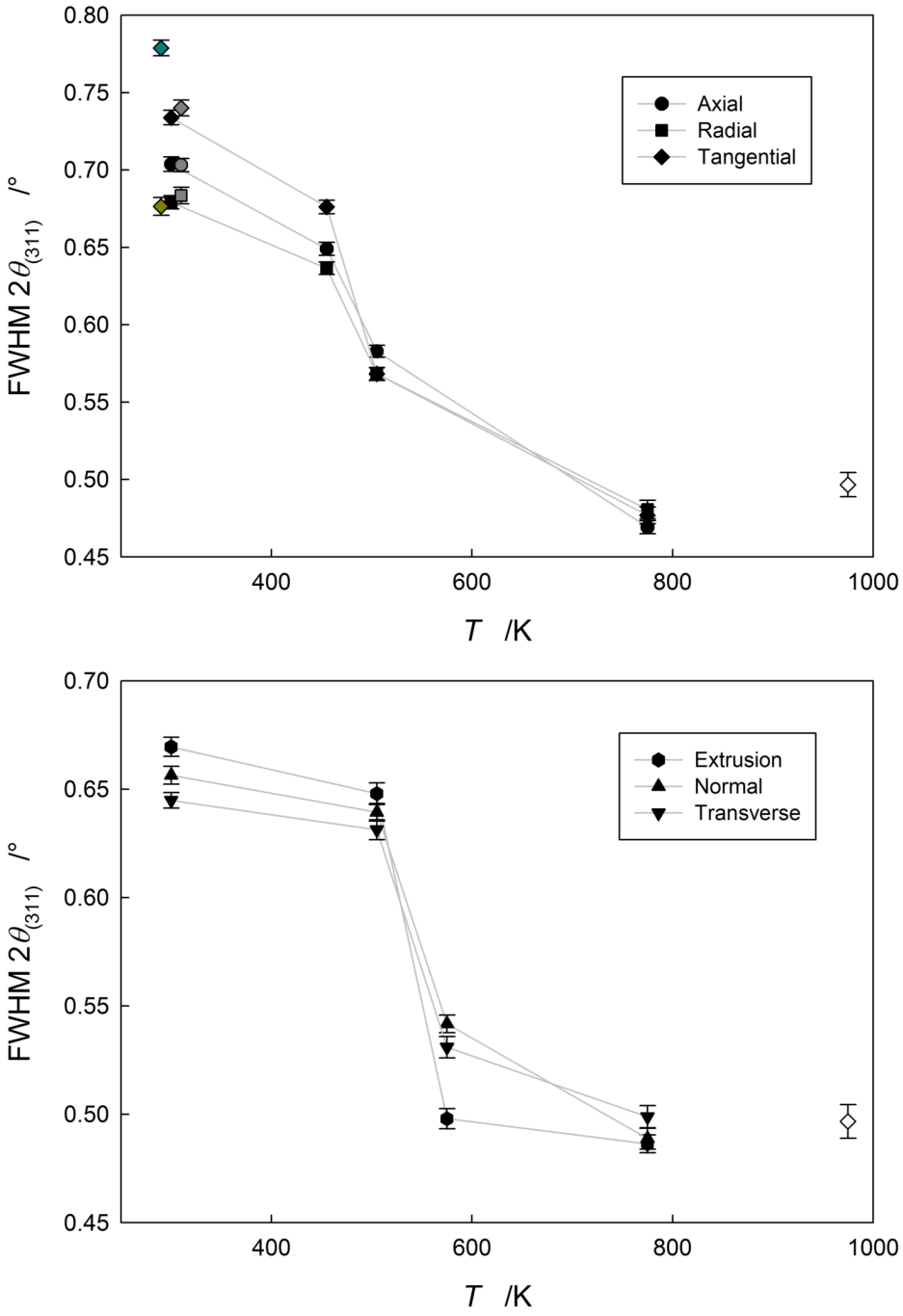

Figure 4.27: Measurement of the peak broadening FWHM (full width at half maximum) of the diffraction peak from the (311) plane with annealing temperature T of dilatometry-shaped samples processed by HPT (top) and ECAP (bottom). The top graph contains three samples prepared for later measurements (grey) and a sample cut from an unused disc specimen (green). Both graphs also contain a dilatometry-shaped sample cut from an unused disc specimen and annealed at 950 K (white).

ECAP. The recrystallization in stage B leads to a sharp drop of the FWHM which proceeds until annealing to about 770 K.

In the third measurement run the three additional dilatometry-shaped samples were measured with the $\sin^2\psi$ method. The results are displayed in figure 4.28. All three samples show a more (axial and tangential orientations) or less (radial orientation) pronounced oscillating behavior which indicates a microtexture [44]. Furthermore, the sample in axial and the sample in tangential orientation show clear signs of ψ-splitting. This effect occurs when either the ε_{13} or the ε_{23} or both stress components are non-zero [44]. In none of the three samples a considerable slope can be observed, however.

The final measurement run was a texture measurement for which the three dilatometry-shaped samples from the $\sin^2\psi$ measurements were used. The samples were positioned upright in the Eulerian cradle i.e. with the long sides of the samples perpendicular (independent of ϕ and χ angles) to the incident neutron beam. For the texture measurement the (111) and (200) reflections were used.

Figure 4.29 shows the (111) and (200) pole figures derived from the texture measurements of dilatometry-shaped samples in axial, radial and tangential orientation respectively. The pole figures display typical textures of fcc metals deformed by simple shear [56]. The 2θ angle measurements of the dilatometry-shaped samples at various annealing stages (see figure 4.26) indicate that deformation by ECAP leads to a stronger texture than deformation by HPT. This manifests in a strong orientation dependence of the intensity ratio of the (311) and the (222) reflection which is measured along, but not shown here.

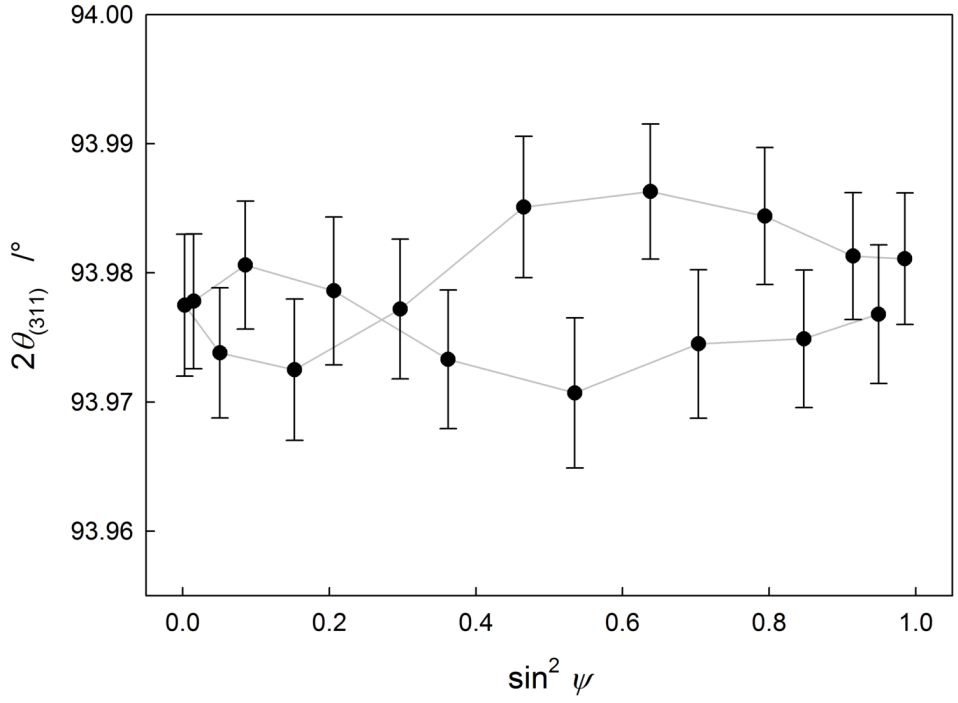
94.00
93.99
93.98
93.97
93.96
$2\theta_{(311)}$ /°
0.0
0.2
0.4
0.6
0.8
1.0
$\sin^2 \psi$

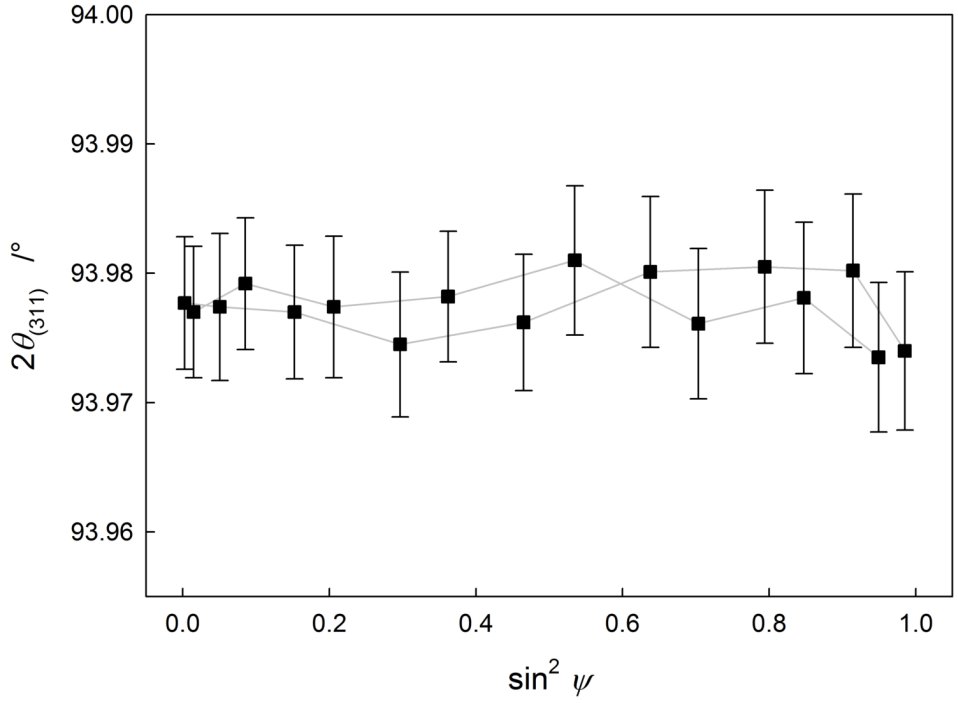
94.00
93.99
93.98
93.97
93.96
$2\theta_{(311)}$ /°
0.0
0.2
0.4
0.6
0.8
1.0
$\sin^2 \psi$

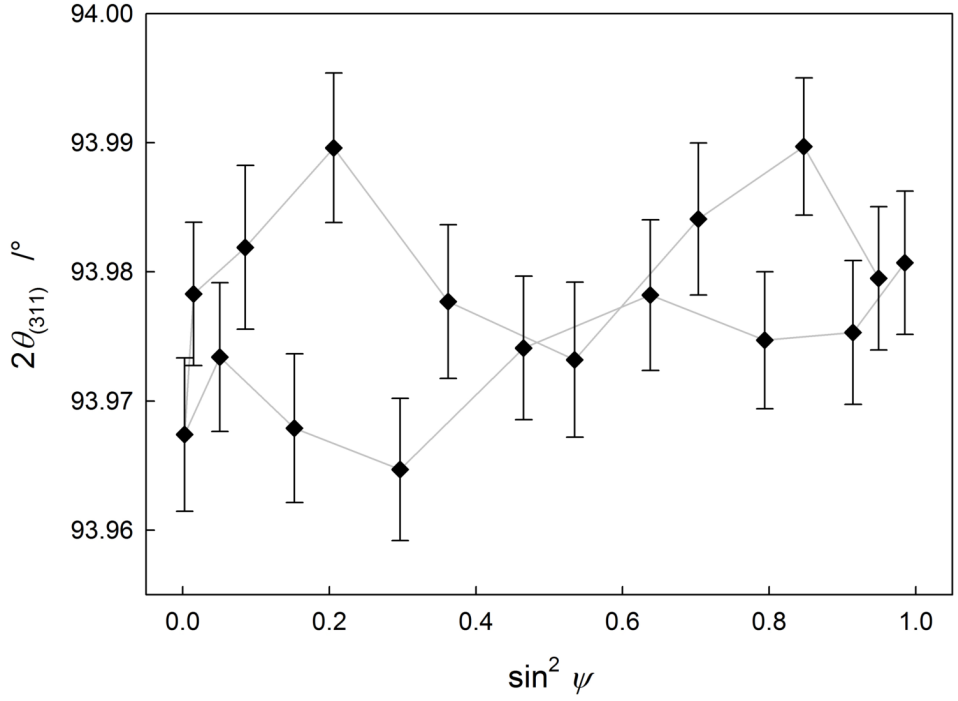

Figure 4.28: Measurement of the peak position 2θ of the (311) reflection in relation to $\sin^2\psi$ (the rotation around the ψ- or z-axis). Measurement in axial (top left), radial (bottom left) and tangential (right) orientations.

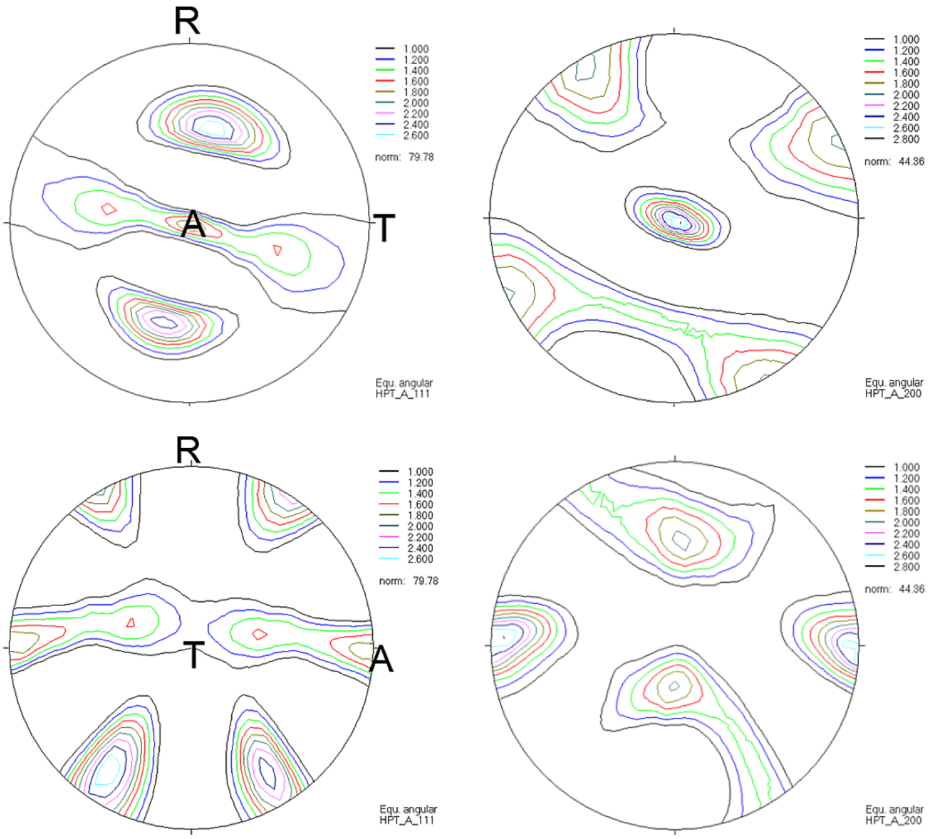

Figure 4.29: Pole figures derived from the texture measurements of dilatometry-shaped samples in axial (A), radial (R) and tangential (T) orientations. The top images show the texture in the R-T plane while the bottom images show the A-R plane. The left side images show the results derived from the (111) reflection while the right side images show the results from the (200) reflection.

4.4 Modeling of the annealing behavior of ultrafine-grained nickel

In order to better understand the processes involved in the annealing of defects in nickel, a quantitative model of the annealing behavior was prepared by C. Neubauer [57]. In this model all three annealing steps are considered with one or more defect annealing processes. The list of processes considered is given in table 4.11.

Table 4.11: Overview of the model developed by Neubauer: list of the individual processes considered for each stage of the annealing.

Stage A	Stage B	Stage C
Vacancies annealing at grain boundaries (spherical crystallites)	Recrystallization I	Void shrinkage (bulk diffusion)
Vacancies annealing at grain boundaries (cylindrical crystallites)		Void shrinkage (pipe diffusion)
Vacancies annealing at dislocations		Recrystallization II

For stage A it is assumed that the length change is caused entirely by the annealing of vacancies at different types of sinks. In the first case the grain boundaries act as sinks with the crystallites presumed spherical. As seen in the previous subsection though, the crystallites are elongated after process-

ing by HPT. Therefore, the second case considers the grain boundaries of cylindrical crystallites as the sinks. The third case uses dislocations as sinks for the annealing of vacancies.

According to Crank's *The Mathematics of Diffusion* [58] the transport of material (e.g. vacancies) by diffusion in a sphere is given by:

$$\frac{M_t}{M_\infty} = 1 - \frac{6}{\pi^2} \sum_{n=1}^{\infty} \frac{1}{n^2} \exp\left(\frac{-Dn^2\pi^2 t}{a^2}\right) \tag{4.1}$$

where M_t denotes the amount of material diffused in (or out) at the time t and M_∞ the amount of material diffused after infinite time. Furthermore, D is the temperature-dependent diffusion coefficient and a is the radius of the sphere. From equation 4.1 the volume change can be easily calculated by:

$$\frac{\Delta V}{V_0} = 1 - \frac{M_t}{M_\infty} \tag{4.2}$$

For the second case of diffusion in a cylinder of infinite height which is a fitting representation of diffusion in cylindrical crystallites the material transport is calculated by [57]:

$$\frac{M_t}{M_\infty} = 1 - \sum_{n=1}^{\infty} \frac{4}{a^2\alpha_n^2} \exp\left(-D\alpha_n^2 t\right) \tag{4.3}$$

where a denotes the radius of the cylinder in this case and α_n the zero points of the Bessel function of the first kind and zeroth order [57]:

$$J_0(a\alpha_n) = 0 \tag{4.4}$$

where a denotes again the radius of the cylinder. The volume change is determined like in the case of spherical crystallites from equation 4.2.

In both cases of vacancy annealing at grain boundaries a crystallite size distribution has to be assumed. For this work a simple Gaussian distribution was chosen and vacancy annealing functions for eleven crystallite sizes were calculated. The final function was determined by summing over all annealing functions multiplied by a weighting factor. The weighting factor is determined by the crystallite volume.

The annealing of vacancies at dislocations is based on the work of Seidman and Balluffi [59]. It describes the diffusion of vacancies to dislocations through a hollow cylinder with an outer radius b (the average half distance between two dislocations) and an inner radius c (the radius of the dislocation core). With the additional constraint that vacancies within the outer radius can only diffuse towards the dislocation core, the volume change can then be calculated by:

$$\frac{\Delta V}{V_0} = \sum_{n=1}^{\infty} \frac{2\pi\, C_0 \exp\left(-D\alpha_n^2 t\right)}{\alpha_n^2 \times N(\alpha_n)} \Big\{ Y_0(c\alpha_n) \left[bJ_1(b\alpha_n) - cJ_1(c\alpha_n) \right] - \\ - J_0(c\alpha_n) \left[bJ_1(b\alpha_n) - cJ_1(c\alpha_n) \right] \Big\} \tag{4.5}$$

where the denominator $N(\alpha_n)$ is a function of the radii b and c as well as of the Bessel functions of the first – $J_0(b\alpha_n)$, $J_0(c\alpha_n)$, $J_1(b\alpha_n)$, $J_1(c\alpha_n)$ – and of the second – $Y_0(b\alpha_n)$, $Y_0(c\alpha_n)$, $Y_1(b\alpha_n)$, $Y_1(c\alpha_n)$ – kind [57].

All three cases of vacancy annealing describe an isothermal process with a constant diffusion coefficient D. In order to apply the model on the results

from the dilatometry measurements, the temperature-dependent diffusion coefficient has to be used:

$$D(T) = D_0 \exp\left(-\frac{Q}{k_B\, T(t)}\right) \tag{4.6}$$

where D_0 denotes the diffusion constant, Q the activation energy of vacancy diffusion and k_B the Boltzmann constant. However, the equations 4.1, 4.3 and 4.5 were derived for a constant diffusion coefficient. Using $D(T)$ from equation 4.6 for the mentioned equations is therefore an approximation.

In figure 4.30 a comparison of the three vacancy annealing processes modeled in stage A for a heating rate of $3.0\,\mathrm{K\,min^{-1}}$ is shown. The volume change is normalized, and the average crystallite size is given as $a = 100\,\mathrm{nm}$. The diffusion parameters are a diffusion constant $D_0 = 3.4{\times}10^{-5}\,\mathrm{m^2\,s^{-1}}$ and an activation energy $Q = 1.15\,\mathrm{eV}$. The distance between dislocations equals to $b = 22.4\,\mathrm{nm}$ (which equals a dislocation density of $5.0{\times}10^{14}\,\mathrm{m\,m^{-3}}$) and the core diameter is assumed as $c = 0.3\,\mathrm{nm}$ [59].

The model shows that vacancy annealing at grain boundaries leads to comparable volume respectively length changes. Unsurprisingly, the annealing occurs at lower temperatures for spherical crystallites since in this case diffusion can take place in all spatial directions. The diffusion path is shorter for annealing at dislocations than for annealing at grain boundaries. Therefore, the temperature window for this process is smaller.

For the recrystallization in stage B the Johnson-Mehl-Avrami-Kolmogorov (JMAK) analysis [60, 61, 62] modified by Henderson [63] was applied. This JMAK-analysis has been proven feasible for the description of the recrystallization by Oberdorfer [17]. This calculation was improved by Neubauer

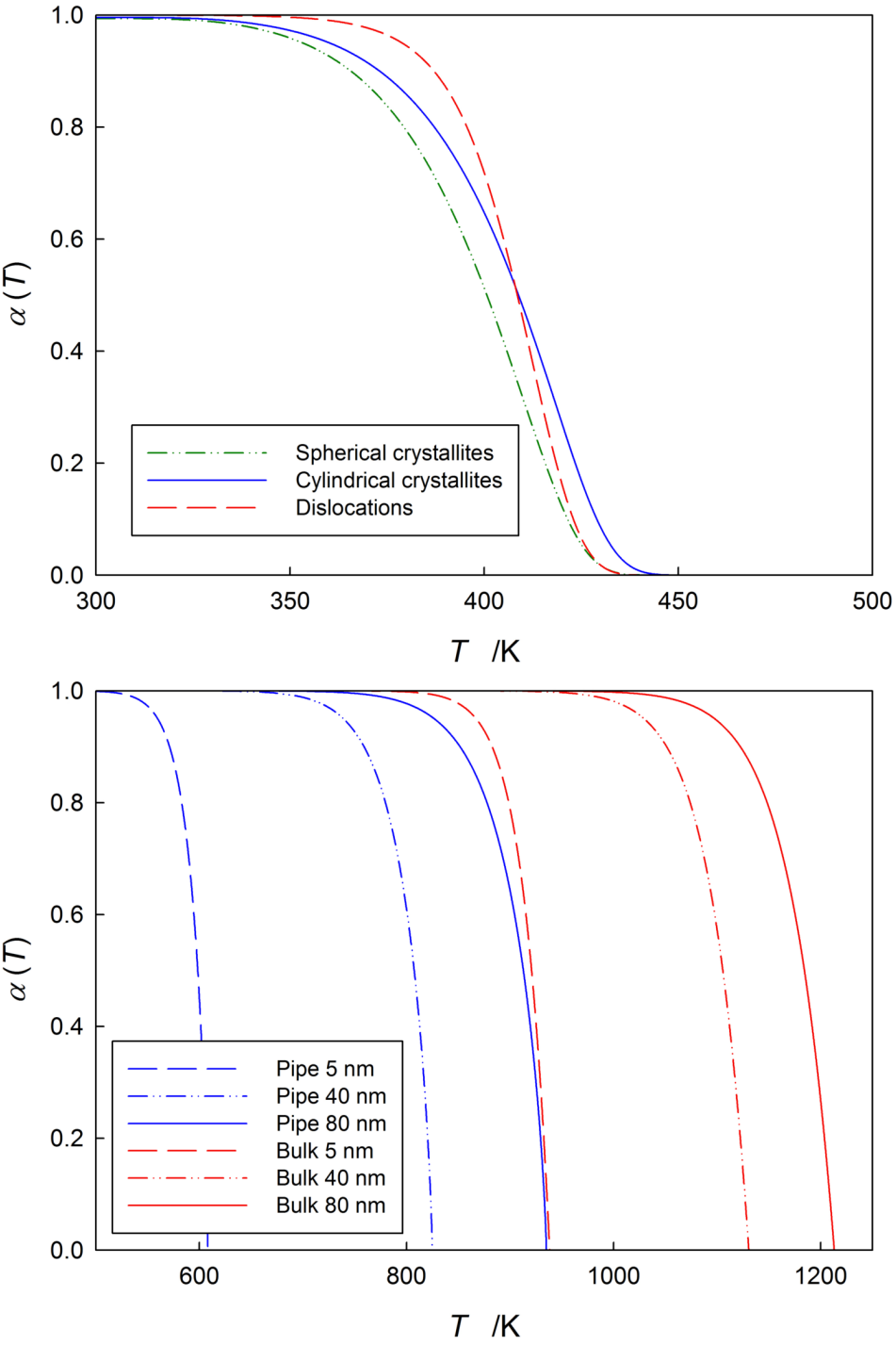

Figure 4.30: Various processes considered for stages A and C of the annealing model. For stage A (top) vacancy annealing at different sinks was modeled. For stage C (bottom) void shrinkage by bulk and pipe diffusion and different void sizes was modeled.

with the exponential integral function Ei which leads to the volume change being [57]:

$$\frac{\Delta V}{V_0} = \exp\left\{-\frac{K_0\,Q}{k_B\,\phi}\left[-Ei(x) + \frac{\exp(-x)}{x}\right]\right\}^n \tag{4.7}$$

with:

$$x = \frac{Q}{k_B\,T(t)} \tag{4.8}$$

where K_0 denotes the rate constant, ϕ the heating rate and n the Avrami exponent.

For stage C the volume change is attributed to the annealing of microvoids [17, 64, 14]. At elevated temperatures void shrinkage occurs due to vacancies being released from the voids and annealing at grain boundaries. The diffusion process can occur via the crystallites (bulk diffusion) or via dislocations cutting the voids (pipe diffusion). The model for void shrinkage is based on the work of Bowden and Balluffi [65]. The driving force behind void shrinkage is the difference of the chemical potentials between the curved surface of the void and the comparably flat surface of the crystallite. This driving force causes a steady diffusion of vacancies away from the void which in turns continually shrinks. For non-isothermal measurements the temperature-dependent diffusion coefficient has to be taken into account. Therefore, the volume change caused by the void shrinkage is then given by [57]:

$$\frac{\Delta V}{V_0} = 1 - \frac{1}{V_0}\left\{N_0\,\frac{4\pi}{3}\,r_0^3\left[1 - \left(\frac{r(t)}{r_0}\right)^3\right]\right\} \tag{4.9}$$

with the time-dependent void radius:

$$r(t) = \sqrt[3]{-3\,\frac{2\Omega\,\gamma}{\xi\,k_B}\,D_0\,\frac{-Ei\left(\frac{Q}{k_B T_0}\right) + Ei\left(\frac{Q}{k_B T_0 + k_B \phi t}\right)}{\phi} + r_0^3} \tag{4.10}$$

where N_0 denotes the number and r_0 the initial radius of the voids. Like for the crystallite size, a Gaussian distribution is assumed for the initial void radius and a weighted average over all radii is calculated. Furthermore, Ω is the atomic volume, γ is the surface energy and ξ is the correlation factor (0.781 for fcc metals).

For the case of diffusion along dislocations it is assumed that a dislocation connects the void to the grain boundary, and acts as fast diffusion path. The volume change is calculated by equation 4.9, however with the time-dependent void radius being:

$$r(t) = \sqrt[4]{-4\,\frac{A\,\Omega\,\gamma}{\pi\,L\,k_B}\,D_0\,\frac{-Ei\left(\frac{Q}{k_B T_0}\right) + Ei\left(\frac{Q}{k_B T_0 + k_B \phi t}\right)}{\phi} + r_0^4} \tag{4.11}$$

where A is the cross section and L is the length of the dislocation. Since diffusion occurs via a dislocation, different values for the activation energy Q and the diffusion constant D_0 have to be used. Data from the work of Wuttig and Birnbaum [66] was chosen for the model.

A comparison of the two void shrinkage mechanics for three initial void sizes each can be found in figure 4.30. As expected from the lower activation energy for diffusion along dislocations [67, 66], void shrinkage via pipe diffusion occurs at much lower temperatures than void shrinkage via bulk diffusion.

Both types of void shrinkage show a similar dependence on the initial void size where a larger initial void size leads to a shift to higher temperatures.

For the final model all three stages had to be combined. This is done by fitting the calculated volume changes for each stage to a normalized dilatometry curve. The relative amount of the volume changes during each stage is determined from the measured curve and introduced to the model by a weighting factor. For stage A annealing of vacancies at grain boundaries of cylindrical crystallites is chosen. For stage B a recrystallization step has already been developed by Oberdorfer [17], and for stage C a combination of void shrinkage by pipe diffusion and another recrystallization step is chosen.

Figure 4.31 shows the least-squares fit of the model to a measured, normalized dilatometry curve. Overall, the model was applied to the curves resulting from the nine measurements 00E to 016, as well as two curves resulting from measurements performed by Steyskal [21]. For most curves the fit results in good agreement with the measurement results, however in some cases the agreement is poor. The most plausible explanation for this poor agreement in some cases is that the weighting factors for the final results were taken from a single measurement (013) and applied to all other fits.

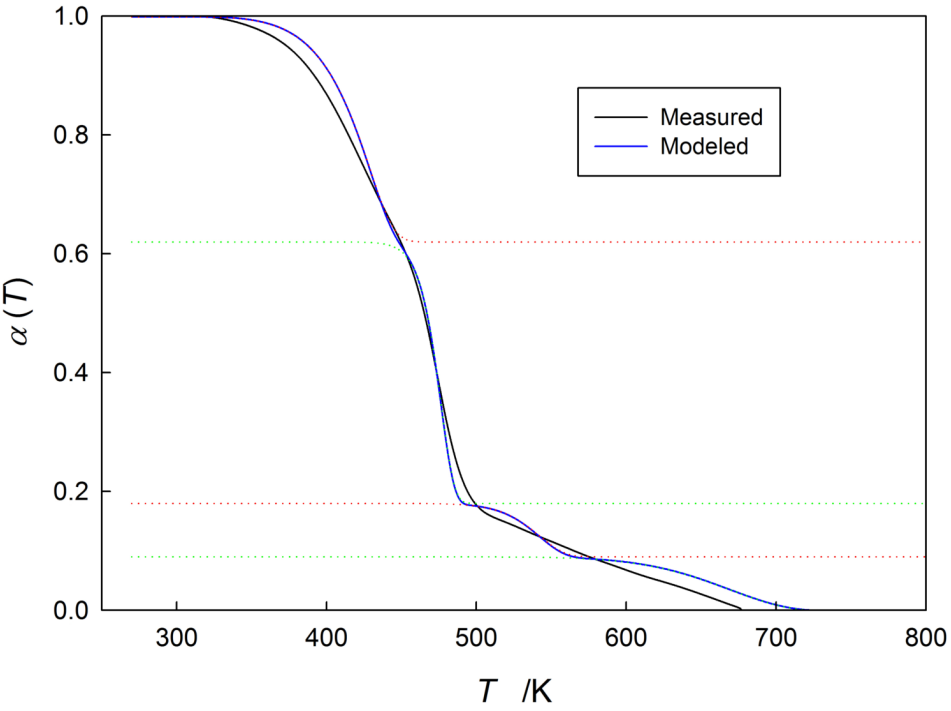

Figure 4.31: Combined least-squares fit of the individual models for all three stages to a measured curve. The processes included are vacancy annealing at grain boundaries of cylindrical crystallites (stage A); recrystallization (stage B); void shrinkage by pipe diffusion and further recrystallization (stage C). The dotted curves represent the individual processes.

5

Discussion

The primary goals of this thesis were twofold: first to investigate the influence of the method of plastic deformation on the annealing behavior of high-purity, ultrafine-grained nickel, second to shed light into the anisotropy of the annealing behavior which has first been observed by Oberdorfer [17] and by Steyskal [21] as well as in the author's master thesis [22]. However, whereas the aforementioned studies were restricted to small sets of samples, systematic studies on a large number of samples were conducted for this thesis.

The choice for ultrafine-grained nickel as example material was based on it's good workability and a well-defined, multi-stage annealing behavior. This annealing behavior with well-separated recovery and recrystallization processes was put to good use in the determination of critical material parameters: the excess volume of grain boundaries which has been calculated from the length change during the recrystallization [16], and the activation energy of the recrystallization which has been derived from the shift of the recrystalliaztion temperature [25]. Furthermore, defect concentrations [15] have been measured for ultrafine-grained nickel and other materials.

The methods that were applied in order to generate these results so far were deformation by HPT, high-precision difference dilatometry and electron microscopy [17]. In this study these complementary methods were augmented by the methods of deformation by ECAP, elastic tensile deformation, plastic deformation by cold rolling, neutron diffraction, SQUID magnetometry and modeling of the complete annealing behavior. With the help of these methods a model could be developed which is able to elucidate the nature of the anisotropy of the annealing behavior of ultrafine-grained nickel.

In the following chapter each of the three stages – A, B and C – will be discussed separately (in sections 5.1, 5.2 and 5.3) and important findings of the systematic studies are presented. Special emphasis has been put on stage A (section 5.1) which showed a highly anisotropic annealing behavior during initial measurements [21]. This effect was attributed to either annealing of anisotropic residual stress or anisotropic annealing of vacancies in combination with an outward expansion of the relaxed lattice (figure 5.1) [17].

Figure 5.2 shows a comparison of the annealing behavior observed during difference dilatometry measurements of samples in axial, radial and tangential samples. Table 5.1 lists the average length changes measured during the three annealing stages depending on the sample orientation. A complete list of the length changes of each measurement comprising these averages is included in the appendix.

The results from this work firstly show that the observed anisotropic annealing behavior is well reproducible for a large numbers samples. Secondly, for samples cut from HPT specimen the quality of the measurement (most prominently for stage A) appears to depend on the distance between sample and torsion axis. Furthermore, deformation by ECAP leads to a similar annealing behavior as HPT with an anisotropic length increase during stage A too.

Table 5.1: Average length changes during the three annealing stages A, B and C for samples from different measurement series and orientations (Or.). No. indicates the number of samples measured in this orientation. The orientations are A (axial), R (radial), T (tangential) after deformation by HPT (see also figure 3.6), and E (extrusion), N (normal), V (transverse) after deformation by ECAP (see also figure 3.7).

Series	Or.	No.	$\frac{\Delta L}{L_0}\Big\vert_A$ /10^{-4}	$\frac{\Delta L}{L_0}\Big\vert_B$ /10^{-4}	$\frac{\Delta L}{L_0}\Big\vert_C$ /10^{-4}
HPT					
Ni5TT	A	27	-1.39±0.59	-2.28±0.32	-1.22±0.60
	T	8	+0.38±0.19	-1.29±0.28	-1.00±0.43
Ni5Tan	A	4	-2.44±0.70	-2.93±0.48	-1.56±0.52
	T	20	+0.89±0.33	-1.32±0.43	-1.34±0.54
Ni10Ten	A	3	-1.11±0.34	-1.95±0.33	-1.57±0.16
	T	3	-0.15±0.37	-1.03±0.24	-0.90±0.11
Ni16Tan	A	3	-2.78±0.08	-2.41±0.95	-2.55±0.14
	T	24	+0.38±0.95	-0.80±0.38	-2.44±1.08
Ni16CR	T	10	+0.33±0.87	-0.71±0.36	-2.03±0.44
Ni5BB	T	12	+0.63±0.48	-1.26±0.42	-2.23±0.76
ECAP					
Ni4BC	E	4	+0.26±0.49	-0.42±0.18	-1.38±0.79
	N	6	-0.11±0.47	-1.01±0.54	-1.92±1.10
	V	3	-0.69±0.34	-2.14±0.70	-1.48±0.56
Ni12A	E	4	+0.37±0.22	-0.59±0.10	-0.36±0.08
	N	4	-1.53±1.00	-1.76±0.21	-0.48±0.18
	V	5	-1.65±0.20	-1.55±0.37	-0.47±0.09
Ni12BC	E	5	+0.30±0.39	-0.88±0.20	-0.42±0.16
	N	5	-1.39±0.45	-1.60±0.40	-0.39±0.20
	V	5	-1.21±0.22	-1.54±0.52	-0.42±0.29

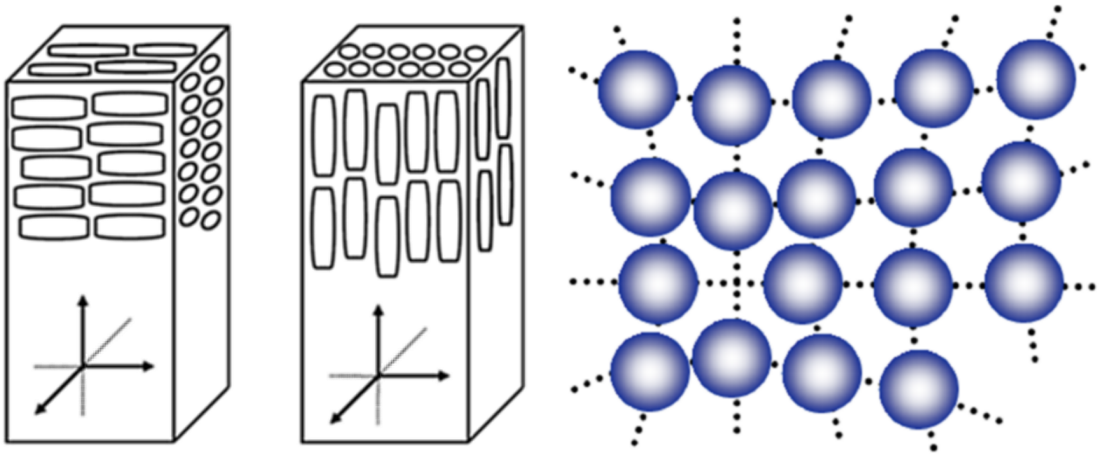

(a) Crystallite elongation relative to sample orientation.

(b) Isotropic relaxation of the lattice at a vacancy.

Figure 5.1: An anisotropic annealing of vacancies can explain the anisotropic length changes (see section 5.1.8). (a) Vacancies anneal preferably perpendicular to the crystallite elongation resulting from deformation by HPT and ECAP; a length decrease occurs in those directions. (b) A relaxed vacancy being occupied by a lattice atom leads to an isotropic expansion of the lattice by an amount equal to the relaxation volume.

5.1 Stage A – Recovery

Primary focus of this work was put on this annealing stage and the influence of deformation and measurement parameters on the annealing behavior as well as the anisotropy observed in this stage. From electron microscopy it becomes clear that the crystallite size does not change during stage A [22]. Therefore, the length change during that stage is attributed to the annealing of vacancies [68]. The annealing of dislocations should not contribute significantly to the length change in this stage. The dislocation density found after HPT is about $\rho_{MD} = 6{\times}10^{15}\,\mathrm{m}^{-2}$ [69] which according to Oberdorfer [17] only contributes up to 12 % to the overall volume change.

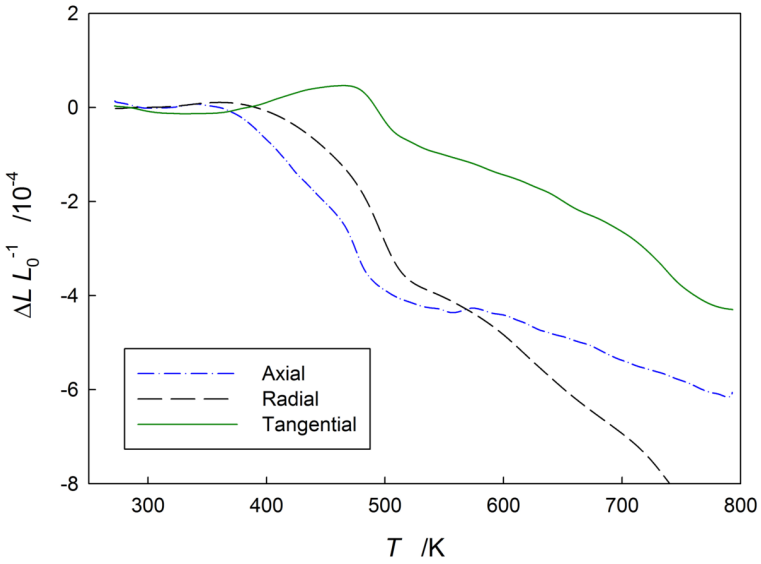

Figure 5.2: Exemplary difference dilatometry curves of samples in axial (sample 0CA from specimen Ni5Mod), radial (sample 0D2 from specimen Ni5Mod) and tangential (sample 0D5 from specimen Ni5Mod) orientations. The sample in tangential orientation shows an irreversible length increase during stage A.

The lower length change measured after deformation by ECAP compared to deformation by HPT reflects in the neutron measurements. The peak broadening results show a higher FWHM after deformation by HPT: 0.70° after deformation by HPT compared to 0.66° after deformation by ECAP. Additionally, the decrease of the FWHM is significantly larger after deformation by HPT too. However, the FWHM at the end of stage A is almost identical with 0.65° after deformation by HPT in comparison to 0.64° after deformation by ECAP. This is a strong sign that the defect concentration after deformation by HPT is considerably higher than after deformation by ECAP, and that the majority of point defects have annealed out at the end of stage A.

Complementary SQUID measurements were performed both on samples in the as-prepared state, after annealing to 370 K (beginning of stage A) as

well as after annealing to 430 K (end of stage A). Furthermore, the measurements were performed on nickel deformed by HPT as well as by ECAP using samples of different orientations. However, it turned out that the recovery processes taking place during stage A did not have an effect on the magnetization behavior. This comes not surprising since the high-field measurements showed that voids have the most influence on the magnetization behavior (see section 5.5).

After deformation by HPT stage A covers the temperature range from about 340 to 435 K ($\varphi = 3.0\,\mathrm{K\,min^{-1}}$), shifted slightly depending on the heating rate. Meanwhile after deformation by ECAP stage A covers the temperature range from 370 to 500 K ($\varphi = 3.0\,\mathrm{K\,min^{-1}}$), similarly shifted depending on the heating rate.

In the following an in-depth discussion of stage A will be given, including overviews on the orientation dependences after deformation by HPT (section 5.1.1) and by ECAP (section 5.1.4), discussions of the position (section 5.1.2) and heating rate dependence (section 5.1.3), as well as a comparison with the single dilatometry study not performed in our group (section 5.1.5). After consideration of issues of residual stress (section 5.1.6) and dislocations (section 5.1.7), the model of anisotropic annealing of vacancies is presented in the last section 5.1.8.

5.1.1 Overview of the orientation dependence after HPT

The orientation dependence of the annealing behavior during stage A was first observed in ultrafine-grained nickel [21] and later in ultrafine-grained iron too [70]. In this thesis extensive measurements on the orientation dependence have been performed with a significant sample size for the first time.

The measurement series Ni5Tan (deformation by HPT, five turns) as well as Ni16Tan (deformation by HPT, 16 turns) each included 24 samples in tangential orientation in which the anisotropic length increase is observed. A total of six samples in tangential orientation were measured in the measurement series Ni10NTen (deformation by HPT, ten turns) and Ni10Ten (deformation by HPT, ten turns, subsequent tensile straining) combined. The measurement series Ni16CR (deformation by HPT, 16 turns, subsequent cold rolling) and Ni5BB (deformation by HPT, five turns, bar-shaped bases) consisted of ten respectively twelve samples in tangential orientation. Additionally, eight samples in tangential orientation were measured during the diploma thesis of the author (Ni5TT, deformation by HPT, five turns, under liquid nitrogen cooling).

As seen in table 5.1 with the exception of the series Ni10Ten (which includes Ni10NTen as well) all of these series show an average length increase during stage A. The results for these series are displayed in figure 4.6 and in the appendix. It becomes evident that even though the overall length change during stage A is negative in these measurements still an irreversible length increase can be observed. As a result the difference curve has a plateau-like character at the end of stage A as seen in the top image of figure 4.6.

As can be ssen in table 5.1 for the series Ni5TT, Ni5Tan, Ni10Ten and Ni5BB the errors of the average length changes for samples in tangential orientation are lower or of the same dimension as for samples in axial orientation. The average length changes, however, vary between -0.15×10^{-4} and $+0.89\times10^{-4}$. For the series Ni16Tan and Ni16CR, on the other hand, the errors for samples in tangential samples are very large.

One potential source of error is the fact that a number of the samples included in the analysis were not cut in perfect tangential orientation but slightly tilted towards radial orientation. Four samples from the measure-

ment series Ni5TT, all six samples from the measurement series Ni10Ten and Ni10NTen, and four samples from the measurement series Ni5Tan were not in ideal tangential orientation. Concluding from the results of the series Ni10Ten and Ni10NTen this deviation from ideal tangential orientation does affect the length change during stage A. This effect becomes even more evident when all samples from the disc specimen Ni5Tan are compared (displayed in the appendix).

5.1.2 Position dependence

From equation 3.1 one can see that the applied strain during deformation by HPT depends on the radius r. Therefore, the total applied strain in a disc specimen processed by HPT increases from the center to the edge. However, during deformation by HPT a steady-state is reached at strains of about $\varepsilon = 8$ to 16 [30]. According to equation 3.1 the strain in a disc specimen is radius dependent. Therefore, the steady-state is reached faster at the edges of the disc than in the center. All dilatometry sample measured in this study exhibited a strain of at least $\varepsilon = 12$. Thus, it is safe to assume that all samples were cut from a steady-state microstructure.

Figure 4.2 shows three samples from the edge of the disc specimen Ni5Tan (deformation by HPT, five turns) with an applied strain of 40 (cut from the edge of the disc specimen, see figure 4.1). All samples from this disc specimen were deformed to the steady-state, but there is a clear difference between samples deformed to a strain of 40 and samples deformed to a strain of 20 (cut from closer to the center of the disc specimen, see figure 4.1, the results can be found in the appendix). If only samples deformed to a strain of 40 are considered the amplitude in stage A equals to $(+0.92 \pm 0.27) \times 10^{-4}$. Whereas, the amplitude equals to $(+0.86 \pm 0.44) \times 10^{-4}$ when only samples of

a strain of 20 or less are considered (excluding samples of partially radial character). The average irreversible length increases are comparable, but the error increases when only samples from the center of the disc specimen are taken into consideration.

For the disc specimen Ni16Tan (deformation by HPT, 16 turns) the samples from the edge (applied strain of 100, see figure 4.8) show a large spread as well. If only those samples are considered, the average irreversible length increase equals to $(+0.46 \pm 1.07) \times 10^{-4}$. The four samples from the center of the disc (the figure can be found in the appendix) which were deformed to a strain of 35 show an average length increase of $(+0.16 \pm 1.00) \times 10^{-4}$. In both cases the error and therefore the spread of the amplitudes is much larger than in the disc specimen Ni5Tan.

However, in the case of the disc specimen Ni16Tan an influence of the heating rate has to be considered as well (covered in the next section). Accordingly, if the samples from the edge of disc specimen Ni16Tan (deformed to a strain of 100) are grouped by heating rate, then the average of each group's error equals to 0.39×10^{-4} instead of 1.07×10^{-4}. Taking into account that each group of results consists of only two or three values and that outliers can thus have a great impact on the error of a group, we can assume that the spread of the amplitudes is lowest at the edge of a disc specimen.

This effect appears to be a result of the sample position and not of the applied strain at the sample's positions. Samples from the disc specimen Ni16Tan at a distance of about 6 mm had similar strain applied as samples from the edge of the disc specimen Ni5Tan (35 and 40). The latter show a very small spread of the amplitudes while the former do show a much larger spread. The heating rate in samples from the edge of the disc specimen Ni5Tan does not have the same influence on the amplitude as in samples from the edge of the disc specimen Ni16Tan.

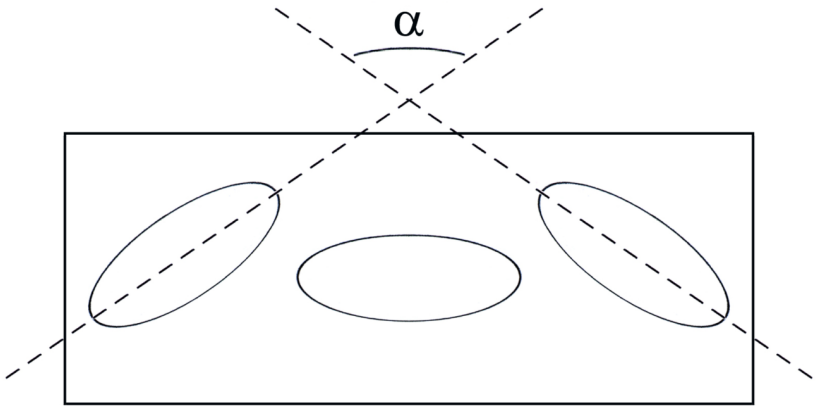

Figure 5.3: The elongated crystallites at the bases of a dilatometry sample in tangential orientation are not exactly parallel to the measurement direction. The angle α between the elongation direction at the top and at the bottom base of the sample depends on the distance to the torsion axis.

Table 5.2: Angle between the direction of crystallite elongation at opposing ends of a 7 mm long dilatometry sample depending on sample position (see above figure 5.3). The exemplary equivalent strain ε applies for samples deformed under the conditions from the measurement series Ni5TT, Ni5Tan and Ni5BB.

d /mm	ε	α
2.25	12	62°
6.00	20	120°
9.75	30	140°
13.50	40	151°

A possible explanation for this position dependence might be that samples from close to the torsion axis in a disc specimen deviate from ideal tangential orientation in parts of the sample volume. Assuming a sample length of 7 mm and a distance of 6 mm between the center of the dilatometry sample and the torsion axis, the shear direction at the top and the bottom base of the sample are at an angle of 120°. Since the crystallite elongation occurs along the shear direction the angle between crystallites at the top and the bottom base are hence 120° too as can be seen in figure 5.3. Table 5.2 shows the influence of sample position on the angle between crystallite elongation at opposing ends of a dilatometry sample.

Unlike in deformation by HPT deformation by ECAP leads to a uniform strain along the cross section of the rod specimen. Additionally, the direction of crystallite elongation is parallel along the cross section as well as the length of the rod specimen (disregarding the end sections). Furthermore, the strain applied on the rod specimen Ni12A (deformation by ECAP, twelve passes, route A) and Ni12BC (deformation by ECAP, twelve passes, route B_C) is only about 7.5 (see equation 3.2) which is barely enough to reach the steady-state and well below the strains applied on any disc specimen.

However, looking at figures 4.18a and 4.18b it becomes obvious that all samples in transverse and normal orientation are equidistant to the core of the rod specimen. Only samples in extrusion orientation were cut out at distances of 5.94 mm (e.g. sample 0DB from the specimen Ni12A), of 6.78 mm (e.g. sample 0F5 from the specimen Ni12BC) and of 7.96 mm (e.g. sample 0DC from the specimen Ni12A) from the core of the rod specimen. This distance seems to have no influence on the annealing behavior of the samples though.

From the Ni12A rod specimen one sample behaves like an outlier (sample 0DB which is not considered for further calculations, results found in the ap-

pendix) and it is cut at a distance of 5.94 mm from the core. The remaining samples (in extrusion orienation) behave very similar to each other and similar to samples in tangential orienation after deformation by HPT. From the Ni12BC rod specimen two samples behave different than the rest (samples 0FA and 0FB) in that they show an overall length decrease during stage A despite an obvious length increase in that stage as well (results found in the appendix). These two samples were cut at distances of 5.94 mm and 6.78 mm from the core. The other three samples in extrusion orientation were cut at distances of 5.94 mm and 7.96 mm from the core.

With no position dependence being observed after deformation by ECAP the explanation in terms of crystallite angles within a dilatometry sample becomes even more plausible. Generally, it can be stated that the lower strain applied during deformation by ECAP does not result in a significantly lower reproducibility compared to deformation by ECAP. Once the steady-state is reached during deformation (at a strain of about 8) applying further strain does not increase the reproducibility of the annealing behavior.

5.1.3 Heating rate dependence of the amplitude

In the above section it was mentioned that samples from the edge of the disc specimen of the measurement series Ni16Tan (deformation by HPT, 16 turns, see section 4.1.3) show a large spread of the amplitude during stage A (see figure 4.8). However, the results of the measurement series Ni5Tan (deformation by HPT, five turns) show a very small spread for samples from the edge of the disc specimen. Furthermore, if the results from the measurement series Ni16Tan and Ni16CR (deformation by HPT, 16 turns, subsequent cold rolling) are grouped by heating rate the spread becomes very small. This clearly indicates that for the measurement series Ni16Tan

and Ni16CR the amplitude during stage A indeed depends on the heating rate. Other measurement series, on the other hand, do not show such a heating rate dependence.

Figure 5.4 shows the length change during stage A in dependence of the heating rate for samples in tangential orientation from the measurement series Ni16Tan and Ni16CR. Included are the results for three samples measured at heating rates between 3.00 K min^{-1} and 5.00 K min^{-1} (3.75, 4.00 and 4.50 K min^{-1}). Another sample measured at 10.00 K min^{-1} heating rate is not included (the result can be found in the appendix). This diagram shows a step-like heating rate dependence of the annealing behavior of samples in tangential orientation.

At heating rates in the range of 1.50 to 4.50 K min^{-1} the annealing behavior of samples in tangential orientation is similar to the annealing behavior observed in the measurement series Ni5Tan (section 4.1.1) with a marked length increase. The average length change for samples measured at heating rates of 4.50 K min^{-1} and lower is calculated with $(+0.69\pm0.41)\times10^{-4}$ which is still below the average length change from the measurement series Ni5Tan. Whereas, the annealing behavior observed at heating rates from 5.00 K min^{-1} upwards is plateau-like. The average length change determined for these samples is $(-0.56\pm0.54)\times10^{-4}$.

This heating rate dependence of the amplitude during stage A was observed in the measurement series Ni16Tan and Ni16CR which were subjected to 16 turns of HPT. In all other measurement series in which the deformation was kept to five (Ni5Tan and Ni5BB) or ten turns (Ni10Ten) instead, no such heating rate dependence was observed. Deformation by ECAP did not result in such a heating rate dependent behavior either. Therefore, the most obvious explanation is the higher strain applied during the deformation compared to other measurement series.

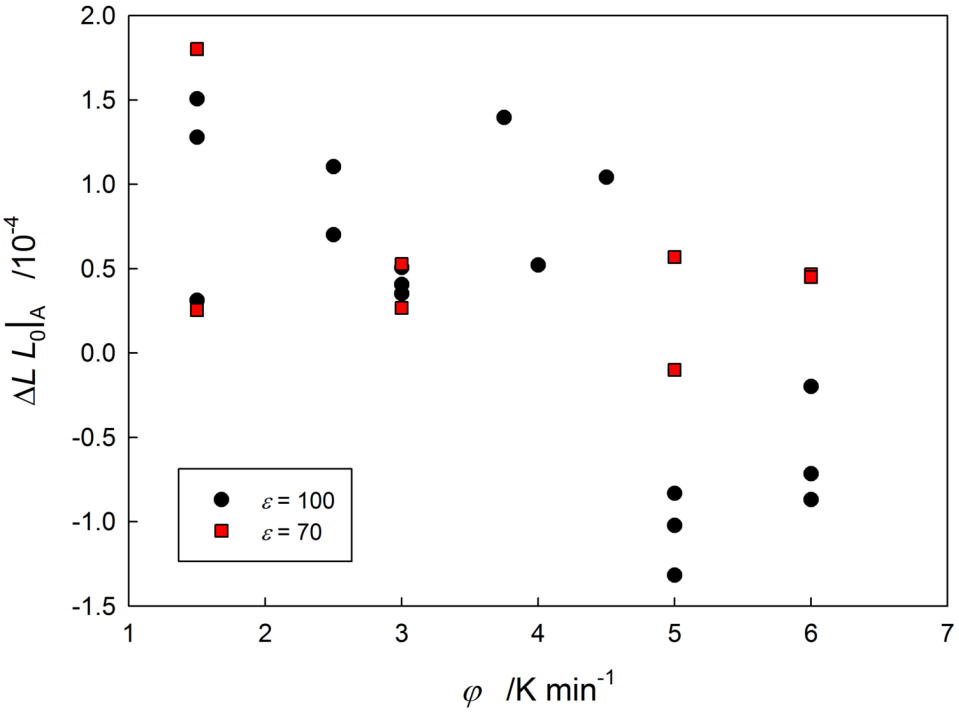

Figure 5.4: Length changes during stage A in relation to heating rate for samples from the measurement series Ni16Tan (deformation by HPT, 16 turns) and Ni16CR (deformation by HPT, 16 turns, subsequent cold rolling) deformed to equivalent strains of $\varepsilon = 100$ and of $\varepsilon = 70$. Between heating rates of $\varphi = 4.5\,\mathrm{K\,min^{-1}}$ and of $\varphi = 5.0\,\mathrm{K\,min^{-1}}$ the annealing characteristics change fundamentally.

5.1.4 Orientation dependence after ECAP

In this work further difference dilatometry measurements after deformation by ECAP were performed on high-purity nickel (see section 4.2). From the first measurement series Ni4BC (deformation by ECAP, four passes, route B_C) it became clear that nickel deformed by ECAP shows a similar three-stage behavior as nickel deformed by HPT (see section 4.2.1). Furthermore, just like after deformation by HPT an anisotropic annealing behavior during stage A was observed. As seen in table 5.1 an irreversible length increase was measured in extrusion orientation, a length decrease in transverse orientation, and in normal orientation both small length increases as well as small length decreases were measured (see figure 4.16).

Table 5.1 shows two important findings: first, the average length changes were in general smaller than after deformation by HPT; second, the variance of the length changes is still about the same extent as for measurements after deformation by HPT. The high variance could be the result of the small sample number of only 13 samples in total. However, when the microstructure of the samples is taken into account (see figure 4.17) it becomes likely that the applied strain of 3.5 is not enough to reach the steady-state and to achieve a fully homogeneous microstructure.

In order to achieve a fully homogeneous microstructure the measurement series Ni12A (deformation by ECAP, twelve passes, route A) and Ni12BC (deformation by ECAP, twelve passes, route B_C) were prepared by increasing the number of passes to twelve and the applied strain to 7.5 (see section 4.2.2). The increased strain greatly improved the reproducibility and the distinction between the different orientations. The annealing behavior after twelve passes of ECAP very closely resembles the annealing behavior after deformation by HPT except for a shift to higher temperatures (see figure

4.19). The anisotropic annealing behavior during stage A is now clearly developed as well.

In total 15 samples were measured from each of the rod specimen Ni12A and Ni12BC respectively. The measurement series Ni12A resulted in two outliers (plus another potential outlier which was still considered for the calculations listed in table 5.1), while the measurement series Ni12BC did not produce any outliers. The measured length changes were smaller in general than for nickel deformed by HPT with the length changes after deformation by ECAP with route B_C being smaller than with route A. The errors were relatively small with the exception of stage A in normal orientation of the measurement series Ni12A which is caused by the single outlier mentioned above.

Comparing the orientation dependent annealing behavior of nickel deformed by HPT and ECAP, the principal orientations can be put in two groups. The first group of axial, radial (HPT), normal and transverse (ECAP) orientations show length decreases during stage A; the second group of tangential (HPT) and extrusion (ECAP) orientations show length increases. This anisotropic behavior of nickel is well reflected in the microstructure. Nickel deformed by HPT or ECAP shows strongly elongated crystallites after deformation where the elongation coincides well with the length increase (in tangential and extrusion orientation respectively).

5.1.5 Comparison with results by Klement on ultrafine-grained copper processed with ECAP

An anisotropic annealing behavior was first observed by Klement [27] in pure copper (99.99 %) deformed by ECAP. The deformations were performed by

route A with 2, 4, 5, 6, 10 and 12 passes. Dilatometry was used to measure the change of excess volume in different orientations, and TEM and DSC were used to identify the annealing processes.

The dilatometry measurements revealed two annealing stages: one stage between 370 to 440 K and a second stage between 440 to 480 K. During the first stage no change in the microstructure and no heat release in the DSC measurements was observed. The second stage results in a change from an ultrafine-grained to a coarse-grained microstructure and is characterized by an exothermal peak in the DSC measurements.

The second stage was identified primarily as recrystallization process. The observed length changes showed strong anisotropy with the greatest length decrease in normal and the smallest length decrease in transverse orientations. This anisotropy was partially explained by the platelet-like microstructure with the highest number of grain boundaries in normal orientation. However, the annealing of grain boundaries did not explain the different length decreases in extrusion and normal orientations.

This discrepancy was explained by the annealing of vacancies at dislocations and the resulting dislocation climb. If the half-plane forming the dislocations is reduced by dislocation climb, the crystal will shrink parallel to the Burgers vector [27]. Since ECAP deformation takes place by simple shear [39], the author assumed that most dislocations are aligned with their Burgers vector parallel to shear plane and shear direction. This model refined with texture data was able to explain the anisotropic length changes during the second stage.

The first stage up to a temperature of 440 K also showed an anisotropic annealing behavior. During this stage a length increase was observed in normal orientation for samples cut from rod specimen deformed by route

A for 2 to 6 passes, and in transverse orientation for samples cut from rod specimen deformed for 6 to 12 passes. Remaining samples in normal and transverse orientation as well as samples in extrusion orientation showed either a length decrease or no length change at all.

The sum of length changes in all three orientations lead to an overall volume change of roughly zero for all rod specimen from 2 to 12 passes. Since neither TEM nor DSC showed signs of defect annealing it was concluded that the length changes during this stage were the result of a thermally activated Bauschinger effect [28] which partially undoes the plastic deformation of the ECAP process. This Bauschinger effect would be driven by residual stresses and facilitated by defect rearrangements.

A thermally activated Bauschinger effect can explain the irreversible length increase in normal orientation and the irreversible length decrease in extrusion orientation. However, it does not explain the irreversible length increase in transverse orientation unless the deformation process is more complex than assumed. Furthermore, the Bauschinger effect does not explain why the irreversible length increase becomes smaller in normal orientation and larger in transverse orientation with more passes.

Interestingly, this anisotropic annealing behavior of copper deformed by ECAP is inverse to the annealing behavior of nickel deformed by ECAP or HPT (see sections 5.1.4 and 5.1.1). Meanwhile, high-purity copper deformed by HPT [17, 26] showed a different annealing behavior than the results from Klement [27] as well. After deformation by HPT a three-stage behavior is observed for copper similar to nickel deformed by HPT.

Similar to high-purity nickel, stage A was determined to be a recovery process and stage B to be a recrystallization stage. Unlike high-purity nickel, though, neither of those stages showed any anisotropic annealing behavior.

However, according to Klement [27] copper deformed by ECAP showed a platelet-like microstructure. Whereas, after deformation by HPT equiaxed crystallites were reported Oberdorfer [26]. Thus, it is not entirely clear whether copper deformed by HPT with a platelet-shaped or elongated crystallites would show the same inverse anisotropic behavior as copper deformed by ECAP.

5.1.6 Residual stress

Both Klement [27] as well as Oberdorfer [17] have theorized that the anisotropic length increase is not caused by the annealing of defects but by plastic deformation driven by residual stress. Considering the large applied strains during deformation by HPT or ECAP it is no surprise that residual stresses are introduced during these processes [71]. However, in preparation of the dilatometry samples the dimensions of the bulk are reduced by about one order of magnitude, and it has to be assumed that any residual stresses are either strongly reduced or eliminated entirely thereby.

The intention of the measurement series Ni10Ten (deformation by HPT, ten turns, subsequent tensile straining) was to remove any residual stress from the material by applying a uniaxial elastic strain to the material after deformation by HPT. If the sum of residual and externally applied stress exceeds the yield strength of the material, plastic flow sets in and removes the residual stress [50]. Removal of residual stress by elastic deformation necessitates the material to behave both elastic and perfectly plastic. However, since nickel deformed by HPT shows strain hardening, only a reduction of the residual stresses can be expected.

For the measurement series Ni16Tan and Ni16CR (deformation by HPT, 16 turns) the full disc specimen Ni16CR was plastically deformed by cold-

rolling after deformation by HPT. It can be assumed that the additional plastic deformation (to a strain of about 0.22) removes any residual stress from the deformation by HPT. Unlike the samples cut from the uniaxially strained disc specimen Ni10Ten, samples cut from the cold rolled disc specimen Ni16CR (and also from the disc specimen Ni16Tan) were cut in ideal axial, radial or tangential orientation.

The results on the tensile strained and the cold rolled samples are shown in the figures 4.6 and 4.8 respectively, along with reference measurements each. The results from the measurement series Ni10Ten and Ni10NTen seem to indicate a difference between samples which were post-processed compared to samples which were not. In elastically deformed samples (Ni10Ten) a plateau-like behavior is observed. The two samples not elastically post-processed show a different behavior: one shows a similar behavior as samples which were elastically deformed, the other shows a pronounced length increase. However, this spread can be attributed to the samples measured during both these series not being cut in ideal tangential orientation.

The results from the measurement series Ni16Tan and Ni16CR show the heating rate dependence discussed in section 5.1.3. However, no difference can be observed when comparing the cold-rolled and not cold-rolled samples. The average length changes during stage A are $(+0.38 \pm 0.95) \times 10^{-4}$ for the measurement series Ni16Tan and $(+0.33 \pm 0.87) \times 10^{-4}$ for the measurement series Ni16CR. Furthermore, the observed heating-rate dependence is identical between both measurement series with high heating rates leading to reduced length increases.

The elastic deformation did not remove the irreversible length increase in tangential orientation and it did not distinctly reduce it either. Additionally, the plastic deformation by cold-rolling did neither remove nor reduce the irreversible length increase during stage A. These results indicate that there

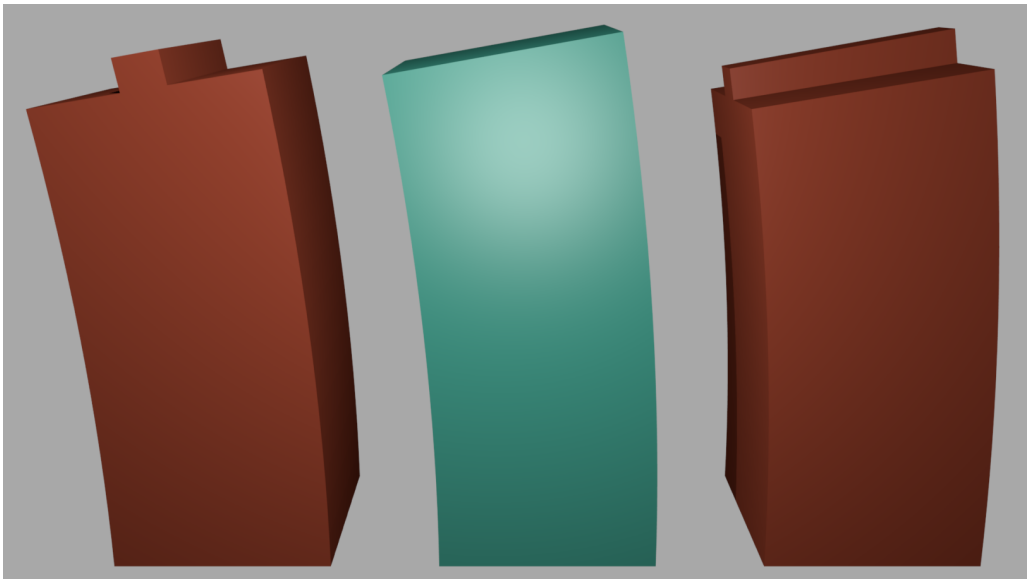

Figure 5.5: Exemplary distortion of samples with planar (green, center) and non-planar (red, left and right) bases due to a residual stress gradient. Due to the orientation of the bar the right and center samples show a larger length increase than the left sample.

are no residual stresses in dilatometry samples which could lead to a plastic deformation during the measurement.

The measurement series Ni5BB (see section 4.1.4) was performed in order to measure a potential plastic deformation caused by residual stress directly. If a residual stress gradient exists in dilatometry samples, then samples in tangential orientation with non-planar bases (as seen in figure 4.13) must show a different length increase whether the bar is parallel to axial or radial orientation. Figure 5.5 shows a schematic view of the principle of this measurement series.

The results of the difference dilatometry measurements of samples in tangential orientation with non-planar base (measurement series Ni5BB) are well comparable to the results from the measurement series Ni5TT and Ni5Tan. The average length increase in series Ni5BB is with $(+0.63 \pm 0.48) \times 10^{-4}$ be-

tween the average length increases of the measurement series Ni5TT (with $(+0.38\pm0.19)\times10^{-4}$) and Ni5Tan (with $(+0.90\pm0.33)\times10^{-4}$). The errors are largest in the measurement series Ni5BB which is probably caused by the unusual sample geometry. Due to the plane push-rod acting on the non-planar base the probability of lateral forces occurring during the measurement increase compared to regular measurements.

The measurement series Ni5BB consisted of samples with three geometries: two samples with regular plane bases, and five samples each with non-planar bases with the bar parallel to the axial, respectively, the radial direction (see figure 5.5). The two samples with plane bases show an average length increase of $(+0.50\pm0.02)\times10^{-4}$ during stage A. The five samples with non-planar bases and the bar parallel to axial direction show an average length increase of $(+0.69\pm0.45)\times10^{-4}$.The five samples with non-planar bases and the bar parallel to radial direction show an average length increase of $(+0.62\pm0.64)\times10^{-4}$.

The low error of samples with regular planar bases compared to samples with non-planar bases indicates that the sample geometry is most likely the cause for the large overall error in the measurement series Ni5BB. The average length changes of samples with bar-shaped bases are almost identical independent of the orientation of the bar. At best, the average length change of samples with bar-shaped bases is slightly larger compared to samples with planar bases. However, this is the case independent of the orientation of the bar, and thus it cannot be caused by residual stress, but most likely by lateral forces due to the sample geometry instead.

All difference dilatometry measurements conducted in order to confirm if the length increase during stage A is caused by residual stresses, did not show hints at such residual stresses. In addition to the measurements described above neutron diffraction measurements were performed to directly identify

residual stresses (see section 4.3). Preliminary measurements by XRD were performed by Keckes for the thesis of Oberdorfer [17] without any signs of residual stresses having been found.

Unlike XRD neutron diffraction allows measurement of residual stresses beyond the surface area. Therefore, scans of the residual stresses in a disc specimen processed by HPT were performed (see figure 4.25). From these results it can be assumed that the center of the disc specimen and at the edges are stress-free. Furthermore, the scans indicate that parts of the disc specimen are compressed in axial orientation and under tensile stress in tangential orientation.

During deformation by HPT under quasi-constrained conditions which is the case in currently used HPT setups [72] the disc specimen is compressed axially and constrained in radial direction. Limited plastic flow occurs in radial direction until the cavities of the anvils are filled. Therefore, compressive stress in axial direction and tensile stress in radial and tangential direction can be expected with the stress-free edges acting as constraint for the residual stresses. However, no tensile stress is observed in radial direction.

Whereas, the residual stress measurements of the bulk disc specimen yielded quite clear results, measurements of dilatometry samples cut from another disc specimen deformed similarly to the bulk one delivered inconclusive results. As seen in figure 4.26 no orientation dependence can be observed at any annealing stage. The large spread after annealing to 770 K is easily explained by the drastically increased crystallite size after annealing. Due to the large crystallite size the number of diffracting crystallites is very small and slightly tilted crystallites may lead to a shift of the signal.

Dilatometry samples cut from the rod specimen Ni12BC deformed by ECAP seemingly show orientation dependence (see figure 4.26). However, said orientation dependence persists after annealing to 500 K at which recovery has

finished. After annealing to 570 K and recrystallization having taken place, a change of the orientation dependence occurs. At this point it can be concluded that a simple measurement of the 2θ shift is senstive enough to map the macroscopic stress distribution within a bulk specimen. However, in order to determine macroscopic stresses in a dilatometry-shaped sample cut from such a bulk specimen, the more sensitive $\sin^2\psi$ method was applied in this study (see figure 4.28).

The $\sin^2\psi$ measurement is the standard method to determine macroscopic stresses in a material. None of the samples showed a slope (figure 4.28) and therefore it can be concluded that no residual stresses of first or second order are present in dilatometry samples. The only exception to this being residual shear stresses close to the surface (non-zero ε_{13} or ε_{23} components) which are indicated by the ψ-splitting in samples in axial and tangential orientation. These shear stresses are usually the result of machining, localized at the surfaces and are of no relevance for dilatometry measurements.

Residual stresses of third order (microscopic stresses) cannot be detected by the 2θ shift (neither using the $\sin^2\psi$ method) [73]. However, the peak broadening observed during the aforementioned measurements clearly shows the existence of stresses of third order in dilatometry samples (see figure 4.27). After deformation by HPT the peak broadening decreases by about 0.05° after annealing to 450 K. On the other hand after deformation by ECAP the reduction of the peak broadening only amounts to about 0.02° after annealing to 500 K. Since residual stresses of third order are localized at defects, these results confirm difference dilatometry measurements which found smaller defect concentrations after deformation by ECAP than by HPT.

In summary, elastic post-deformation, plastic post-deformation, difference dilatometry measurements with samples having non-planar bases and neu-

tron diffraction measurements were performed during this work. None of theses measurements as well as XRD measurements performed before show any hints at macroscopic residual stresses in dilatometry samples. Only residual stresses in bulk disc specimen deformed by HPT and residual stresses of third order localized at defects were detected. Therefore, it can be safely assumed that the irreversible length increase during stage A observed in samples of tangential respectively extrusion orientation is not caused by residual stresses.

5.1.7 Annealing of dislocations

When Klement [27] and co-workers observed an irreversible length increase in copper deformed by ECAP, they attributed this length change to a thermally activated Bauschinger effect (see section 5.1.5). The results of high-purity nickel deformed by ECAP presented in this work, however, cannot be explained by a Bauschinger effect. Furthermore, during recrystallization Klement observed an anisotropic length change too which could not be satisfactorily explained by platelet-shaped crystallites. This additional anisotropy was explained by vacancies annealing at dislocations leading to a length decrease parallel to the preferred Burgers vector.

The Orowan relation is commonly used to describe the relation between strain ε and dislocation density on a slip system α [74]:

$$\dot{\varepsilon}^{\,\alpha} = \rho_m^{\alpha}\, b\, \overline{v}^{\,\alpha} \tag{5.1}$$

with $\dot{\varepsilon}$ being the strain rate, ρ_m being the density of mobile dislocations, b being the modulus of the Burgers vector and $\overline{v}$ being the average dislocation

velocity. Since both HPT and ECAP can be considered to apply plastic deformation by simple shear [39], a preferred Burgers vector parallel to the shear direction has to be expected after both types of deformation.

According to Klement the annealing of vacancies at dislocations leads to dislocation climb which results in a length decrease in the direction of the preferred Burgers vector. However, the highest vacancy concentration determined during this work – 13.38×10^{-4} (see section 4.2.2) – is about one order of magnitude too small to facilitate the climb of an edge dislocation by a single lattice plane. Therefore, the contribution of vacancy annealing at dislocations to the overall length change is questionable.

Despite annealing by dislocation climb very likely not contributing significantly to the length change observed in stage A, annihilation and rearrangement of dislocations might do. Equation 3.5 describes the length change of a dislocation core of a dislocation annealing. Using dislocation density data from XRD measurements [69, 64] the length change caused by annealing dislocations has been estimated by Oberdorfer [17]. For iron, nickel and copper this length change has been calculated to be not more than -0.65×10^{-4} each.

While the overall contribution of such a length change is almost negligible, its contribution to the length change during stage A is not. However, since the volume of the dislocation core only disappears in case of dislocation annihilation and not in case of the formation of dislocation dipoles or low-angle grain boundaries. Therefore, in-depth information on the distribution of dislocations annealing by annihilation respectively formation of dislocation structures would be necessary in order to determine the impact of dislocation annealing on the length change during stage A.

Equation 3.5 only considers the volume of the dislocation core and not the residual stress of third order locally distorting the lattice around the core. This residual stress is the result of non-linear effects and can be calculated using either thermodynamic calculations [75] or second-order elasticity theory [76, 77]. In an isotropic medium the volume change of the material containing dislocations is given by [77]:

$$\Delta V = -\frac{1}{K}\left[\left(1+\frac{1}{K}\frac{\partial K}{\partial V}\right)\int W_D \,\mathrm{d}V_0 + \left(1+\frac{1}{G}\frac{\partial G}{\partial V}\right)\int W_S \,\mathrm{d}V_0\right] \tag{5.2}$$

where K is the bulk modulus of the medium, W_D is the average dilatation work done on the volume, G is the shear modulus of the medium and W_S is the average shearing work done on the volume.

The sign of the volume change ΔV in equation 5.2 depends on the signs of the terms $\int W_D \,\mathrm{d}V_0$ and $\int W_S \,\mathrm{d}V_0$. Without knowledge of these terms and without knowledge of whether the volume change is strictly isotropic (which is questionable considering the strong anisotropy of a simple shear deformation) it is not feasible to incorporate equation 5.2 in the analysis of stage A. It is generally assumed though that the volume change caused by dislocations is positive [75, 76].

5.1.8 Annealing of vacancies

Residual stresses introduced during the deformation by HPT respectively by ECAP can be ruled out as cause of the irreversible length increase during the recovery stage of ultrafine-grained nickel (as described in section 5.1.6). An alternative explanation was first proposed by Oberdorfer [17] and Steyskal [21], and then worked out in detail by the author [68]. This explanation

suggests that the irreversible length increase is caused by a combination of preferential vacancy annealing at grain boundaries and lattice expansion upon annealing of vacancies.

As seen in sections 4.1.1, 4.1.3 and 4.2.2 deformation by HPT and by ECAP leads to a crystallite elongation in high-purity nickel (see also [30, 78, 79, 80, 81]). Without external or internal forces (such as residual stresses) the diffusion of vacancies can be considered to happen randomly and therefore uniformly. However, since vacancies within the crystallites are statistically closer to the long sides of the crystallites, they are more likely to anneal at that sides of the crystallites. Therefore, it can be assumed that vacancy diffusion and annealing occurs primarily perpendicular to the crystallite elongation (see figure 5.1).

For the difference dilatometry measurements this means that the volume change due to vacancy annealing occurs only perpendicular to the crystallite elongation: in axial and radial directions after deformation by HPT, and in normal and transverse directions after deformation by ECAP (see figures 4.2 and 4.19). The excess volume of vacancies, however, is less than the atomic volume Ω due to lattice relaxation around vacancies. This is expressed in equation 3.4 by the negative (vacancies being replaced by atoms) and the positive (lattice expansion) term.

Since the lattice expansion is uniform the volume increase caused by it can be measured in all directions (see figure 5.1). In axial and radial directions (after deformation by HPT), and in normal and transverse directions (after deformation by ECAP) the sum of vacancies being replaced by atoms and lattice expansion results in a net length decrease. In tangential direction (after deformation by HPT), and in extrusion direction (after deformation by ECAP) only the length increase due to lattice expansion is measured.

Therefore, the length change for samples in axial, radial, normal and transverse directions equation 3.4 changes to:

$$\left.\frac{\Delta L}{L_0}\right|_{\text{Vacancies}} = \frac{1}{3}C_V r - \frac{1}{2}C_V \tag{5.3}$$

where the factor $1/3$ denotes the isotropic lattice expansion in all three spatial dimensions and $1/2$ the anisotropic diffusion of the vacancies in two dimensions only.

While for samples in tangential and extrusion directions the negative term drops out and the length change is expressed as:

$$\left.\frac{\Delta L}{L_0}\right|_{\text{Vacancies}} = \frac{1}{3}C_V r \tag{5.4}$$

together equation 3.4 can be used to determine the lattice relaxation factor r from the length decrease respectively length increase measured in two directions [17, 68]:

$$r = \frac{3M}{2M - 2} \tag{5.5}$$

where M is the ratio of length increase (in the direction parallel to the cyrstallite elongation) to length decrease (in the direction perpendicular to the crystallite elongation). Equation 5.5 was applied on dilatometry data from 18 samples in axial orientation deformed by HPT (13 samples from [22], one sample from [21] and four samples from measurement series Ni5Tan– see table 4.2) as well as 24 samples in tangential orientation (three samples

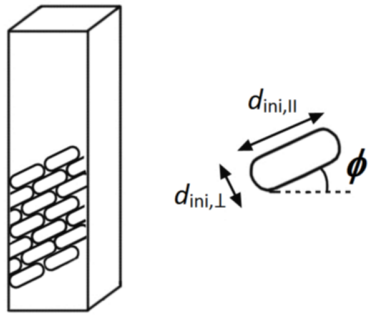

Figure 5.6: Orientation of the elongated crystallites within a dilatometry sample. The angle ϕ is defined as the angle between the direction of the crystallite elongation to the plane normal of the measurement direction.

from [22], one sample from [21] and 20 samples from measurement series Ni5Tan–see table 4.2). From this data a relaxation factor r for high-purity nickel deformed by HPT between 0.36 to 0.40 was determined [68]. With:

$$V_V = (1 - r)\ \Omega \tag{5.6}$$

this relaxation factor results in a vacancy volume between $0.60\,\Omega$ and $0.64\,\Omega$.

In case of nickel deformed by HPT the crystallites are elongated at an angle with respect to the tangential direction [30, 82, 17]. Oberdorfer found this angle to be 10° [17]. This angle is small enough to assume that the elongation is parallel to tangential direction, and perpendicular to axial and radial directions. In case of nickel deformed by ECAP the crystallite elongation occurs at angles of 23° (rod specimen Ni12A) and 33° (rod specimen Ni12BC) with respect to extrusion orientation (see section 4.2.2). These angles imply a strong deviation from parallel or perpendicular crystallite orientation with respect to measuring direction. Therefore, equation 3.4 has to adapted with the angle of the elongation direction in mind.

Since the elongation of the crystallites is neither exactly parallel nor exactly perpendicular to the measurement direction (for any sample orientation) both equation 5.3 and equation 5.4 apply for every sample to a degree depending on the angle ϕ. This leads to the universal equation:

$$\left.\frac{\Delta L}{L_0}\right|_{\text{Vacancies}} = \cos\phi\left(\frac{1}{3}C_V r - \frac{1}{2}C_V\right) + \sin\phi\,\frac{1}{3}C_V r \tag{5.7}$$

which is simplified to:

$$\left.\frac{\Delta L}{L_0}\right|_{\text{Vacancies}} = \frac{1}{3}\left(\cos\phi + \sin\phi\right)C_V r - \frac{1}{2}\cos\phi\, C_V \tag{5.8}$$

A summary of the calculated results for nickel after deformation by HPT or ECAP based on equation 5.8 can be found in table 5.3. Table 5.3 also contains the corresponding vacancy volumes $V_V = (1 - r)\ \Omega$. For the results from measurement series Ni5Tan (deformation by HPT, five turns) with a small tilt angle of $\phi = 10°$ a relaxation factor of $r = 0.51$ and for the vacancy concentration a value of $C_V = (8.24 \pm 0.29) \times 10^{-4}$ are obtained. Compared to earlier results by Oberdorfer [17] an only slightly higher vacancy concentration is calculated. The relaxation factor of 0.51, however, is higher than that reported by Oberdorfer (0.27 to 0.30) [17].

Equation 5.8 is particularly relevant for nickel deformed by ECAP due to a substantial tilt of the direction of the crystallite elongation. For the calculations with measurement series Ni12A (deformation by ECAP, twelve passes, route A, $\phi = 23°$) and Ni12BC (deformation by ECAP, twelve passes, route B_C, $\phi = 33°$) the length changes in normal and extrusion orientation are compared. Using equation 5.8 relaxation factors of $r = 0.56$ for the

Table 5.3: Results for the relaxation factor r, the vacancy volume V_V and the vacancy concentration C_V. Analysis of the results for stage A of annealing for the measurement series Ni5Tan (deformation by HPT, five turns), Ni12A (deformation by ECAP, twelve turns, route A) and Ni12BC (deformation by ECAP, twelve turns, route B_C). The tilt angle ϕ describes the angle between the crystallite elongation and measurement direction (see 5.6).

Series	ϕ	r	V_V /Ω	C_V /10^{-4}
Ni5Tan	10°	0.51	0.49	8.24±0.29
Ni12A	23°	0.56	0.44	7.18±0.20
Ni12BC	33°	0.68	0.32	13.38±0.56

Ni12A series and $r = 0.68$ for the Ni12BC series are calculated. The vacancy concentrations equal $C_V = (7.18\pm0.20)\times10^{-4}$ for the Ni12A series and $C_V = (13.38\pm0.56)\times10^{-4}$ for the Ni12BC series. The results for the Ni12A series are very close to the results from the Ni5Tan series which applied deformation by HPT (section 4.1.1), but for the Ni12BC series both the relaxation factor and the vacancy concentration are significantly higher.

We start the discussion of the present results on vacancy volume with a comparison with the preliminary results reported by Oberdorfer [17]. As stated above, Oberdorfer found lower values of the vacancy relaxation, i.e. higher values of the vacancy volume for nickel deformed by HPT. However, this difference would get substantially reduced if the tilt angle of 10° is taken into account. Indeed, without considering the tilt angle vacancy volumes of 0.60 Ω or 0.64 Ω are derived from the present data on nickel deformed by HPT under almost identical conditions. Therefore, the higher vacancy volume reported earlier by Oberdorfer might arise from neglecting the tilt angle ϕ.

Presumably the most reliable theoretical values currently available are those recently reported by Metsue et al [83]. For the temperature range between

300 K and 400 K of the present measurements, vacancy relaxation factors of 0.33 or 0.36 (corresponding to vacancy volumes of 0.67 Ω or 0.64 Ω) were obtained by local density approximation or generalized gradient approximation respectively. The present experimental relaxation factor for nickel deformed by HPT (taking the tilt angle into account) is slightly larger. From earlier numerical simulations [84, 85, 86] lower values of the relaxation factor were found for nickel as indicated in table 5.4. A lower value of 0.22 was also found earlier for nickel a temperature of 6 K using diffusive x-ray scattering [87]. Table 5.4 also shows numerically calculated results for the vacancy volumes of other metals. As can be seen for molybdenum, tantalum and tungsten, as well as for niobium and vanadium albeit to a smaller degree, the results can depend strongly on the calculation method.

The almost equal vacancy volumes deduced for nickel prepared by ECAP (using route A) compared to nickel prepared by HPT supports the assumption that independent of the deformation process vacancy annealing is the predominant recovery process occurring in stage A. The lower vacancy volume of nickel processed by ECAP with route B_C is probably the result of the larger scattering compared to route A. The lower average aspect ratio of the crystallites resulting from route B_C in combination with a larger variance of the aspect ratio might contribute to this scattering.

The notion of vacancy annealing as the dominating process during stage A explains the slight shift of this stage after deformation by ECAP compared to deformation by HPT too. It reflects the increasing diffusion length of the vacancies for reaching grain boundaries due to larger crystallites after deformation by ECAP. Both in nickel deformed by HPT as well as by ECAP high vacancy concentrations are observed which might be considered the characteristic consequence of severe plastic deformation of high-purity nickel.

Table 5.4: Literature data on numerically calculated vacancy volumes V_V for nickel and various fcc and bcc metals.

Element	V_V / Ω	Source
Ni	0.78	Bender and Ehrhart [87]
	0.84	Gao et al [84]
	0.83	de Debiaggi et al [85]
	0.83	Ortega et al [86]
	0.67	Metsue et al [83]
	0.64	Metsue et al
Al	0.67	Chetty et al [88]
Cr	0.97	Kurita and Numakura [89]
Fe	0.94	Kurita and Numakura
Ge	0.7	Scholz and Seeger [90]
Mo	0.6	Meyer and Fähnle [91]
	0.55	Söderlind et al [92]
	0.86	Kurita and Numakura
Nb	0.7	Söderlind et al
	0.64	Kurita and Numakura
Ta	0.53	Söderlind et al
	0.72	Kurita and Numakura
V	0.63	Söderlind et al
	0.70	Kurita and Numakura
W	0.45	Söderlind et al
	0.87	Kurita and Numakura

These results further validate the model developed by Neubauer [57] for stage A of the annealing of high-purity nickel deformed by HPT. For this model, stage A was considered to be caused by annealing of vacancies only. In particular three different mechanisms were developed: annealing of vacancies at grain boundaries with either spherical or cylindrical crystallites, or annealing of vacancies at dislocations. For the final model the annealing of vacancies at grain boundaries with cylindrical crystallites resulted in an excellent match to the measured results (see section 4.4).

In summary, the mechanism of vacancy annealing at grain boundaries is able to plausibly explain the anisotropy of the annealing behavior of high-purity nickel during stage A. The model taking into account the exact angle ϕ of the crystallite elongation yields well matching values for the vacancy volume after deformation by HPT or ECAP (route A). The model by Neubauer [57] (see section 4.4) already takes this mechanism into account, but without including the angle ϕ of the crystallite elongation yet.

5.2 Stage B – Recrystallization

Stage B which is comprised of recrystallization has already been extensively discussed by Steyskal [21] and Oberdorfer [17]. Electron microscopy imaging (using BSE and EBSD methods) has shown that stage B is encompassed by a significant change of the crystallite size and shape. Determination of the activation energy of the recrystallization [25] as well as the grain boundary excess volume [16] have delivered good results.

Neutron diffraction measurements (see section 4.3) show a change of the FWHM during stage B which directly correlates to the peak broadening caused by the initial crystallite size. Further reduction of the FWHM after

the end of stage B has been reached is significantly reduced in magnitude as well as in slope. It can be assumed that this further reduction of the FWHM is caused primarily by secondary grain growth or the annealing of persistent defects (e.g. voids). Therefore, the length change during stage B is fully attributed to the annealing of grain boundaries. This notion is also confirmed by supplementary studies of the magnetic saturation behavior by SQUID magnetometry (see section 5.5).

The recrystallization taking place during stage B covers the temperature range from about 435 to 500 K ($\varphi = 3.0\,\mathrm{K\,min^{-1}}$) after deformation by HPT. Deformation by ECAP leads to stage B covering the temperature range from 500 to 575 K ($\varphi = 3.0\,\mathrm{K\,min^{-1}}$). After both deformation methods a shift of the recrystallization depending on the heating rate is observed.

In the following the kinetics of stage B (section 5.2.1) and the issue of grain boundary excess volume will be discussed (section 5.2.2).

5.2.1 Activation energy of recrystallization

In this work the activation energies for multiple measurement series were calculated using Kissinger analyses [49]. A comparison of the Kissinger plots of the measurement series performed in this work is displayed in figure 5.7. Values for the activation energy found in the measurement series Ni5Tan, Ni12A and Ni12BC are listed in table 5.5. The measurement series Ni5Tan (deformation by HPT, five turns) yielded an activation energy of (1.04±0.08) eV while the measurement series Ni5BB (deformation by HPT, five turns, bar-shaped bases) yielded an activation energy of (1.17±0.11) eV. Deformation by ECAP using route A (measurement series Ni12A, twelve passes) resulted in an activation energy of (1.21±0.10) eV which matches

the results from nickel deformed by HPT remarkably well. Using route B_C (measurement series Ni12BC, twelve passes) resulted in an activation energy of (1.42±0.24) eV.

Figure 5.7 demonstrates that the activation energies determined during this work are all very similar. Furthermore, the results match previous results very well too (see below). The stronger deviation observed in the measurement series Ni12BC might be the result of the high variance of these measurements which manifests in a significantly larger error than in other measurement series. Figure 5.7 also shows the shift of the recrystallization temperatures between deformation by HPT and by ECAP, and for the latter between routes A and B_C. This shift correlates with the initial crystallite sizes observed in nickel deformed by HPT and by ECAP (as well as the routes A and B_C).

The activation energy for the recrystallization of high-purity nickel deformed by 16 turns of HPT (measurement series Ni16Tan) was determined with only (0.65±0.11) eV. This value is not only significantly lower than the activation energies of any other measurement series performed during this work, but also clearly lower than the literature value of 0.95 eV. The low error indicates that this significantly lower activation energy is not an outlier caused by a stronger deviation of the recrystallization temperatures.

Interestingly, compared to nickel deformed by five turns of HPT the recrystallization temperature of nickel deformed by 16 turns of HPT is shifted to higher temperatures (by 20 K and more). However, the strain applied during 16 turns of HPT is more than twice as high and therefore the recrystallization temperature is expected to be lower. This temperature shift in conjunction with the heating rate dependence observed during recovery (see section 5.1.3) indicates that nickel undergoes microstructural development even in the steady-state which probably also affects the Kissinger analysis. It is unclear, however, in how far these two phenomena are connected.

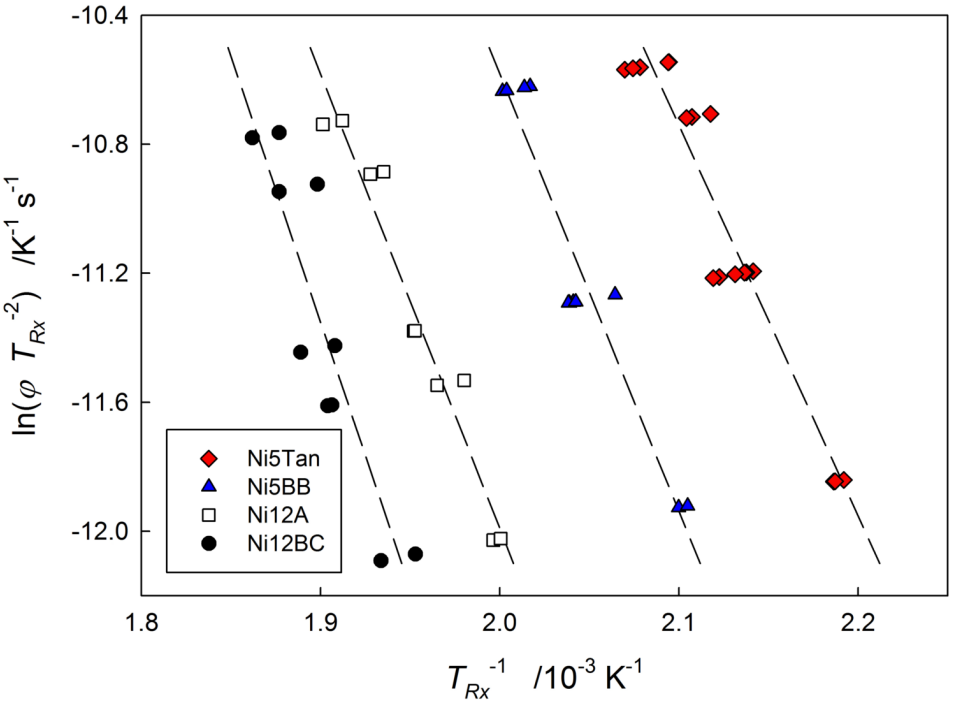

Figure 5.7: Kissinger analyses for the recrystallization stages of samples from measurement series Ni5Tan (deformation by HPT, five turns), Ni5BB (deformation by HPT, five turns, bar-shaped bases), Ni12A (deformation by ECAP, twelve passes, route A) and Ni12BC (deformation by ECAP, twelve passes, route B_C). For the measurement series Ni12A and Ni12BC samples in extrusion orientation were not included due to the large spread of the results. The recrystallization temperature T_{Rx} is defined as the local minimum of stage B in the derivative curves.

Former calculations performed by Oberdorfer [17] applied the Kissinger analysis and non-isothermal JMAK modeling [60, 61, 62, 63] respectively on nickel deformed by HPT. The Kissinger analysis yielded an activation energy of (1.20±0.04) eV while the non-isothermal JMAK analysis yielded an activation energy of (1.20±0.01) eV. These values are higher than the values of 0.95 eV determined from DSC measurements [93] and of 0.88 to 0.94 eV determined from TEM measurements [94].

A Kissinger analysis of the recrystallization stage of high-purity nickel deformed by HPT under liquid nitrogen cooling yielded an activation energy of (1.14±0.06) eV [22]. The difference dilatometry curves from those measurements were used to model the recrystallization with the non-isothermal JMAK kinetic (see section 4.4). For the model an activation energy of 1.15 eV was chosen [57]. Using this activation energy the measured dilatometry curves could be fitted very well.

Compared to these earlier results the numbers of samples used for the calculations have been greatly increased. Where previous analyses were performed with five samples [17], the calculations in this study are based on 50 samples in total: 18 samples from measurement series Ni5Tan, twelve samples from measurement series Ni5BB, and ten samples from measurement series Ni12A and Ni12BC each. Furthermore, this study also included samples in tangential orientation, as also nickel deformed by ECAP instead of HPT.

5.2.2 Grain boundary excess volume

The high density of grain boundaries in ultrafine-grained metals in combination with the clear separation of recovery and recrystallization in nickel (and copper) allows for the determination of the grain boundary excess vol-

ume (not to be confused with the grain boundary width) from the length change measured by difference dilatometry. In this study the grain boundary excess volume of ultrafine-grained nickel was determined after deformation by HPT as well as by ECAP for two different sample orientations each. The calculations are based on the work by Steyskal [16] and Oberdorfer [26] who applied equation 3.6 on results from nickel respectively copper deformed by HPT.

Equation 3.6 assumes that the grain boundaries contributing to the length change are positioned perpendicular to the measurement direction. This assumption is sufficiently fulfilled if the crystallites are elongated roughly perpendicular to the measurement direction (e.g. for samples in axial orientation) or parallel to the measurement direction (e.g. for samples in tangential orientation). For ultrafine-grained nickel prepared by HPT this is the case: the crystallites are elongated at an angle of 10° with respect to tangential direction [17]. Thus, for ultrafine-grained nickel deformed by HPT the requirement is met.

For ultrafine-grained nickel prepared by ECAP equation 3.6 cannot be applied, because the crystallites are elongated at angles of 23° and 33° with respect to extrusion direction (see section 4.2.2). At such angles it has to be assumed that both grain boundaries parallel as well as perpendicular to the direction of crystallite elongation contribute to the length change regardless of the sample orientation. The magnitude of the contribution as well as the crystallite size (which defines the distance between two grain boundaries) are both modified by the angle ϕ between the direction of crystallite elongation and the plane perpendicular to measurement direction (see figure 5.6). Furthermore, since $^1/_{d_{fin}} \ll {}^1/_{d_{ini}}$ the term including d_{fin} can be neglected. With these modifications equation 3.6 becomes:

$$\left.\frac{\Delta L}{L_0}\right|_{\text{Grain Boundaries}} = \epsilon_{GB}\cos\phi\left[\frac{1}{\left(\frac{d_{ini,\perp}}{\cos\phi}\right)}\right] + \epsilon_{GB}\sin\phi\left[\frac{1}{\left(\frac{d_{ini,\parallel}}{\sin\phi}\right)}\right] \tag{5.9}$$

which can be written as:

$$\left.\frac{\Delta L}{L_0}\right|_{\text{Grain Boundaries}} = \epsilon_{GB}\left[\left(\frac{\cos^2\phi}{d_{ini,\perp}}\right) + \left(\frac{\sin^2\phi}{d_{ini,\parallel}}\right)\right] \tag{5.10}$$

where $d_{ini,\parallel}$ and $d_{ini,\perp}$ denote the crystallite sizes parallel to elongation direction and perpendicular to elongation direction respectively. With the results from the measurement series Ni5Tan (deformation by HPT, five turns) and the assumption that $\phi = 10°$ [17] the excess volume calculates as $\epsilon_{GB} = (36\pm12)$ pm (in axial direction) and $\epsilon_{GB} = (28\pm9)$ pm (in tangential direction). These values are slightly below the values reported by Steyskal [21] where the angle ϕ was considered zero (see below).

Turning to the samples deformed by ECAP, for the measurement series Ni12A (deformation by ECAP, twelve passes, route A) and Ni12BC (deformation by ECAP, twelve passes, route B_C) the tilt angle of the elongated crystallites is derived from electron microscopy images as $\phi = 23°$ in case of the Ni12A series and as $\phi = 33°$ in case of the Ni12BC series. For the Ni12A series equation 5.10 gives an excess volume of $\epsilon_{GB} = (50\pm8)$ pm (in normal direction) respectively of $\epsilon_{GB} = (21\pm4)$ pm (in extrusion direction). For the Ni12BC series the excess volume calculates as $\epsilon_{GB} = (46\pm13)$ pm (in normal direction) and as $\epsilon_{GB} = (25\pm6)$ pm (in extrusion direction). A full list of the grain boundary excess volumes for ultrafine-grained nickel can be found in table 5.5.

For comparison, using equation 3.6 with $\phi = 0°$ Oberdorfer [17] determined for nickel a grain boundary excess volume ϵ_{GB} of (32±5) pm from samples in axial and of (39±12) pm from samples in tangential orientation. Steyskal et al [16] found a grain boundary excess volume of (35±4) pm (axial orientation) respectively (32±4) pm (tangential orientation). Interestingly, if $\phi = 10°$ is assumed, the results of Steyskal are remarkably similar to the results for measurements series Ni5Tan. For these calculations only 15 samples were included (twelve samples in axial and three samples in tangential orientation). In this study 24 samples from the disc specimen Ni5Tan (four samples in axial and 20 samples in tangential orientation), eight samples from the rod specimen Ni12A (four samples each in extrusion and normal orientation) and ten samples from the rod specimen Ni12BC (five samples each in extrusion and normal orientation) were considered.

Grain boundary excess volumes for bcc and fcc metals have been calculated numerically by various computer simulations of grain boundaries [95, 96, 97, 98]. However, the choice of the interatomic potentials turned out to have significant impact on the results [95]. From molecular dynamics simulations excess volumes of 39 to 41 pm for high-angle grain boundaries in nickel [97] respectively of 28 to 42 pm for $\Sigma 5$ grain boundaries in nickel [98] have been calculated recently. The calculated values match nicely with the results for high-purity nickel deformed by HPT, and also match values for nickel deformed by ECAP and measured in extrusion direction.

Experimental data on grain boundary excess volumes from other techniques, however, is scarce. For gold excess volumes of 4 to 12 pm were found using TEM [99, 100]. For aluminum an excess volume of 64 pm was determined by measuring the grain boundary contact angle [101]. For nanocrystalline palladium an excess volume of 23 pm was calculated from density measurements [102]. Finally, in case of nanocrystalline iron an excess volume of 19 pm was

Table 5.5: Results for the activation energy Q according to the Kissinger analysis and for the grain boundary excess volume ϵ_{GB} perpendicular ($\perp$, axial and normal) and parallel ($\parallel$, tangential and extrusion) to the general direction of crystallite elongation. The direction of elongation is angled at the angle ϕ in respect to the plane normal of the measurement direction (for axial and normal orientations). Analysis of the results for stage B of annealing for the measurement series Ni5Tan (deformation by HPT, five turns), Ni12A (deformation by ECAP, twelve turns, route A) and Ni12BC (deformation by ECAP, twelve turns, route B_C). The tilt angle ϕ describes the angle between the crystallite elongation and measurement direction (see 5.6).

Series	ϕ	Q /eV	$\epsilon_{GB}\big\vert_{\perp}$ /pm	$\epsilon_{GB}\big\vert_{\parallel}$ /pm
Ni5Tan	10°	1.04±0.08	36±12	28±9
Ni12A	23°	1.21±0.10	50±8	21±4
Ni12BC	33°	1.42±0.24	46±13	25±6

found from grain growth kinetics [103]. Kuru et al [104] applied XRD measurements on nanocrystalline nickel thin films under stress and found an excess volume of 160 pm. These higher values indicate that the grain boundary excess volume might potentially be increased by external influence (such as external stress in case of Kuru et al [104]).

The substantial variation of the excess volume values with sample orientation for nickel deformed by ECAP show clearly that the length change during recrystallization does not strictly correlate to the crystallite size. This indicates that additional, anisotropic effect contributes to the length change during stage B. A few possible explanations can be given: (i) a higher amount of high-angle grain boundaries in normal direction coupled with a tilt angle dependence of the excess volume [105]; (ii) a contribution of remaining vacancies annealing at grain boundaries (see section 5.1.8); (iii) a texture effect which leads to a change of the packing density during recrystallization; or (iv) anisotropic internal strains localized at grain boundaries.

The fourth option (iv) becomes unlikely when the results from the peak broadening experiments (see section 4.3) are considered. The change of the FWHM correlates well with the crystallite sizes before and after recrystallization. The second option (ii), on the other hand, seems plausible considering that the crystallite sizes and therefore the necessary diffusion lengths after deformation by ECAP are larger than after deformation by HPT. However, further experiments are required before a conclusion can be reached.

5.3 Stage C – Grain growth

The third and final stage of the annealing of high-purity nickel after deformation by HPT or by ECAP has so far not been discussed as in-depth as the recovery and the recrystallization stages. Electron microscopy images show that recrystallization is mostly complete at the end of stage B [17, 21, 22] with only partial ultrafine-grained areas remaining. During stage C secondary grain growth is observed, but the small number of grain boundaries remaining after primary recrystallization lead only to a small volume change.

As a result the model developed by Neubauer [57] attributes the volume change during stage C by 50 % to a second recrystallization process and by 50 % to void shrinkage (see section 4.4). The secondary recrystallization process was modeled with an activation energy of 1.35 eV. The void shrinkage process was modeled using a pipe diffusion process. However, the activation energy of the pipe diffusion process had to be set to only 1.2 eV (from 1.2 eV [66]) to achieve a satisfying fit. Nonetheless, stage C could be modeled reasonably well with the combination of a second recrystallization process and void shrinkage.

Neutron diffraction measurements show that the FWHM decreases from 0.57° to 0.48° in the temperature window from 500 to 770 K for nickel deformed by HPT. For nickel deformed by ECAP the FWHM decreases from 0.52° to 0.49° in the temperature window from 570 to 770 K. Nickel annealed to 970 K shows a similar FWHM as nickel annealed to 770 K. Considering the similar peak broadening of the last sample, and considering the considerably small number of crystallites in dilatometry-shaped samples after annealing this peak broadening is most likely the technical limit of this measurement setup. Therefore, the FWHM data allow no conclusion regarding stage C.

As seen in table 5.1 the average length changes during stage C are significantly smaller after deformation by ECAP compared to deformation by HPT. This length change reduction is even more pronounced than the length change reduction observed during stage B. Nickel deformed by 16 turns of HPT shows a higher length change than nickel deformed by five turns of HPT. Therefore, it can be stated that the length change observed during stage C depends to the amount of deformation. That also means that the length change is not solely caused by grain growth. Instead, a significant contribution of the annealing of stable defects such as voids has to be expected.

The SQUID measurements (see section 5.5 below) indeed indicate the presence of nanovoids in nickel prepared by HPT or ECAP. The minimum radius of the nanovoids was calculated with values of 5.1 nm for nickel prepared by HPT, and 4.8 nm for nickel prepared by ECAP. However, annealing up to a temperature of even 770 K did not result in a reduction of the void radius. It seems that the size (or alternatively the concentration) of nanovoids depends only on the deformation method and remains stable beyond stage C. Until further research is done, though, the exact annealing processes occurring during stage C remain unclear.

5.4 The annealing stages of titanium

The measurement series performed with titanium processed by ECAP (measurements series Ti4A, see section 4.2.3) consisted of a considerably smaller number of samples. Nonetheless, measurements with samples of all orientations at different heating rates could be performed. Unlike nickel which has an isotropic fcc structure, the titanium performed by ECAP consists mostly of α-titanium with small volumes of ω-titanium [51]. Both of which are hexagonal and therefore anisotropic phases.

The combination of anisotropic phases and a strong texture from the deformation results in an anisotropic coefficient of thermal expansion. Therefore, difference dilatometry with a well-recrystallized reference sample will inevitably show an anisotropy of the thermal expansions. However, the derivatives by temperature still deliver valuable information about the changes caused by irreversible annealing effects.

From the derivatives of samples of different orientations five stages of defect annealing in ultrafine-grained titanium were identified:

- Stage A from 270 to 360 K
- Stage B from 360 to 500 K
- Stage C from 500 to 620 K
- Stage D from 620 to 740 K
- Stage E from 740 to 800 K

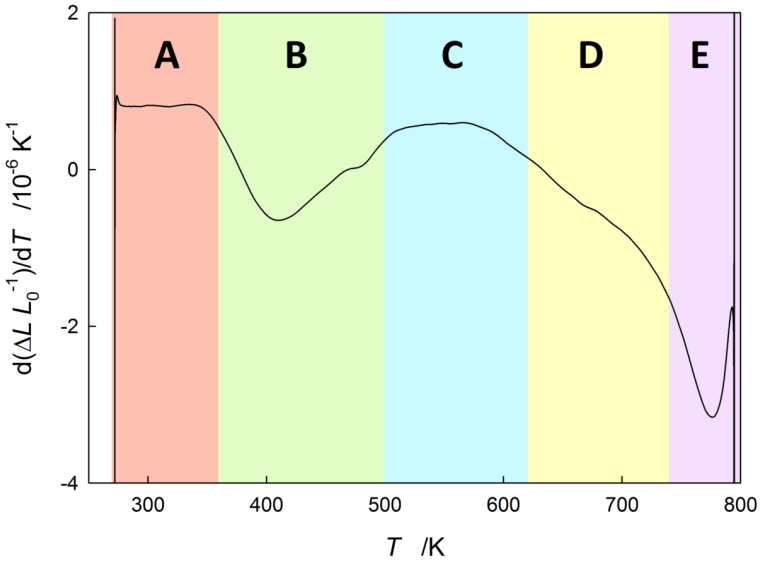

Figure 5.8: The five annealing stages of ultrafine-grained titanium deformed by ECAP. The dilatometry curve pictured is from the sample 0F1 (extrusion orientation, $\phi = 6.0\,\mathrm{K\,min^{-1}}$).

Figure 5.8 shows an example for the derivative of a difference dilatometry curve (sample 0F1 in extrusion orientation, $6.0\,\mathrm{K\,min^{-1}}$ heating rate) with the five stages marked. From the lack of extrema in the derivatives it can be concluded that during stage A no annealing takes place. Interestingly, the slope of the difference curves changes at about 360 K which manifests in a sharp drop in the derivative curve. This might indicate a phase change at that temperature, as the change of the slope is observed in samples of all orientations.

Stage E can easily be identified as recrystallization stage from the sharp minimum in the derivative curves. The stages B, C and D, on the other hand, seem to consist of recovery processes (see table 5.6). For samples in extrusion orientation the derivatives show a minimum (length decrease) either during stage B (well visible in figure 5.8) or stage C and a weak minimum during stage D (barely visible at about 660 K in 5.8). For samples

Table 5.6: Tentative assignment of recovery (R_C) and recrystallization (R_X) processes during the five annealing stages observed in different orientations (Or.) for ultrafine-grained titanium deformed by ECAP. A dash (—) signifies the lack of annealing processes.

Or.	A	B	C	D	E
E	—	R_C 1	R_C 1	R_C 2	R_X
N	—	R_C 1 & 2	R_C 2	—	R_X
V	—	—	R_C 1	R_C 2	R_X

of normal orientation the derivatives show a maximum (length increase) during stage B (as seen in figure 4.22) and a broad minimum during stage C which, however, occurs already halfway during stage B. For samples of transverse orientation the derivatives show two weak minima during the stages C and D (pictured in figure 4.22).

Except for samples of transverse orientation, a strong heating rate dependence can be observed. In combination with the strongly anisotropic coefficient of thermal expansion this effect makes an interpretation of the results difficult. Nonetheless, between two and three strongly anisotropic, heating rate dependent recovery processes can be identified. Additionally, a potential phase change and a recrystallization process are found in ultrafine-grained titanium prepared by ECAP. However, in order to gain more definite results, investigations with other, more sophisticated methods such as temperature-modulated dilatometry [106] are required.

5.5 Comparative studies of the magnetization behavior of nickel

Owing to magneto-elastic coupling the magnetization behavior upon approach to saturation magnetization is sensitive to the microstructure and the defect composition. Therefore, the magnetization behavior of nickel deformed by HPT or ECAP can provide valuable insight into the microstructure after the deformation. For this reason SQUID measurements of the magnetization behavior of nickel ideally complement the difference dilatometry measurements performed in this study.

A SQUID (superconducting quantum interference device) measurement device consists of one or more superconducting loops containing Josephson junctions [107]. The magnetic flux inside such a loop is quantized and any change to the flux by an external magnetic field is compensated by screening currents within the loop.

Although nickel is a ferromagnetic metal it is important to keep the magnetic background of the sample holder as low as possible. Furthermore, it is even more important to keep the background as constant as possible. In order to achieve this, Topolovec et al [108] developed a sample holder consisting of a nonmagnetic plastic cable tie in a nonmagnetic plastic tube. This sample holder is large enough that it can be moved freely through the superconducting loop without a change of the background magnetic field.

According to Kronmüller [109] the approach to magnetic saturation can be described by a power law where different parameters of the power law are connected to different defect types:

$$M(H) = M_S - \left(\frac{a_{1/2}}{H^{1/2}} + \frac{a_1}{H^1} + \frac{a_{3/2}}{H^{3/2}} + \frac{a_2}{H^2} + \frac{a_3}{H^3}\right) + \\ +\alpha\, T\sqrt{H} + \chi_P\, \mu_0\, H \tag{5.11}$$

where $M(H)$ denotes the magnetization in dependence of the applied field H, M_S the spontaneous magnetization, α a paramagnetic factor, T the temperature, χ_P the paramagnetic susceptibility, μ_0 the vacuum permeability, and a_n the parameters which describe type and concentrations of defects.

Kisker [110] uses a slightly modified equation 5.11 combined of terms from [111, 112, 113, 114]:

$$M(H) = M_S - \frac{a_{1/2}}{H^{1/2}} - \frac{a_1}{H^1} - \frac{a_2}{H^2} + c\,T\, f_{HP}(M_0,H) \tag{5.12}$$

with:

$$f_{HP}(M_0,H) = 3\sqrt{H} + \frac{M_0 + H}{\sqrt{M_0}}\, \arcsin\sqrt{\frac{M_0}{M_0 + H}} \tag{5.13}$$

where c denotes a material-specific constant.

For different dominating defect types, different power laws of H^{-n} dominate the equations 5.11 and 5.12. For point defects such as vacancies either $H^{-1/2}$ (in the case of point defects of smaller radius than the magnetic exchange length l_H of the external field) or H^{-2} is dominant. For dislocation dipoles either H^{-1} (in the case of dipole widths smaller than l_H) or H^{-2} is dominant. For straight dislocations H^{-2} is dominant. For nonmagnetic precipitates or voids either $H^{-1/2}$ (radius smaller than l_H) or $H^{-3/2}$ is dominant.

Table 5.7: List with the designations, preparation method (HPT, ECAP or cold rolled–CR), orientation (Or.) and properties of small dilatometry-shaped samples prepared for the SQUID measurements.

Sample	Process	Or.	Dimensions /mm^3	Mass /mg
HPT2	HPT	R	1.00×0.95×2.05	16.46
HPT4	HPT	A	1.00×1.05×2.05	16.85
HPT6	HPT	T	1.05×1.15×2.05	17.78
HPT7	HPT	T	1.00×1.05×2.00	17.75
HPT8	HPT	A	1.00×1.05×2.05	18.36
HPT3	HPT	R	1.05×1.10×2.05	17.97
ECAP1	ECAP	N	1.05×1.00×2.00	17.49
ECAP2	ECAP	E	1.05×1.00×2.00	17.37
REF1			1.15×1.10×2.10	19.91
REF2			1.10×1.10×2.15	20.38
CR1	CR	N	1.10×1.10×2.10	19.57
CR2	CR	E (R)	1.10×1.10×2.10	19.55

The SQUID measurements were performed by P. Ranacher during his masters thesis [115] using ultrafine-grained nickel prepared by HPT and ECAP. The ultrafine-grained nickel was provided by the author and prepared for the SQUID measurements under the author's supervision. Samples of dimensions $1\times1\times2\,\mathrm{mm}^3$ were cut from a disc specimen deformed by five turns of HPT ([22]) and from a rod specimen deformed by twelve passes of ECAP using route $\mathrm{B_C}$ (Ni12BC). Additionally, samples from cold-rolled nickel as well as undeformed nickel of identical composition were prepared. Table 5.7 lists the samples which were used for the measurements.

The magnetization behavior of the positive branches of the hysteresis loops were measured up to a magnetic field of $1.59\times10^6\,\mathrm{A\,m^{-1}}$. From the hysteresis loops the saturation magnetization M_0, the remanent magnetization M_r, the coercivity H_C and the permeability μ were deduced. All mea-

sured samples show almost identical saturation magnetization of roughly $M_0 = 55.3\,\mathrm{mA\,m^2\,g^{-1}}$ independent of deformation method or orientation. Furthermore, samples processed by HPT or ECAP show almost identical remanent magnetizations around $M_r = 2.3\,\mathrm{mA\,m^2\,g^{-1}}$ too. The cold-rolled and undeformed samples, however, showed a slightly lower remanent magnetization.

One axial and one tangential sample processed by HPT were annealed afterwards and measured again after each annealing step. The annealing states were 370 K (before stage A), 430 K (after stage A and before stage B), 490 K (after stage B and before stage C) and 770 K (after stage C). After none of the annealing stages a significant change of the saturation magnetization M_0 was observed. The remanent magnetization M_r and the coercivity H_C, on the other hand, are reduced clearly after annealing to 490 K (after recrystallization, stage B).

The coercivity H_C of nickel prepared by HPT and by ECAP is larger than the coercivity of nickel prepared by cold rolling and the reference material. During recrystallization (annealing to 490 K) the coercivity of nickel deformed by HPT decreases and the material becomes magnetically softer. It is well known that the coercivity of ferromagnetic materials such as nickel peaks at crystallite sizes of a few tens of nanometers and decreases with increasing crystallite sizes [116]. Thus, the increase of the crystallite size due to recrystallization explains the change of coercivity during stage B.

Figure 5.9 shows the positive hysteresis branch of one of the samples deformed by HPT (HPT4, not annealed). The curve can be divided in three regions: the low-field region up to $3.98\times10^4\,\mathrm{A\,m^{-1}}$ magnetic field, the medium-field region from 0.80×10^5 to $3.18\times10^5\,\mathrm{A\,m^{-1}}$ magnetic field and the high-field region above $0.80\times10^6\,\mathrm{A\,m^{-1}}$ magnetic field. In the low-field region the magnetization is governed by Bloch wall movement, while in the medium-

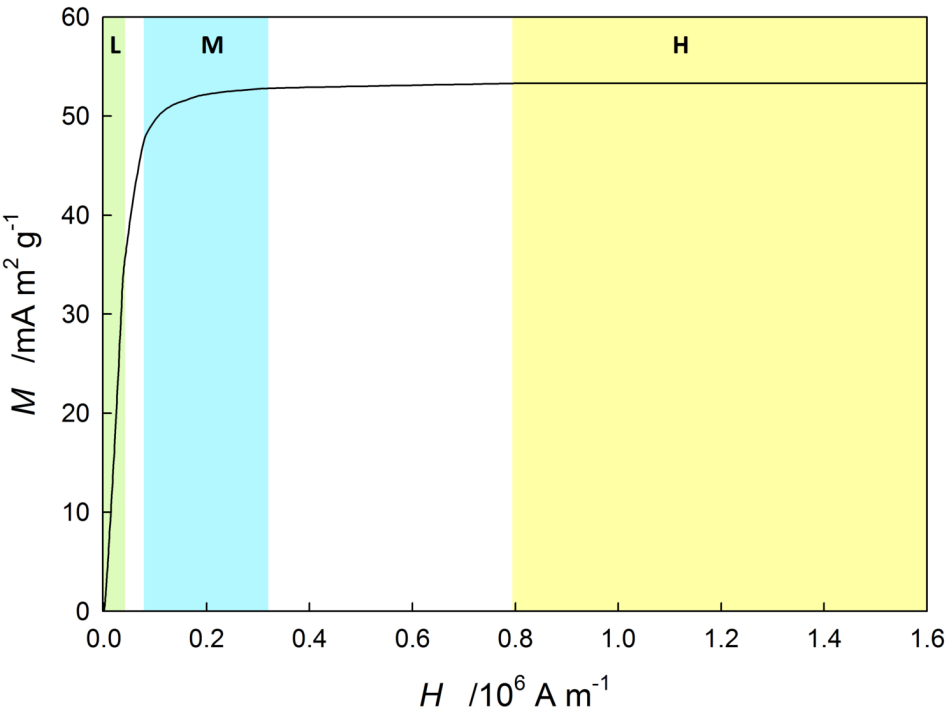

Figure 5.9: Definition of the low-, medium- and high-field areas (marked L, M and H) based on the magnetization curve of the sample HPT4 (after annealing to 770 K). The areas were identified from a $^{(1-M)}/_{M_0}$ over H plot (not shown here).

field region it is governed by domain rotation and magnetization [117]. In the high-field region defects are the main factor influencing the magnetization.

In the low-field region an increase of the initial permeability (the permeability μ at $H = 0$) of nickel prepared by HPT is observed after recrystallization (after annealing to the end of stage B at 490 K). This is another sign for the material becoming magnetically softer during recrystallization (stage B). The medium-field and high-field regions were analyzed in terms of M over H^{-n} plots where the x-axis was rescaled to H^{-n} and a linear fit was applied.

In the medium-field region the slopes of the M over $H^{-3/2}$ plots for nickel prepared by HPT, ECAP and cold rolling were notably higher than for the reference material (and nickel deformed by HPT after recrystallization at 490 K). This reflects in a slower approach to magnetic saturation for plastically deformed nickel. Both the M over $H^{-3/2}$ plots as well as the M over H behavior in general again indicate that nickel becomes magnetically softer during the recrystallization.

In the high-field region the magnetization behavior becomes dominated by the alignment of spins in the vicinity of lattice defects. The best linear fits were found for the M over $H^{-1/2}$ plots which are shown in figure 5.10. It was found that $H^{-1/2}$ is also the dominant factor in the fit where all exponents H^{-n} according to equation 5.12 are taken into account. Consequently, in the high-field region the $a_{1/2}$ parameter directly correlates with the slope of the M over $H^{-1/2}$ plot.

As seen in the linear fits depicted in figure 5.10 the parameter $a_{1/2}$ depends on the type of deformation. Figure 5.11 shows the parameter $a_{1/2}$ for different deformation methods over the annealing temperature. After deformation by HPT an average $a_{1/2}$ parameter of 0.86 mA m^2 g^{-1} was determined. However,

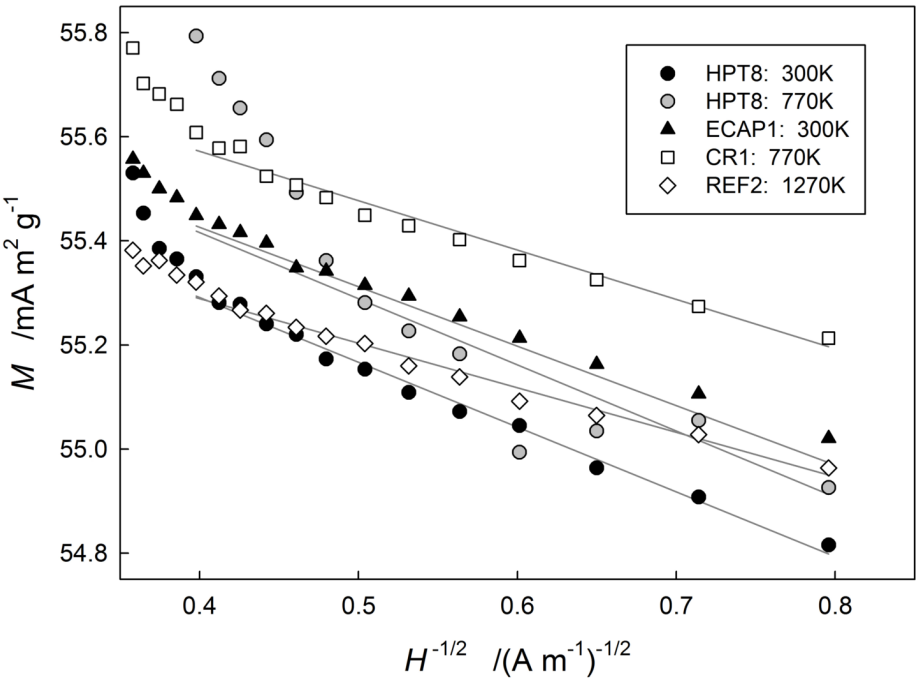

Figure 5.10: Linear fit of the magnetization of samples deformed by HPT, ECAP and cold rolling. On the x-axis the applied magnetic field H has been rescaled to $H^{-1/2}$.

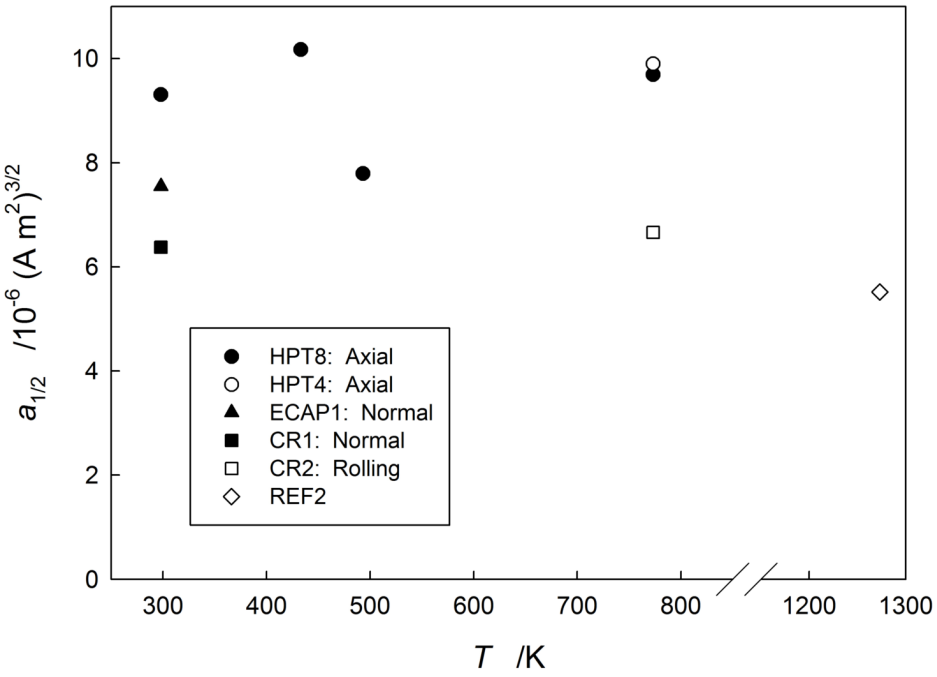

Figure 5.11: Parameter $a_{1/2}$ in relation to annealing temperature for samples deformed by HPT, ECAP and cold rolling. The parameters $a_{1/2}$ were gained from fitting the power law in equation 5.12 to the magnetization curves.

after deformation by ECAP or by cold-rolling as well as in undeformed nickel a lower average value of $a_{1/2} = 0.53\,\mathrm{mA\,m^2\,g^{-1}}$ was determined. Heat treatment does not seem to influence these parameters at all.

The dominance of $H^{-1/2}$ indicates that the approach to saturation magnetization is governed by non-magnetic spheres [109]. In case of high-purity nickel these spheres must be assumed to be nanovoids. Using this equation from the work of Kisker [110] the parameter $a_{1/2}$ was used to calculate the average radius r_0 of the voids associated with it:

$$a_{1/2} = \frac{\sqrt{2}\,\pi^2 M_S^{5/2}}{27\,\mu_0^{1/2} A_{Ex}^{1/2}}\, r_0^4\, N \tag{5.14}$$

where A_{Ex} denotes the exchange constant and N the number density of voids. The number density is a material specific quantity which is unknown for the nickel in question. Therefore only a maximum for N can be considered which gives:

$$N \leq \frac{3}{4\pi\, l_{Ex}^3} \tag{5.15}$$

where l_{Ex} denotes the exchange length. The maximum number density N is defined as the inverse of the exchange volume $\frac{4\pi}{3}\, l_{Ex}^3$ for which the model leading to equation 5.14 is defined [115].

Using an exchange constant $A_{Ex} = 3.5{\times}10^{-16}\,\mathrm{J\,m^{-1}}$ and an exchange length $l_{Ex} = 55\,\mathrm{nm}$ a minimum radius can be calculated. For nickel deformed by HPT values around $r_0 = 5.1\,\mathrm{nm}$ are determined. For nickel deformed by ECAP a value of about $r_0 = 4.8\,\mathrm{nm}$ is determined. The values for cold-rolled and undeformed nickel are between 4.5 to 4.7 nm. Interestingly, these mini-

mum radii seem to be independent of the annealing state. Nonetheless, the presence of nanovoids in nickel deformed by HPT or ECAP can be expected from dilatometry data on stage C, and the combination of void shrinkage with grain growth has been used successfully to model this annealing stage as seen in section 4.4.

6

Conclusions

In continuation of previous work conducted at this institute extensive difference dilatometry measurements of high-purity nickel deformed by HPT and ECAP were performed in the framework of this thesis. The difference dilatometry measurements were complemented by electron microscopy imaging, neutron diffraction measurements, SQUID measurements and numerical modeling.

A major focus of this work was on the anisotropy of the annealing behavior observed in a few samples during previous measurements. This behavior was proven consistent by means of a systematic investigation on a large set of samples performed in this work. This anisotropic annealing behavior occurs in a temperature window of 340 to 435 K respectively 370 to 500 K depending on deformation method. It manifests in an irreversible length increase in certain sample orientations which would indicate an increase of the excess volume associated with defects.

The comprehensive dilatometry measurements performed for the first time in this study showed a dependence of the irreversible length increase on the position of the sample within the disc specimen. The most reproducible

results were gained from samples cut out at the edge of the disc specimen. This effect is attributed to the elongation of crystallites along the shear direction: in samples from the edge of a disc specimen the crystallites are aligned more parallel than in samples from the center. Samples from a disc specimen deformed to very high strains (up to $\varepsilon = 100$) furthermore showed a heating rate dependence of the irreversible length increase.

Two potential explanations for the anisotropic annealing behavior have been put forward: residual stresses and anisotropic vacancy annealing. The massive plastic deformation during the HPT and ECAP processes has been proven to result in residual stresses. If theses residual stresses remain present even after cutting the disc or rod specimen into dilatometry samples, the heating during dilatometry measurements might result in a sample deformation which can be measured as irreversible length increase.

In order to test this hypothesis, disc specimen deformed by HPT were post-processed elastically as well as plastically. An elastic or plastic deformation in the presence of residual stresses would result in a plastic flow which removes any residual stress. While the results for elastically post-processed nickel were inconclusive due to technical limitations, the plastically post-processed nickel did still show the anisotropic annealing behavior observed without post-processing.

In a related experiment one series of dilatometry samples in tangential orientation were prepared with non-planar bases, but with a thin bar at one of their bases instead. If the length increase is caused by sample deformation, a dependency of the length increase on the orientation of this bar relative to the disc specimen would be observed. The results, however, of this series did not show any difference between samples with a bar parallel to axial direction, samples with a bar parallel to radial direction, and samples with no bar at all.

Neutron diffraction measurements intended to directly identify potential residual stresses showed the expected residual stresses in a disc specimen prepared by HPT. However, dilatometry samples cut from such a disc specimen did not show signs of residual stress. Measurements using the $\sin^2\psi$ method with samples in axial, radial and tangential orientation showed no slopes in the 2θ versus $\sin^2\psi$ plots indicating the absence of residual stresses. Considering the results from post-processed nickel, samples with non-planar bases and neutron diffraction measurements it can be concluded that there are no macroscopic residual stresses left in the dilatometry samples, and that the anisotropic annealing behavior is not caused by residual stresses.

Therefore, this supports the notion that the irreversible length increase is caused by vacancies annealing perpendicular to the direction of crystallite elongation in combination with an isotropic outward expansion of the lattice when vacancies anneal. This allowed for the calculation of the volume of a relaxed vacancy V_V in nickel from the measured length changes and the orientation of the crystallites within the dilatometry samples. After deformation by HPT a vacancy volume of $0.49\,\Omega$ is found. For the first time difference dilatometry on ultrafine-grained nickel prepared by ECAP was performed too and from these results a vacancy volume of $0.44\,\Omega$ was determined.

The recrystallization process following the recovery has been studied more in-detail as well. The activation energy of the recrystallization could be determined from a large sample size and was found to match well for deformation by HPT as well as ECAP. Additionally, the grain boundary excess volumes for samples deformed by HPT and by ECAP were calculated and were found not only to match earlier results by Steyskal, but also results of numerical calculations. In case of deformation by ECAP a dependency of the grain boundary excess volume on the sample orientation was observed. A few possible explanations for this observation were given.

In general the annealing behavior of ultrafine-grained nickel deformed by ECAP turned out to be almost identical to that deformed by HPT. The same three stages A, B and C of annealing are observed of which the first (stage A) shows the same irreversible length increase as nickel deformed by HPT. The annealing stages for nickel deformed by ECAP are slightly shifted towards higher temperatures which is probably a result of the lower defect density which results from a smaller applied strain. The lower defect density also manifests in a smaller amplitude of the length changes in all stages of the annealing.

In addition, difference dilatometry measurements were also performed on ultrafine-grained titanium processed by ECAP. However, due to a strongly anisotropic coefficient of thermal expansion, analysis of the results becomes very difficult. Nonetheless, ultrafine-grained titanium showed an anisotropic, multi-stage annealing behavior as well. Like ultrafine-grained nickel an irreversible length increase was observed during the recovery of the ultrafine-grained titanium.

Bibliography

[1] C. Koch: *Optimization of strength and ductility in nanocrystalline and ultrafine grained metals*, Scr. Mater. **49** (2003) 657–662

[2] R. Valiev, Y. Estrin, Z. Horita, T. Langdon, M. Zehetbauer, Y. Zhu: *Fundamentals of Superior Properties in Bulk NanoSPD Materials*, Mater. Res. Lett. **4** (2016) 1–21

[3] L. Liu, Y. Li, F. Wang: *Electrochemical Corrosion Behavior of Nanocrystalline Materials—a Review*, J. Mater. Sci. Technol. **26** (2010) 1–14

[4] A. Zhilyaev, T. Langdon: *Using high-pressure torsion for metal processing: Fundamentals and applications*, Prog. Mater. Sci. **53** (2008) 893–979

[5] R. Valiev, T. Langdon: *Principles of equal-channel angular pressing as a processing tool for grain refinement*, Prog. Mater. Sci. **51** (2006) 881–981

[6] T. Langdon: *Twenty-five years of ultrafine-grained materials: Achieving exceptional properties through grain refinement*, Acta Mater. **61** (2013) 7035–7059

[7] E. Schafler, R. Pippan: *Effect of thermal treatment on microstructure in high pressure torsion (HPT) deformed nickel*, Mater. Sci. Eng., A **387** (2004) 799–804

[8] R. Valiev, I. Sabirov, A. Zhilyaev, T. Langdon: *Bulk Nanostructured Metals for Innovative Applications*, JOM **64** (2012) 1134–1142

[9] D. Hughes, N. Hansen: *Microstructure and strength of nickel at large strains*, Acta Mater. **48** (2000) 2985–3004

[10] R. Figueiredo, T. Langdon: *Using Severe Plastic Deformation for the Processing of Advanced Engineering Materials*, Mater. Trans. **50** (2009) 1613–1619

[11] M. Starink, X. Cheng, S. Yang: *Hardening of pure metals by high-pressure torsion: A physically based model employing volume-averaged defect evolutions*, Acta Mater. **61** (2013) 183–192

[12] W. Sprengel, B. Oberdorfer, E.-M. Steyskal, R. Würschum: *Dilatometry: a powerful tool for the study of defects in ultrafine-grained metals*, J. Mater. Sci. **47** (2012) 7921–7925

[13] R. Würschum, B. Oberdorfer, E.-M. Steyskal, W. Sprengel, W. Puff, P. Pikart, C. Hugenschmidt, R. Pippan: *Free volumes in bulk nanocrystalline metals studied by the complementary techniques of positron annihilation and dilatometry*, Physica B **407** (2012) 2670–2675

[14] D. Setman, E. Schafler, E. Korznikova, M. Zehetbauer: *The presence and nature of vacancy type defects in nanometals detained by severe plastic deformation*, Mater. Sci. Eng., A **493** (2008) 116–122

[15] B. Oberdorfer, B. Lorenzoni, K. Unger, W. Sprengel, M. Zehetbauer,

R. Pippan, R. Würschum: *Absolute concentration of free volume-type defects in ultrafine-grained Fe prepared by high-pressure torsion*, Scr. Mater. **63** (2010) 452–455

[16] E.-M. Steyskal, B. Oberdorfer, W. Sprengel, M. Zehetbauer, R. Pippan, R. Würschum: *Direct Experimental Determination of Grain Boundary Excess Volume in Metals*, Phys. Rev. Lett. **108** (2012) 055 504

[17] B. Oberdorfer: *Atomic Free Volume in Bulk Nanocrystalline Metals studied by Dilatometry and Positron Annihilation*, Doctoral thesis, Graz University of Technology, Austria (2012)

[18] G. Rathmayr, R. Pippan: *Influence of impurities and deformation temperature on the saturation microstructure and ductility of HPT-deformed nickel*, Acta Mater. **59** (2011) 7228–7240

[19] Y. Todaka, M. Umemoto, A. Yamazaki, J. Sasaki, K. Tsuchiya: *Influence of High-Pressure Torsion Straining Conditions on Microstructure Evolution in Commercial Purity Aluminum*, Mater. Trans. **49** (2008) 7–14

[20] D. Orlov, Y. Todaka, M. Umemoto, N. Tsuji: *Role of strain reversal in grain refinement by severe plastic deformation*, Mater. Sci. Eng., A **499** (2009) 427–433

[21] E.-M. Steyskal: *Untersuchung freier Volume in submikrokristallinem Nickel mit der Methode der Dilatometrie*, Master thesis, Graz University of Technology, Austria (2010)

[22] J. Kotzurek: *Defektuntersuchungen mittels Dilatometrie an*

feinkörnigem Nickel nach Tieftemperaturverformung, Master thesis, Graz University of Technology, Austria (2013)

[23] R. Simmons, R. Balluffi: *Measurements of Equilibrium Vacancy Concentrations in Aluminum*, Phys. Rev. **117** (1960) 52–61

[24] B. Oberdorfer, E.-M. Steyskal, W. Sprengel, W. Puff, P. Pikart, C. Hugenschmidt, M. Zehetbauer, R. Pippan, R. Würschum: *In Situ Probing of Fast Defect Annealing in Cu and Ni with a High-Intensity Positron Beam*, Phys. Rev. Lett. **105** (2010) 146 101

[25] B. Oberdorfer, E.-M. Steyskal, W. Sprengel, R. Pippan, M. Zehetbauer, W. Puff, R. Würschum: *Recrystallization kinetics of ultrafine-grained Ni studied by dilatometry*, J. Alloys Compd. **509S** (2011) S309–S311

[26] B. Oberdorfer, D. Setman, E.-M. Steyskal, A. Hohenwarter, W. Sprengel, M. Zehetbauer, R. Pippan, R. Würschum: *Grain boundary excess volume and defect annealing of copper after high-pressure torsion*, Acta Mater. **68** (2014) 189–195

[27] K. Klement: *Nichtgleichgewichtsdefekte in extrem verformten Metallen*, Doctoral thesis, University of Augsburg, Germany (2007)

[28] O. Pedersen, L. Brown, W. Stobbs: *The bauschinger effect in copper*, Acta Metall. **29** (1981) 1843–1850

[29] J. Jonas, C. Ghosh, L. Tóth: *The equivalent strain in high pressure torsion*, Mater. Sci. Eng., A **607** (2014) 530–535

[30] R. Pippan, F. Wetscher, M. Hafok, A. Vorhauer, I. Sabirov: *The Lim-*

its of Refinement by Severe Plastic Deformation, Adv. Eng. Mater. **8** (2006) 1046–1056

[31] M. Zehetbauer, V. Seumer: *Cold work hardening in stages IV and V of f.c.c. metals–I. experiments and interpretation*, Acta Metall. Mater. **41** (1993) 577–588

[32] M. Zehetbauer: *Cold work hardening in stages IV and V of f.c.c. metals–II. model fits and physical results*, Acta Metall. Mater. **41** (1993) 589–599

[33] O. Renk, A. Hohenwarter, S. Wurster, R. Pippan: *Direct evidence for grain boundary motion as the dominant restoration mechanism in the steady-state regime of extremely cold-rolled copper*, Acta Mater. **77** (2014) 401–410

[34] Y. Iwahashi, J. Wang, Z. Horita, M. Nemoto, T. Langdon: *Principle of equal-channel angular pressing for the processing of ultra-fine grained materials*, Scr. Mater. **35** (1996) 143–146

[35] Y. Iwahashi, Z. Horita, M. Nemoto, T. Langdon: *The process of grain refinement in equal-channel angular pressing*, Acta Mater. **46** (1998) 3317–3331

[36] A. Zhilyaev, B.-K. Kim, G. Nurislamova, M. Baró, J. Szpunar, T. Langdon: *Orientation imaging microscopy of ultrafine-grained nickel*, Scr. Mater. **46** (2002) 575–580

[37] D. Hughes, N. Hansen, D. Bammann: *Geometrically necessary boundaries, incidental dislocation boundaries and geometrically necessary dislocations*, Scr. Mater. **48** (2003) 147–153

[38] K. Unger: *Bestimmung der Curie-Temperatur von Nickel zur heizratenabhängigen Temperaturkalibrierung eines Differenz-Dilatometers* (2010)

[39] V. Segal: *Severe plastic deformation: simple shear versus pure shear*, Mater. Sci. Eng., A **338** (2002) 331–344

[40] M. Abràmoff, P. Magalhães, J. Sunanda: *Image Processing with ImageJ*, Biophotonics Intern. **11** (2004) 36–42

[41] A. Wilkinson, T. Britton: *Strains, planes, and EBSD in materials science*, Materials Today **15** (2012) 366–376

[42] W. Bragg, W. Bragg: *The Reflection of X-rays by Crystals*, Proc. Roy. Soc. London **88** (1913) 428–438

[43] G. Webster, R. Wimpory: *Non-destructive measurement of residual stress by neutron diffraction*, J. Mater. Process. Technol. **117** (2001) 395–399

[44] B. Eigenmann, E. Macherauch: *Röntgenographische Untersuchung von Spannungszuständen in Werkstoffen Teil I*, Materialwiss. Werkstofftech. **26** (1995) 148–160

[45] B. Eigenmann, E. Macherauch: *Röntgenographische Untersuchung von Spannungszuständen in Werkstoffen Teil II*, Materialwiss. Werkstofftech. **26** (1995) 199–216

[46] C. Randau, U. Garbe, H.-G. Brokmeier: *StressTextureCalculator: a software tool to extract texture, strain and microstructure information from area-detector measurements*, J. Appl. Crystallogr. **44** (2011) 641–646

[47] H.-G. Brokmeier, W. Gan, C. Randau, M. Völler, J. Rebelo-Kornmeier, M. Hofmann: *Texture analysis at neutron diffractometer STRESS-SPEC*, Nucl. Instrum. Methods Phys. Res., Sect. A **642** (2011) 87–92

[48] M. Hofmann, W. Gan, J. Rebelo-Kornmeier: *STRESS-SPEC: Materials science diffractometer*, JLSRF **1** (2015) A6

[49] H. Kissinger: *Variation of Peak Temperature With Heating Rate In Differential Thermal Analysis*, J. Res. Nat. Bur. Stand. **57** (1956) 217–221

[50] S. Kalpakjian, S. Schmid: *Manufacturing Processes for Engineering Materials, 5th Edition* (Pearson) (2008)

[51] A. Jäger, V. Gärtnerova, K. Tesař: *Microstructure and anisotropy of the mechanical properties in commercially pure titanium after equal channel angular pressing with back pressure at room temperature*, Mater. Sci. Eng., A **644** (2015) 114–120

[52] S. Ferrasse, V. Segal, S. Kalidindi, F. Alford: *Texture evolution during equal channel angular extrusion Part I. Effect of route, number of passes and initial texture*, Mater. Sci. Eng., A **368** (2004) 28–40

[53] S. Ferrasse, V. Segal, F. Alford: *Texture evolution during equal channel angular extrusion (ECAE) Part II. An effect of post-deformation annealing*, Mater. Sci. Eng., A **372** (2004) 235–244

[54] A. Guz', F. Makhort: *The physical fundamentals of the ultrasonic nondestructive stress analysis of solids*, Int. Appl. Mech. **36** (2000) 1119–1149

[55] G. Albertini, G. Bruno, A. Carradò, F. Fiori, M. Rogante, F. Rustichelli: *Determination of residual stresses in materials and industrial components by neutron diffraction*, Meas. Sci. Technol. **10** (1999) 56–73

[56] A. Gazder, F. Dalla Torre, C. Gu, C. Davies, E. Pereloma: *Microstructure and texture evolution of bcc and fcc metals subjected to equal channel angular extrusion*, Mater. Sci. Eng., A **415** (2006) 126–139

[57] C. Neubauer: *Modellierung dilatometrischer Messdaten zum mehrstufigen Ausheilen von Überschussvolumen in Metallen nach starker plastischer Verforumng*, Master thesis, Graz University of Technology, Austria (2015)

[58] J. Crank: *The Mathematics of Diffusion* (Oxford Press) (1975)

[59] D. Seidman, R. Balluffi: *Sources of Thermally Generated Vacancies in Single-Crystal and Polycrystalline Gold*, Phys. Rev. **139** (1965) 1824–1840

[60] W. Johnson, R. Mehl: *Reaction kinetics in processes of nucleation and growth*, Trans. Am. Inst. Min. Metall. Eng. **135** (1939) 416–442

[61] M. Avrami: *Kinetics of Phase Change. I General Theory*, J. Chem. Phys. **7** (1939) 1103–1112

[62] A. Kolmogorov: *On the statistical theory of metal crystallisation*, Izv. Akad. Nauk SSSR, Ser. Fiz. **3** (1939) 355–359

[63] D. Henderson: *Thermal analysis of non-isothermal crystallization kinetics in glass forming liquids*, J. Non-Cryst. Solids **30** (1979) 301–315

[64] T. Ungár, E. Schafler, P. Hanák, S. Bernstorff, M. Zehetbauer: *Vacancy production during plastic deformation in copper determined by in situ X-ray diffraction*, Mater. Sci. Eng., A **462** (2007) 398–401

[65] H. Bowden, R. Balluffi: *Measurements of Self-diffusion Coefficients in Copper from the Annealing of Voids*, Philos. Mag. **19** (1969) 1001–1014

[66] M. Wuttig, H. Birnbaum: *Self-Diffusion along Edge Dislocations in Nickel*, Phys. Rev. **147** (1966) 495–505

[67] G. White, O. Madelung, B. Eisenmann, H. Schäfer, P. Ehrhart, H. Mehrer, N. Stolica, N. Stolwijk, A. LeClaire, I. Kaur, W. Gust: *Landolt-Börnstein* (Springer) (1961)

[68] J. Kotzurek, E.-M. Steyskal, B. Oberdorfer, A. Hohenwarter, R. Pippan, W. Sprengel, R. Würschum: *Direct measurement of vacancy relaxation by dilatometry*, Appl. Phys. Lett. **109** (2016) 021 906

[69] M. Zehetbauer, J. Kohout, E. Schafler, F. Sachslehner, A. Dubravina: *Plastic deformation of nickel under high hydrostatic pressure*, J. Alloys Compd. **378** (2004) 329–334

[70] B. Scherwitzl: *Dilatometrische Untersuchungen freier Volume in submikrokristallinem Eisen nach Hochverformung*, Master thesis, Graz University of Technology, Austria (2012)

[71] G. Abrosimova, N. Afonikova, Y. Estrin, N. Kobelev, E. Kolyvanov: *Orientation dependence of elastic properties and internal stresses in sub-microcrystalline copper produced by equal channel angular pressing*, Acta Mater. **58** (2010) 6656–6664

[72] A. Hohenwarter, A. Bachmaier, B. Gludovatz, S. Scheriau, R. Pip-

pan: *Technical parameters affecting grain refinement by high pressure torsion*, Int. J. Mater. Res. **100** (2009) 1653–1661

[73] M. Zehetbauer, E. Schafler, T. Ungár: *Non-microscopical methods for characterization of microstructures and properties of UFG metals*, Int. J. Mater. Res. **98** (2007) 290–298

[74] D. Bacon, D. Hull: *Introduction to Dislocation, 5th Edition* (Butterworth-Heinemann) (2011)

[75] C. Zener: *Theory of Lattice Expansion Introduced by Cold-work*, Trans. Am. Inst. Min. Metall. Eng. **147** (1942) 361–364

[76] A. Seeger, E. Mann: *Anwendung der nichtlinearen Elastizitätstheorie auf Fehlstellen in Kristallen*, Z. Naturforsch., A: Phys. Sci. **14** (1959) 154–164

[77] R. Toupin, R. Rivlin: *Dimensional Changes in Crystals Caused by Dislocations*, J. Math. Phys. **1** (1960) 8–15

[78] A. Zhilyaev, B.-K. Kim, J. Szpunar, M. Baró, T. Langdon: *The microstructural characteristics of ultrafine-grained nickel*, Mater. Sci. Eng., A **391** (2005) 377–389

[79] H. Zhang, X. Huang, N. Hansen: *Evolution of microstructural parameters and flow stresses toward limits in nickel deformed to ultra-high strains*, Acta Mater. **56** (2008) 5451–5465

[80] K. Raju, M. Krishna, K. Padmanabhan, V. Sarma, N. Gurao, G. Wilde: *Microstructure evolution and hardness variation during annealing of equal channel angular pressed ultra-fine grained nickel subjected to 12 passes*, J. Mater. Sci. **46** (2011) 2662–2671

[81] G. Rathmayr, A. Hohenwarter, R. Pippan: *Influence of grain shape and orientation on the mechanical properties of high pressure torsion deformed nickel*, Mater. Sci. Eng., A **560** (2013) 224–231

[82] M. Hafok, R. Pippan: *High-pressure torsion applied to nickel single crystals*, Philos. Mag. **88** (2008) 1857–1877

[83] A. Metsue, A. Oudriss, J. Bouhattate, X. Feaugas: *Contribution of the entropy on the thermodynamic equilibrium of vacancies in nickel*, J. Chem. Phys. **140** (2014) 104 705

[84] F. Gao, D. Bacon, G. Ackland: *Point-defect and threshold displacement energies in Ni_3Al I. Point-defect properties*, Philos. Mag. A **67** (1993) 275–288

[85] S. de Debiaggi, B. Decorte, A. Monti: *Diffusion by vacancy mechanism in Ni, Al, and Ni3Al: Calculation based on many-body potentials*, Phys. Status Solidi B **195** (1996) 37–54

[86] M. Ortega, S. de Debiaggi, A. Monti: *Self-Diffusion in FCC Metals: Static and Dynamic Simulations in Aluminium and Nickel*, Phys. Status Solidi B **234** (2002) 506–521

[87] O. Bender, P. Ehrhart: *Self-interstitial atoms, vacancies and their agglomerates in electron-irradiated nickel investigated by diffuse scattering of x-rays*, J. Phys. F: Met. Phys. **13** (1983) 911–928

[88] N. Chetty, M. Weinert, T. Rahman, J. Davenport: *Vacancies and impurities in aluminum and magnesium*, Phys. Rev. B: Condens. Matter Mater. Phys. **52** (1995) 6313–6326

[89] N. Kurita, H. Numakura: *Formation volume of atomic vacancies in*

body-centred cubic metals, Z. Metallkd. **95** (2004) 876–879

[90] A. Scholz, A. Seeger: *Verzerrungsfeld und mechanische Relaxation von Leerstellen in Germanium*, Phys. Status Solidi **3** (1963) 1480–1490

[91] B. Meyer, M. Fähnle: *Ab initio calculation of the formation energy and the formation volume of monovacancies in Mo*, Phys. Rev. B: Condens. Matter Mater. Phys. **56** (1997) 13 595–13 598

[92] P. Söderlind, L. Yang, J. Moriarty, J. Wills: *First-principles formation energies of monovacancies in bcc transition metals*, Phys. Rev. B: Condens. Matter Mater. Phys. **61** (2000) 2579–2586

[93] D. Setman, M. B. Kerber, E. Schafler, M. Zehetbauer: *Activation Enthalpies of Deformation-Induced Lattice Defects in Severe Plastic Deformation Nanometals Measured by Differential Scanning Calorimetry*, Metall. Mater. Trans. A **41** (2010) 810–815

[94] K. Detert, G. Dressler: *Rekristallisationsverhalten von zonengeschmolzenem Nickel*, Acta Metall. **13** (1965) 845–853

[95] D. Wolf: *Correlation between energy and volume expansion for grain boundaries in FCC metals*, Scr. Metall. **23** (1989) 1913–1918

[96] D. Wolf: *Correlation between the energy and structure of grain boundaries in b.c.c. metals. II. Symmetrical tilt boundaries*, Philos. Mag. A **62** (1990) 447–464

[97] H. Zhang, D. Srolovitz: *Simulation and analysis of the migration mechanism of Σ5 tilt grain boundaries in an fcc metal*, Acta Mater. **54** (2006) 623–633

[98] D. Olmsted, S. Foiles, E. Holm: *Survey of computed grain boundary properties in face-centered cubic metals: I. Grain boundary energy*, Acta Mater. **57** (2009) 3694–3703

[99] K. Merkle: *Quantification of atomic-scale grain-boundary parameters by high-resolution electron-microscopy*, Ultramicroscopy **40** (1992) 281–290

[100] M. Buckett, K. Merkle: *Determination of grain boundary volume expansion by HREM*, Ultramicroscopy **56** (1994) 71–78

[101] L. Shvindlerman, G. Gottstein, V. Ivanov, D. Molodov, D. Kolesnikov, W. Łojkowski: *Grain boundary excess free volume—direct thermodynamic measurement*, J. Mater. Sci. **41** (2006) 7725–7729

[102] R. Birringer, C. Krill, M. Klingel: *Orientation-phase-space-averaged properties of grain boundaries*, Philos. Mag. Lett. **72** (1995) 71–77

[103] C. Krill, L. Helfen, D. Michels, H. Natter, A. Fitch, O. Masson, R. Birringer: *Size-Dependent Grain-Growth Kinetics Observed in Nanocrystalline Fe*, Phys. Rev. Lett. **86** (2001) 842–845

[104] Y. Kuru, M. Wohlschlögel, U. Welzel, E. Mittemeijer: *Large excess volume in grain boundaries of stressed, nanocrystalline metallic thin films: Its effect on grain-growth kinetics*, Appl. Phys. Lett. **95** (2009) 163 112

[105] J. Bean, K. McKenna: *Origin of differences in the excess volume of copper and nickel grain boundaries*, Acta Mater. **110** (2016) 246–257

[106] M. Luckabauer, W. Sprengel, R. Würschum: *A high-stability non-*

contact dilatometer for low-amplitude temperature-modulated measurements, Rev. Sci. Instrum. **87** (2016) 075 116

[107] B. Josephson: *Possible new effects in Superconductive tunnelling*, Phys. Lett. **1** (1962) 251–253

[108] S. Topolovec, H. Krenn, R. Würschum: *Electrochemical cell for in situ electrodeposition of magnetic thin films in a superconducting quantum interference device magnetometer*, Rev. Sci. Instrum. **86** (2015) 063 903

[109] H. Kronmüller, M. Fähnle: *Micromagnetism and the microstructure of ferromagnetic solids* (Cambridge University Press) (2003)

[110] H. Kisker: *Magnetische Eigenschaften und Mikrostruktur von nanokristallinem Nickel*, Doctoral thesis, University of Stuttgart, Germany (1995)

[111] H. Kronmüller: *Mikromagnetische Berechnung der Magnetisierung in der Umgebung unmagnetischer Einschlüsse in Ferromagnetika*, Z. Angew. Phys. **168** (1962) 478–494

[112] M. Fähnle, H. Kronmüller: *The influence of spatially random magnetostatic, magnetocrystalline, magnetostrictive and exchange fluctuations on the law of approach to ferromagnetic saturation of amorphous ferromagnets*, J. Magn. Magn. Mater. **8** (1978) 149–156

[113] H. Chang, R. Herz, H. Kronmüller: *High-field susceptibility of EuS single crystals*, Appl. Phys. A: Mater. Sci. Process. **22** (1980) 155–160

[114] H. Kronmüller, N. Lenge, H.-U. Habermeier: *Investigation of the ap-*

proach to ferromagnetic saturation in sputtered amorfilms $Fe_{80-x}Ni_xB_{20}$ films, Phys. Lett. A **101** (1984) 439–442

[115] P. Ranacher: *Magnetization behavior of submicrocrystalline nickel prepared by extreme plastic deformation*, Master thesis, Graz University of Technology, Austria (2016)

[116] J. Löffler, J. Meier, B. Doudin, J.-P. Ansermet, W. Wagner: *Random and exchange anisotropy in consolidated nanostructured Fe and Ni: Role of grain size and trace oxides on the magnetic properties*, Phys. Rev. B: Condens. Matter Mater. Phys. **57** (1998) 2915–2924

[117] C. Kittel: *Introduction to solid state physics* (Oldenbourg) (2013)

Appendix

The available overviews of the disc and rod specimens used for the difference dilatometry measurements are listed in the following table along with the method of deformation (CR indicates subsequent cold rolling).

Series	Method	Overview
Ni5Tan	HPT	Figure 4.1
Ni16Tan	HPT	Figure 4.7a
Ni16CR	HPT & CR	Figure 4.7b
Ni5BB	HPT	Figure 4.12
Ni4BC	ECAP	Figure 4.15
Ni12A	ECAP	Figure 4.18a
Ni12BC	ECAP	Figure 4.18b

The following numbered list contains a collection of all 217 dilatometry measurements performed during the work on this doctoral thesis. The list contains the ongoing, hexadecimal numbering (numbers 001 to 02B were assigned during the diploma thesis), the name, the orientation (Or.), the heating rate φ, the date of the measurement and optional comments to the sample or measurement. The orientations are designated as A (axial orientation), R (radial orientation) and T (tangential orientation) for deformation

by HPT (see figure 3.6), and as E (extrusion orientation), N (normal orientation), V (transverse orientation) for deformation by ECAP (see figure 3.7).

N°	Label	Or.	φ /K min^{-1}	Date	Comments
02C	Ni10Ten_T20a	T	3.0	2013/07/18	Tilted towards R
02D	Ni10Ten_T20b	T	6.0	2013/07/19	Tilted towards R
02E	Ni10Ten_T20c	T	3.0	2013/07/22	Tilted towards R
02F	Ni10Ten_T20d	T	1.5	2013/07/24	Tilted towards R
030	Ni10NTen_T20e	T	6.0	2013/08/13	Tilted towards R
031	Ni10NTen_T20f	T	3.0	2013/08/14	Tilted towards R
032	Ni10NTen_A20a	A	3.0	2013/10/01	
033	Ni4BC_T3a	V	1.5	2013/10/03	
034	Ni4BC_T3b	V	3.0	2013/10/04	
035	Ni4BC_T3c	V	6.0	2013/10/07	
036	Ni4BC_N3a	N	1.5	2013/10/08	
037	Ni4BC_E3a	E	1.5	2013/10/09	
038	Ni4BC_N3b	N	3.0	2013/10/10	
039	Ni4BC_N3c	N	6.0	2013/10/11	
03A	Ni4BC_E3b	E	3.0	2013/10/14	
03B	Ni4BC_E3c	E	6.0	2013/10/15	
03C	Ni4BC_E3d	E	1.5	2013/10/21	
03D	Ni4BC_N3d	N	6.0	2013/10/23	
03E	Ni5Tan_T40a	T	3.0	2014/02/04	
03F	Ni5Tan_T30a	T	3.0	2014/02/05	
040	Ni5Tan_T20a	T	3.0	2014/02/06	
041	Ni5Tan_T12a	T	3.0	2014/02/07	
042	Ni5Tan_T12b	T	6.0	2014/02/10	
043	Ni5Tan_T20b	T	6.0	2014/02/11	
044	Ni5Tan_T30b	T	6.0	2014/02/12	
045	Ni5Tan_T40b	T	6.0	2014/02/13	
046	Ni5Tan_T40c	T	1.5	2014/02/20	
047	Ni5Tan_T30c	T	1.5	2014/02/21	
048	Ni5Tan_T40e	T	3.0	2014/02/27	

N°	Label	Or.	φ /K min^{-1}	Date	Comments
049	Ni5Tan_T40f	T	6.0	2014/02/28	
04A	Ni5Tan_T30e	T	3.0	2014/03/04	
04B	Ni5Tan_T30f	T	6.0	2014/03/06	
04C	Ni5Tan_T20c	T	3.0	2014/03/10	
04D	Ni5Tan_T20d	T	6.0	2014/03/11	
04E	Ni5Tan_T20e	T	3.0	2014/03/12	Tilted towards R
04F	Ni5Tan_T20f	T	6.0	2014/03/13	Tilted towards R
050	Ni5Tan_T40g	T	1.5	2014/03/14	
051	Ni5Tan_T30g	T	1.5	2014/03/17	Tilted towards R
052	Ni5Tan_T30h	T	6.0	2014/03/18	Tilted towards R
053	Ni5Tan_A20a	A	3.0	2014/04/01	
054	Ni5Tan_A20b	A	6.0	2014/04/02	
055	Ni5Tan_A30a	A	3.0	2014/04/03	
056	Ni5Tan_A30b	A	6.0	2014/04/04	
057	Ni4BC26_T3a	V	6.0	2014/05/08	C_V measurement
058	Ni4BC26_T3b	V	6.0	2014/05/09	C_V measurement
059	Ni4BC26_T3c	V	6.0	2014/05/12	C_V measurement
05A	Ni5Ten_T30a	T	3.0	2014/07/14	
05B	Ni16Tan_A5a	A	6.0	2014/09/11	
05C	Ni16Tan_A5b	A	3.0	2014/09/12	
05D	Ni16Tan_A5c	A	1.5	2014/09/15	
05E	Ni16Tan_T100a	T	6.0	2014/09/16	
05F	Ni16Tan_T100b	T	3.0	2014/09/17	
060	Ni16Tan_T100c	T	1.5	2014/09/26	
061	Ni16Tan_T100d	T	5.0	2014/09/29	
062	Ni16Tan_T100e	T	2.5	2014/09/30	
063	Ni16Tan_T70a	T	6.0	2014/10/01	
064	Ni16Tan_T70b	T	3.0	2014/10/02	
065	Ni16Tan_T70c	T	1.5	2014/10/03	
066	Ni16Tan_T35a	T	6.0	2014/10/06	
067	Ni16Tan_T35b	T	3.0	2014/10/07	
068	Ni16Tan_T35c	T	1.5	2014/10/08	
069	Ni16CR_T100a	T	6.0	2014/10/10	
06A	Ni16CR_T100b	T	3.0	2014/10/13	

N°	Label	Or.	φ /K min^{-1}	Date	Comments
06B	Ni16CR_T100c	T	1.5	2014/10/14	
06C	Ni16CR_T100d	T	5.0	2014/10/15	
06D	Ni4BC26_T3d	V	1.5	2014/10/22	
06E	Ni4BC26_T3e	V	3.0	2014/10/23	
06F	Ni4BC26_T3f	V	6.0	2014/10/24	
070	Ni4BC26_T3g	V	3.0	2014/10/27	
071	Ni16Tan_T70d	T	5.0	2014/10/28	
072	Ni16Tan_T35d	T	5.0	2014/10/29	
073	Ni16Tan_T100f	T	1.5	2014/10/30	
074	Ni16CR_T70a	T	6.0	2014/11/04	
075	Ni16CR_T70b	T	5.0	2014/11/06	
076	Ni16CR_T70c	T	3.0	2014/11/07	
077	Ni16CR_T70d	T	1.5	2014/11/10	
078	Al1CR_T0.6a	V	1.5	2014/11/14	Data corrupted
079	Al1CR_T0.6b	V	3.0	2014/11/17	Aluminum
07A	Al1CR_T0.6c	V	5.0	2014/11/18	Aluminum
07B	Al1CR_T0.6d	V	6.0	2014/11/19	Aluminum
07C	Al1CR_T0.6e	V	1.5	2014/11/20	Aluminum
07D	Al1CR_R0.6a	E	5.0	2014/11/21	Aluminum
07E	Al1CR_R0.6b	E	1.5	2014/11/24	Aluminum
07F	Al1CR_R0.6c	E	3.0	2014/11/26	Aluminum
080	Al1CR_R0.6d	E	6.0	2014/11/27	Aluminum
081	Ni16Tan_T100g	T	2.5	2014/11/28	
082	Ni16Tan_T100h	T	3.0	2014/12/01	
083	Ni16Tan_T100i	T	5.0	2014/12/02	
084	Ni16Tan_T100j	T	6.0	2014/12/03	
085	Ni16CR_T35a	T	3.0	2014/12/03	
086	Ni16CR_T35b	T	6.0	2014/12/04	
087	Ni5Tan_T40d	T	5.0	2014/12/04	
088	Ni5Tan_T40h	T	5.0	2014/12/05	
089	Ni5Tan_T30d	T	5.0	2014/12/05	
08A	Ni16Tan_T100k	T	3.75	2014/12/09	
08B	Ni16Tan_T100l	T	4.0	2014/12/10	5 s Acquisition rate
08C	Ni16Tan_T100m	T	4.5	2014/12/10	4 s Acquisition rate

N°	Label	Or.	φ /K min^{-1}	Date	Comments
08D	Ni16Tan_T100n	T	10.0	2014/12/16	
08E	Ni16Tan_T100o	T	1.5	2014/12/17	Bar-shaped Base
08F	Ni16Tan_T100p	T	3.0	2014/12/18	Bar-shaped Base
090	Ni25CR_A1a	N	1.5	2015/01/27	
091	Ni25CR_A1b	N	3.0	2015/01/28	
092	Ni25CR_A1c	N	6.0	2015/01/28	
093	Ni25CR_T1a	E	1.5	2015/01/29	
094	Ni25CR_T1b	E	3.0	2015/01/30	
095	Ni25CR_T1c	E	6.0	2015/01/30	
096	Ni4BC_N3e	N	2.5	2015/02/04	
097	Ni4BC_N3f	N	5.0	2015/02/04	
098	Ni10NTen_A20b	A	1.5	2015/02/05	
099	Ni10NTen_A20c	A	6.0	2015/02/06	
09A	Ni1CR_N1a	N	1.5	2015/04/27	
09B	Ni1CR_N1b	N	2.5	2015/04/28	
09C	Ni1CR_N1c	N	3.0	2015/04/29	
09D	Ni1CR_N1d	N	5.0	2015/04/30	
09E	Ni1CR_N1e	N	6.0	2015/04/30	
09F	Ni1CR_T1a	V	1.5	2015/05/04	
0A0	Ni1CR_T1b	V	2.5	2015/05/05	
0A1	Ni1CR_T1c	V	3.0	2015/05/06	
0A2	Ni1CR_T1d	V	5.0	2015/05/07	
0A3	Ni1CR_T1e	V	6.0	2015/05/07	
0A4	Ni1CR_R1a	E	1.5	2015/05/21	
0A5	Ni1CR_R1b	E	2.5	2015/05/22	
0A6	Ni1CR_R1c	E	3.0	2015/05/26	
0A7	Ni1CR_R1d	E	5.0	2015/05/27	
0A8	Ni1CR_R1e	E	6.0	2015/05/27	
0A9	Ni1CR_R1f	E	1.5	2015/06/09	
0AA	Ni1CR_R1g	E	2.5	2015/06/10	
0AB	Ni1CR_R1h	E	3.0	2015/06/11	
0AC	Ni1CR_R1i	E	5.0	2015/06/12	
0AD	Ni1CR_R1j	E	6.0	2015/06/12	
0AE	Ni1CR_N1f	N	1.5	2015/08/03	

N°	Label	Or.	φ /K min^{-1}	Date	Comments
0AF	Ni1CR_N1g	N	2.5	2015/08/04	
0B0	Ni1CR_N1h	N	3.0	2015/08/05	
0B1	Ni1CR_N1i	N	5.0	2015/08/06	
0B2	Ni1CR_N1j	N	6.0	2015/08/07	
0B3	Ni5BBa_T40a	T	1.5	2015/08/13	Bar-shaped Base
0B4	Ni5BBr_T40b	T	1.5	2015/08/14	Bar-shaped Base
0B5	Ni5BBp_T40c	T	3.0	2015/08/17	
0B6	Ni5BBa_T40d	T	3.0	2015/08/18	Bar-shaped Base
0B7	Ni5BBr_T40e	T	3.0	2015/08/19	Bar-shaped Base
0B8	Ni5BBa_T40f	T	6.0	2015/08/27	Bar-shaped Base
0B9	Ni5BBp_T40g	T	6.0	2015/08/28	
0BA	Ni5BBr_T40h	T	6.0	2015/08/31	Bar-shaped Base
0BB	Ni5BBr_T30a	T	3.0	2015/09/01	Bar-shaped Base
0BC	Ni5BBr_T30b	T	6.0	2015/09/02	Bar-shaped Base
0BD	Ni5BBa_T30c	T	3.0	2015/09/03	Bar-shaped Base
0BE	Ni5BBa_T30d	T	6.0	2015/09/04	Bar-shaped Base
0BF	Ni5TT_A30f	A	1.5	2015/09/08	
0C0	Ni5TT_A20g	A	1.5	2015/09/10	
0C1	Ni5TT_A12f	A	3.0	2015/09/11	
0C2	Ni5TT_A12g	A	6.0	2015/09/14	
0C3	Ni5TT_A20h	A	3.0	2015/09/15	
0C4	Ni5TT_A30g	A	3.0	2015/09/23	
0C5	Ni5TT_A30h	A	6.0	2015/09/24	Data corrupted
0C6	Ni5TT_A30i	A	6.0	2015/10/01	
0C7	Ni5TT_A20i	A	6.0	2015/10/02	
0C8	Ni5TT_T30e	T	3.0	2015/10/05	
0C9	Ni5TT_T30f	T	6.0	2015/10/06	
0CA	Ni5Mod_A30a	A	1.5	2015/10/07	
0CB	Ni5Mod_A30b	A	3.0	2015/10/08	
0CC	Ni5Mod_A30c	A	6.0	2015/10/09	
0CD	Ni5Mod_A30d	A	1.5	2015/10/12	
0CE	Ni5Mod_A30e	A	3.0	2015/10/13	
0CF	Ni5Mod_A30f	A	6.0	2015/10/14	
0D0	Ni5Mod_R30a	R	1.5	2015/10/15	

N°	Label	Or.	φ /K min^{-1}	Date	Comments
0D1	Ni5Mod_R30b	R	3.0	2015/10/16	
0D2	Ni5Mod_R30c	R	6.0	2015/10/19	
0D3	Ni5Mod_R30d	R	3.0	2015/10/21	
0D4	Ni5Mod_T40a	T	3.0	2015/11/05	
0D5	Ni5Mod_T30a	T	3.0	2015/11/06	Annealed at 370 K
0D6	Ni5Mod_T40b	T	3.0	2015/11/09	Annealed at 430 K
0D7	Ni5Mod_T30b	T	3.0	2015/11/11	Annealed at 490 K
0D8	Ni12A_T9a	V	1.5	2015/11/23	
0D9	Ni12A_T9b	V	3.0	2015/11/24	
0DA	Ni12A_T9c	V	6.0	2015/11/25	
0DB	Ni12A_E9a	E	1.5	2015/11/26	
0DC	Ni12A_E9b	E	3.0	2015/11/27	
0DD	Ni12A_E9c	E	6.0	2015/11/30	
0DE	Ni12A_N9a	N	1.5	2015/12/01	
0DF	Ni12A_N9b	N	3.0	2015/12/02	
0E0	Ni12A_N9c	N	6.0	2015/12/03	
0E1	Ni12BC_T9a	V	1.5	2015/12/10	
0E2	Ni12BC_T9b	V	3.0	2015/12/11	
0E3	Ni12BC_T9c	V	6.0	2015/12/14	
0E4	Ni12BC_E9a	E	1.5	2015/12/15	Data corrupted
0E5	Ni12BC_E9b	E	1.5	2015/12/16	
0E6	Ni12BC_E9c	E	3.0	2015/12/17	
0E7	Ni12BC_E9d	E	6.0	2015/12/18	
0E8	Ni12BC_N9a	N	1.5	2016/01/11	
0E9	Ni12BC_N9b	N	3.0	2016/01/12	
0EA	Ni12BC_N9c	N	6.0	2016/01/13	
0EB	Ti4A_N3a	N	3.0	2016/01/19	Titanium
0EC	Ti4A_N3b	N	1.5	2016/01/20	Titanium
0ED	Ti4A_N3c	N	6.0	2016/01/21	Titanium
0EE	Ti4A_T3a	V	3.0	2016/01/22	Titanium
0EF	Ti4A_T3b	V	6.0	2016/01/25	Titanium
0F0	Ti4A_E3a	E	3.0	2016/01/26	Titanium
0F1	Ti4A_E3b	E	6.0	2016/01/27	Titanium
0F2	Ni12A_T9d	V	2.5	2016/02/08	

N°	Label	Or.	φ /K min^{-1}	Date	Comments
0F3	Ni12A_T9e	V	5.0	2016/02/09	
0F4	Ni12A_E9d	E	2.5	2016/02/10	
0F5	Ni12A_E9e	E	5.0	2016/02/11	
0F6	Ni12A_N9d	N	2.5	2016/02/12	
0F7	Ni12A_N9e	N	5.0	2016/02/15	
0F8	Ni12BC_T9d	V	2.5	2016/02/16	
0F9	Ni12BC_T9e	V	5.0	2016/02/17	
0FA	Ni12BC_E9e	E	2.5	2016/02/18	
0FB	Ni12BC_E9f	E	5.0	2016/02/19	
0FC	Ni12BC_N9d	N	2.5	2016/02/23	
0FD	Ni12BC_N9e	N	5.0	2016/02/24	
0FE	Ni5TT_A20j	A	1.5	2016/03/03	
0FF	Ni5TT_A20k	A	3.0	2016/03/04	
100	Ni5TT_A20l	A	6.0	2016/03/07	
101	Ni5TT_A30j	A	3.0	2016/03/29	Annealed at 490 K
102	Ni5TT_A30k	A	3.0	2016/03/30	Annealed at 770 K
103	Ni5ND_T40a	T	3.0	2016/07/26	Versus Ni5ND_A40a
104	Ni12BC_E9g	E	3.0	2016/07/27	Versus Ni12BC_T9f

The following pages contain a complete collection of the results from the difference dilatometry measurements which were used for calculations. The color of the curves indicates the heating rate: blue indicates a heating rate of $1.5\,\mathrm{K\,min^{-1}}$, yellow of $2.5\,\mathrm{K\,min^{-1}}$, green of $3.0\,\mathrm{K\,min^{-1}}$, red of $5.0\,\mathrm{K\,min^{-1}}$, and black of $6.0\,\mathrm{K\,min^{-1}}$. Other rarely used heating rates are designated by different colors.

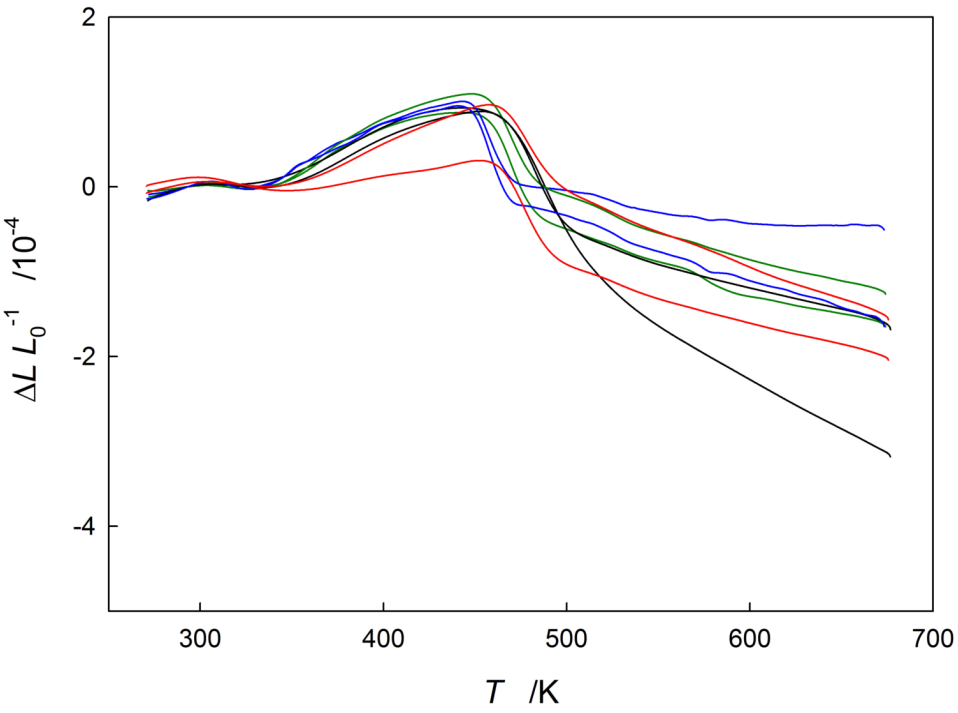

Figure 6.1: Ni5Tan, HPT, tangential, $\varepsilon = 40$. Dilatometry of samples 03E (green), 045 (black), 046 (blue), 048 (green), 049 (black), 050 (blue), 087 and 088 (red).

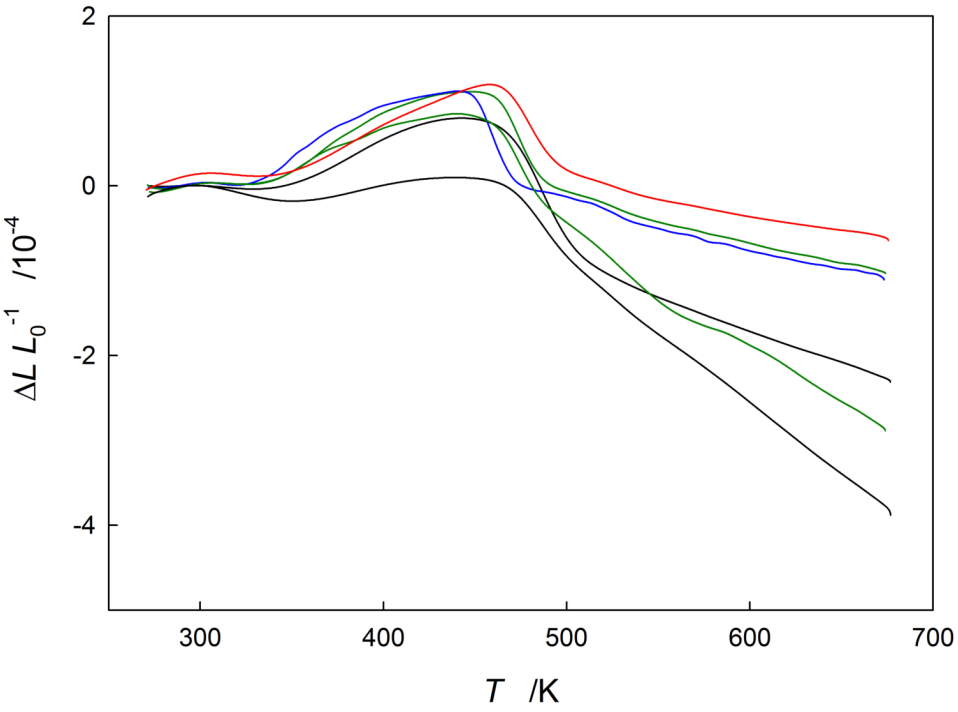

Figure 6.2: Ni5Tan, HPT, tangential, $\varepsilon = 30$. Dilatometry of samples 03F (green), 044 (black), 047 (blue), 04A (green), 04B (black) and 089 (red).

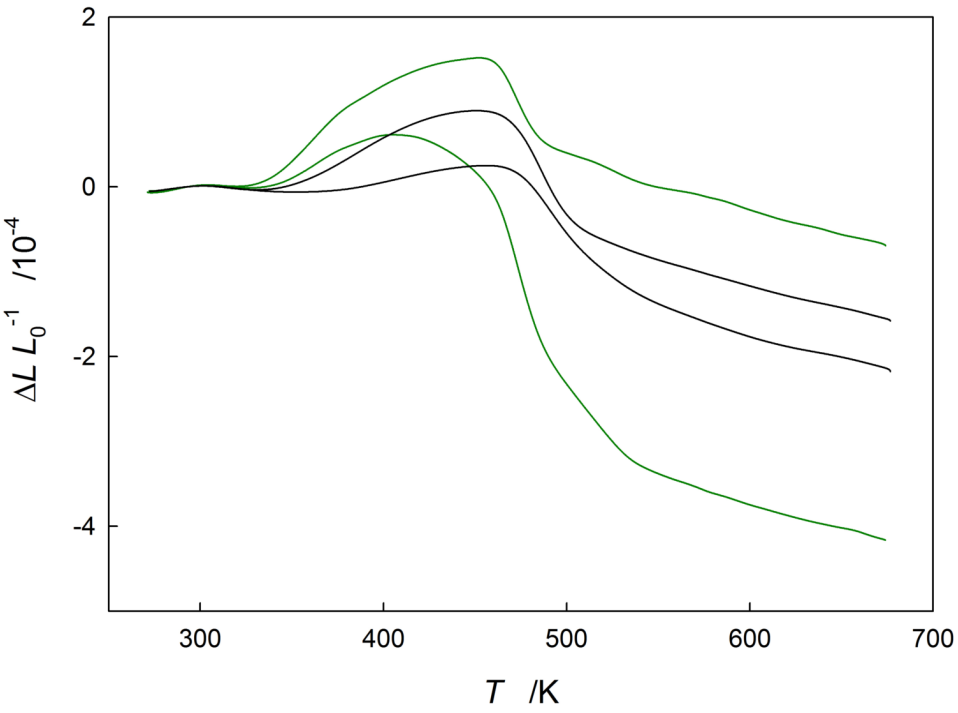

Figure 6.3: Ni5Tan, HPT, tangential, $\varepsilon = 20$. Dilatometry of samples 040 (green), 043 (black), 04C (green) and 04D (black).

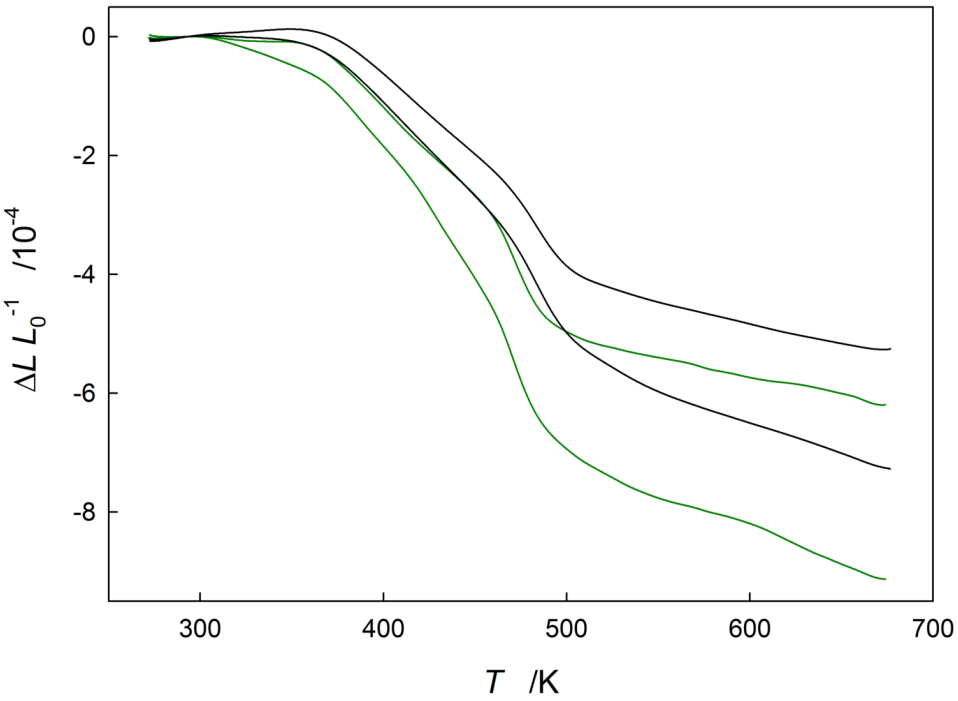

Figure 6.4: Ni5Tan, HPT, axial. Dilatometry of samples 053 (green), 054 (black), 055 (green) and 056 (black).

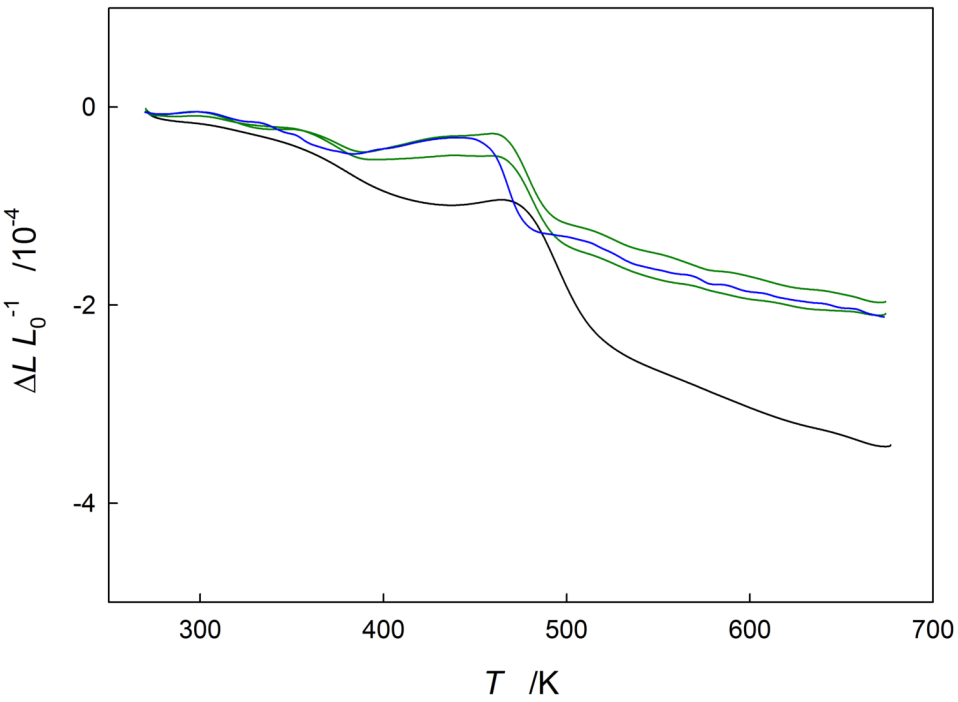

Figure 6.5: Ni10Ten, HPT, tangential, tensile straining. Dilatometry of samples 02C (green), 02D (black), 02E (green) and 02F (blue).

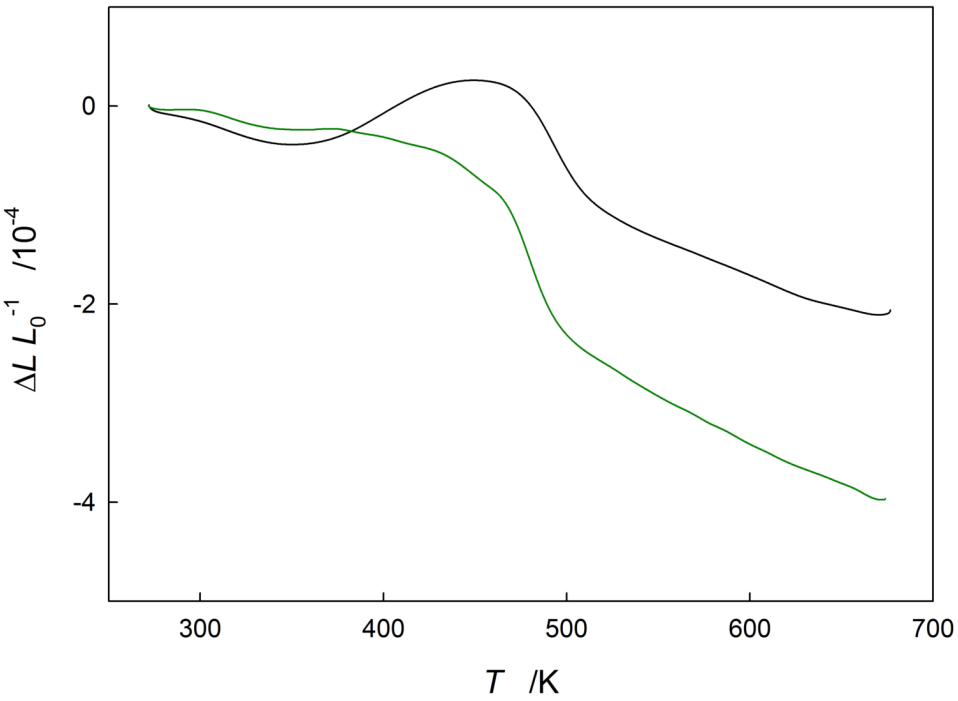

Figure 6.6: Ni10NTen, HPT, tangential, no tensile straining. Dilatometry of samples 030 (black) and 031 (green).

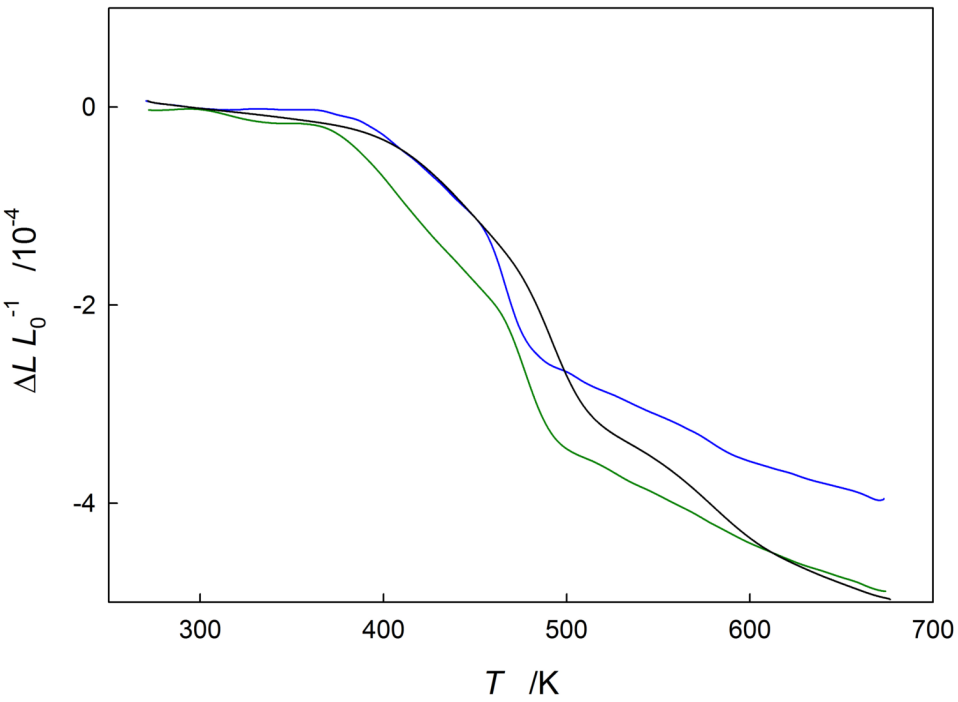

Figure 6.7: Ni10NTen, HPT, axial, no tensile straining. Dilatometry of samples 032 (green), 098 (blue) and 099 (black).

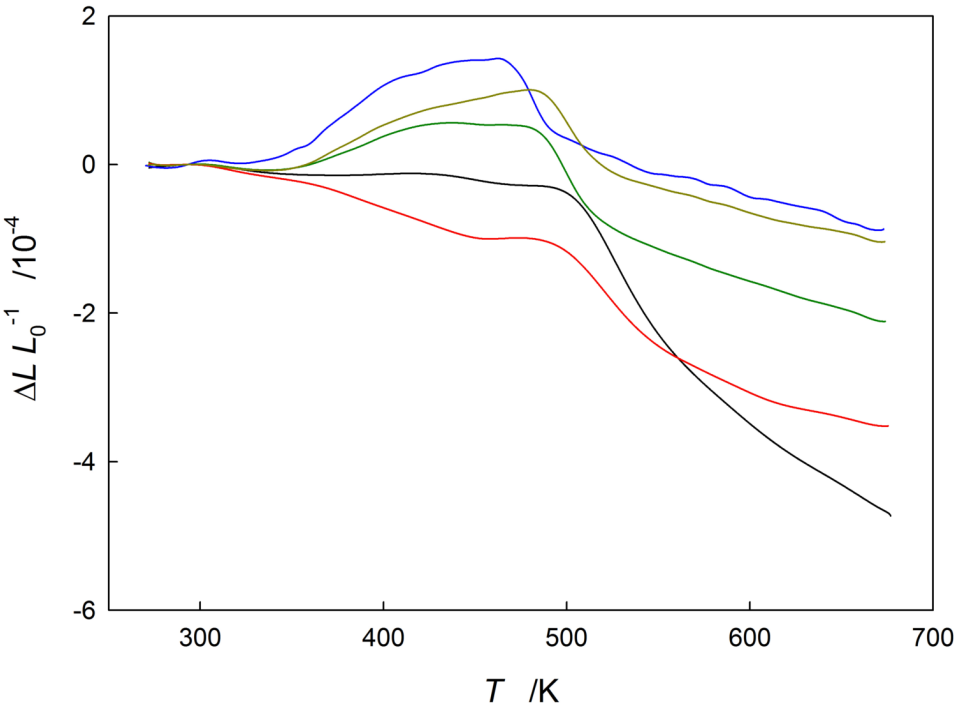

Figure 6.8: Ni16Tan, HPT, tangential, $\varepsilon = 100$. Dilatometry of samples 05E (black), 05F (green), 060 (blue), 061 (red) and 062 (yellow).

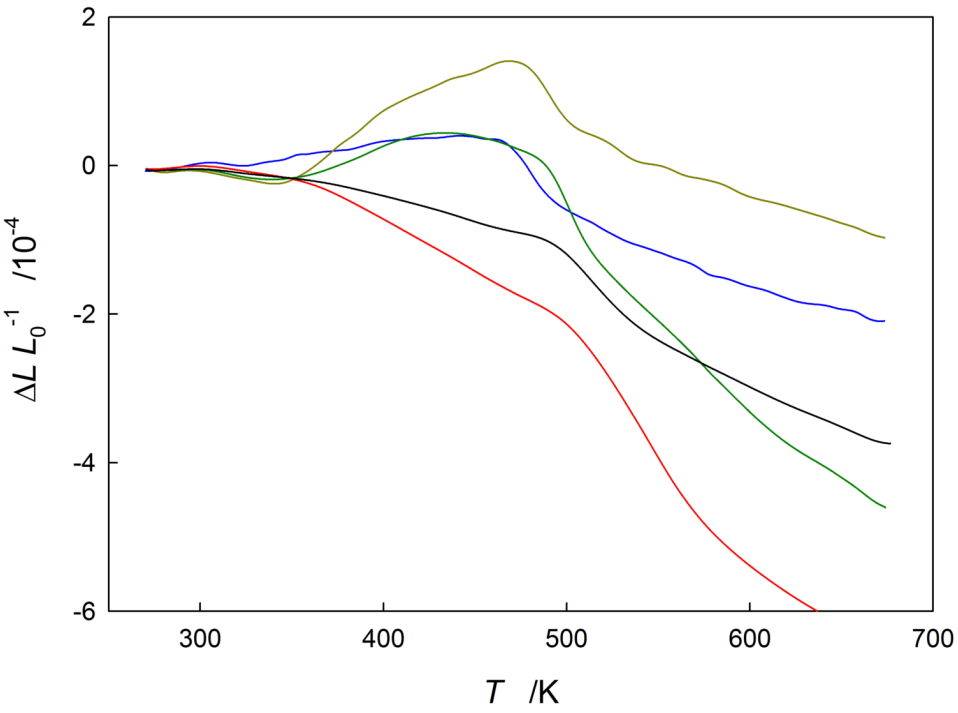

Figure 6.9: Ni16Tan, HPT, tangential, $\varepsilon = 100$. Dilatometry of samples 073 (blue), 081 (yellow), 082 (green), 083 (red) and 084 (black).

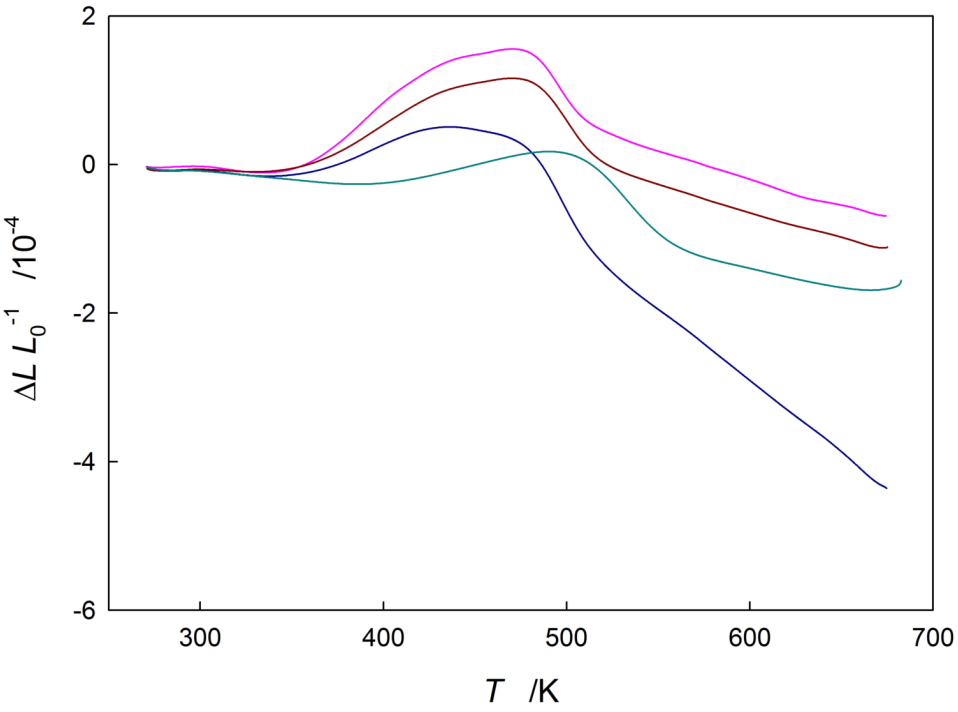

Figure 6.10: Ni16Tan, HPT, tangential, $\varepsilon = 100$. Dilatometry of samples 08A (pink), 08B (navy), 08C (purple) and 08D (cyan).

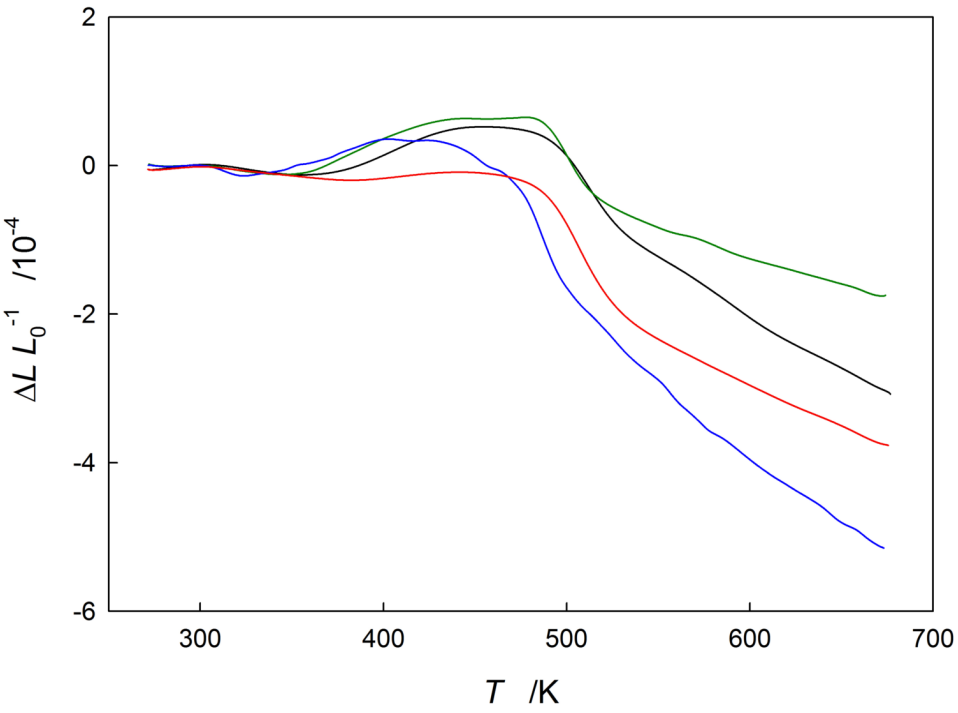

Figure 6.11: Ni16Tan, HPT, tangential, $\varepsilon = 70$. Dilatometry of samples 063 (black), 064 (green), 065 (blue) and 071 (red).

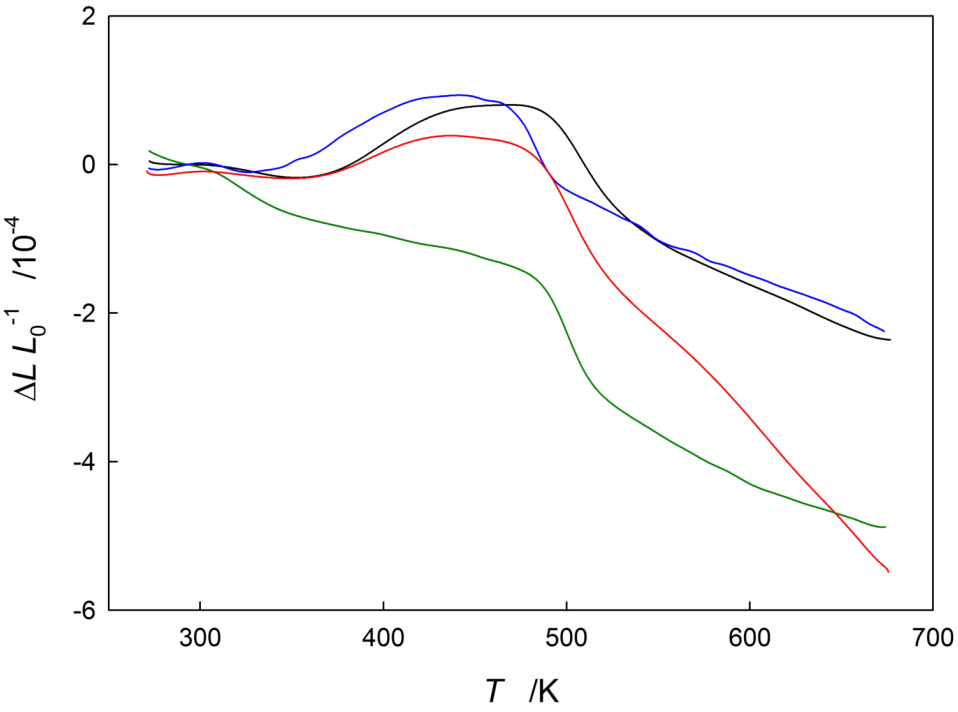

Figure 6.12: Ni16Tan, HPT, tangential, $\varepsilon = 35$. Dilatometry of samples 066 (black), 067 (green), 068 (blue) and 072 (red).

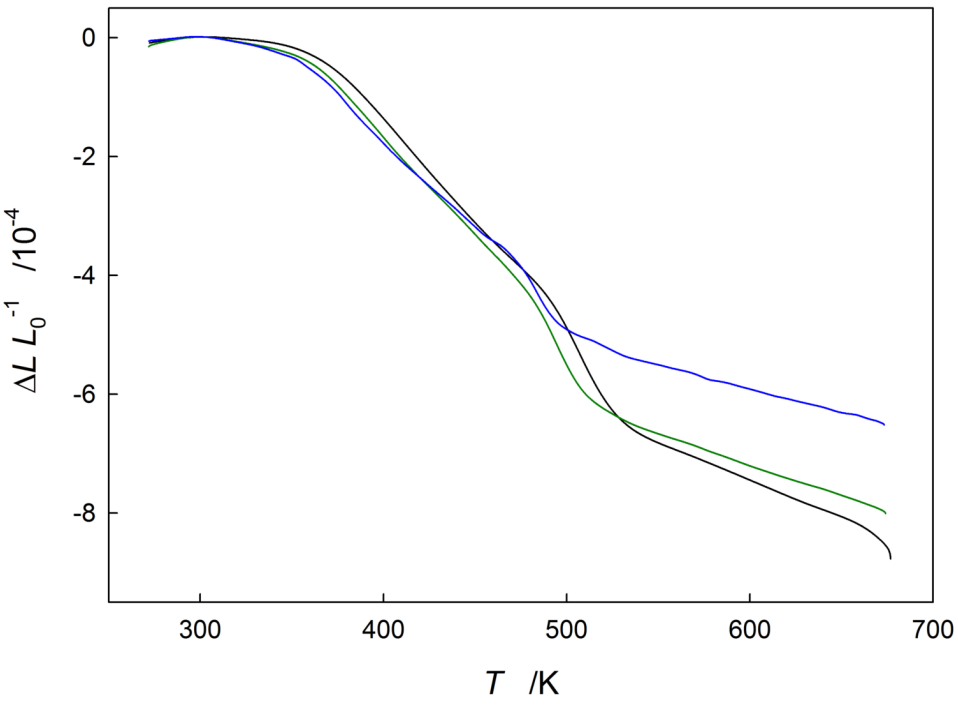

Figure 6.13: Ni16Tan, HPT, axial. Dilatometry of samples 05B (black), 05C (green) and 05D (blue).

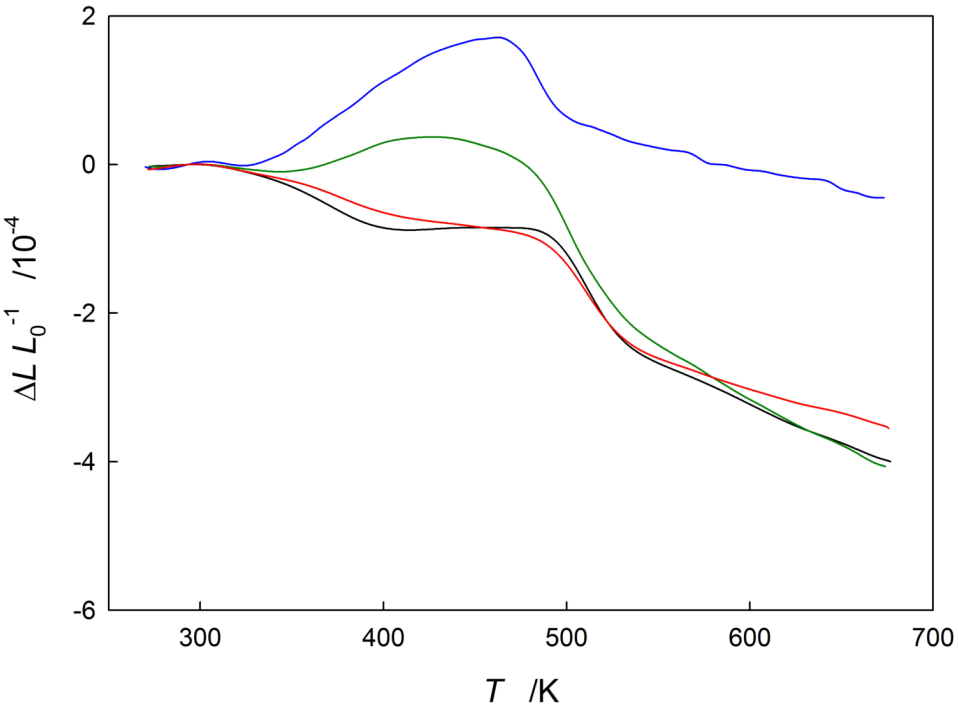

Figure 6.14: Ni16CR, HPT, tangential, cold rolling, $\varepsilon = 100$. Dilatometry of samples 069 (black), 06A (green), 06B (blue) and 06C (red).

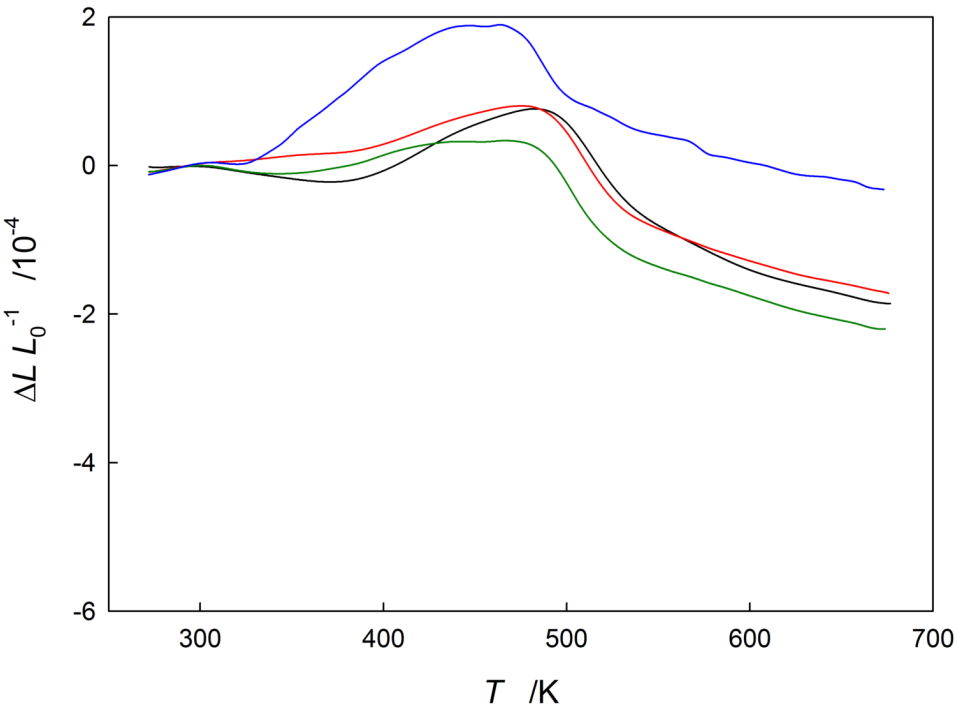

Figure 6.15: Ni16CR, HPT, tangential, cold rolling, $\varepsilon = 70$. Dilatometry of samples 074 (black), 075 (red), 076 (green) and 077 (blue).

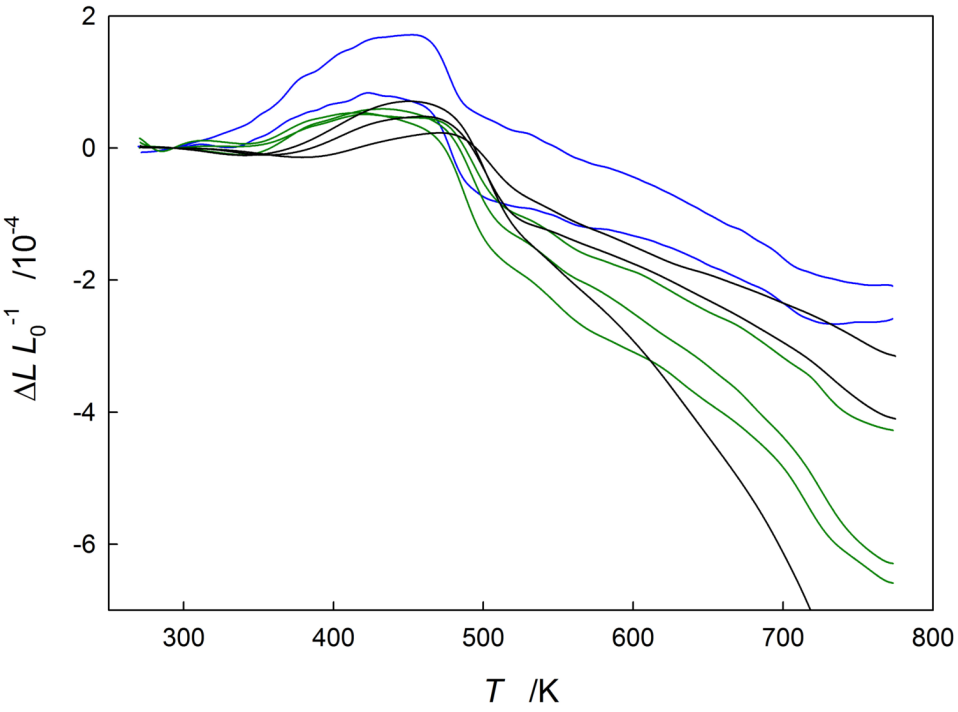

Figure 6.16: Ni5BB, HPT, bar-shaped base, $\varepsilon = 40$. Dilatometry of samples 0B3, 0B4 (blue), 0B5, 0B6, 0B7 (green), 0B8, 0B9 and 0BA (black).

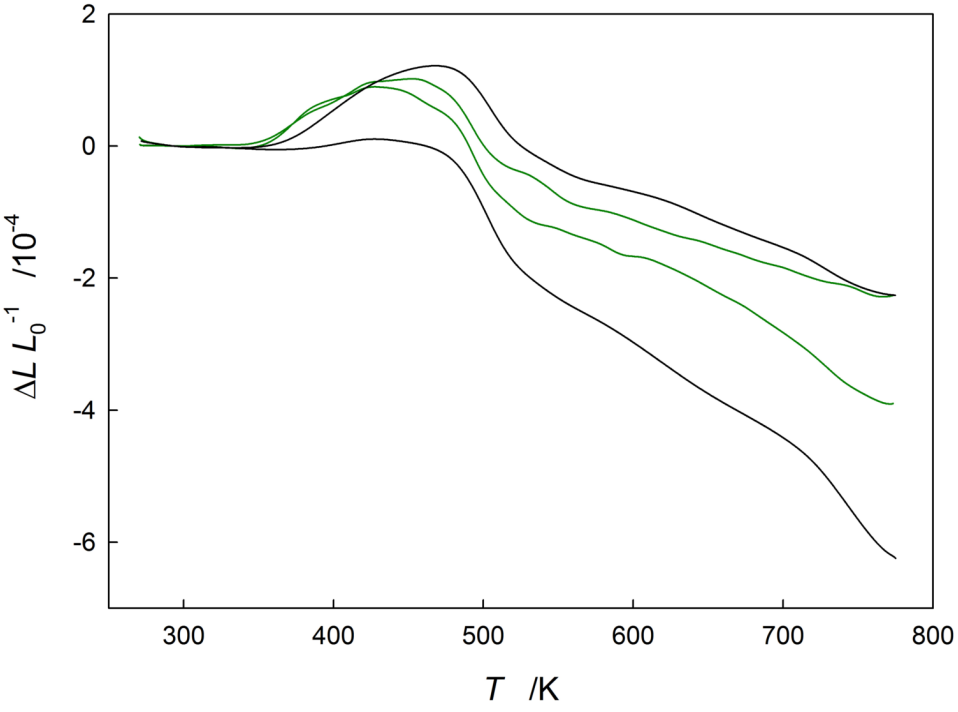

Figure 6.17: Ni5BB, HPT, bar-shaped base, $\varepsilon = 30$. Dilatometry of samples 0BB (green), 0BC (black), 0BD (green) and 0BE (black).

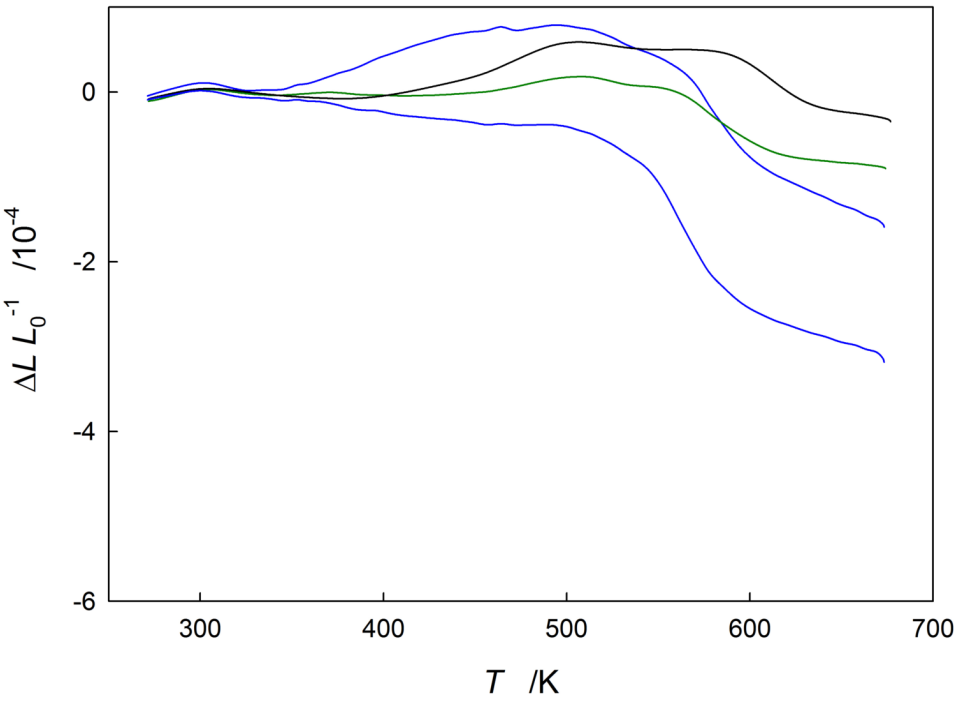

Figure 6.18: Ni4BC, ECAP, B_c4, extrusion. Dilatometry of samples 037 (blue), 03A (green), 03B (black) and 03C (blue).

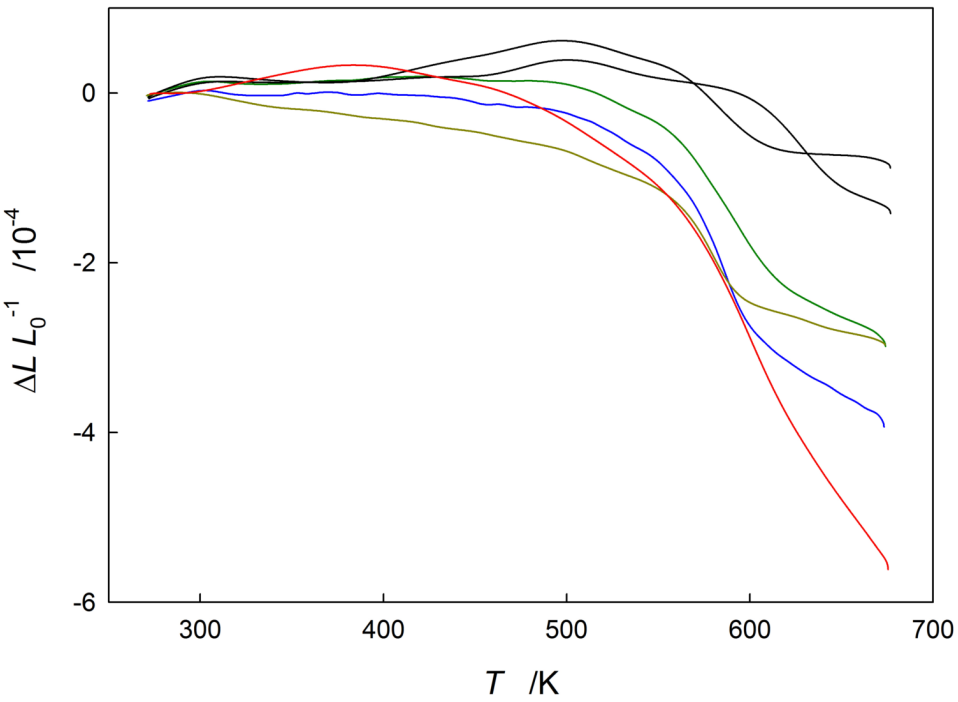

Figure 6.19: Ni4BC, ECAP, B_c4, normal. Dilatometry of samples 036 (blue), 038 (green), 039, 03D (black), 096 (yellow) and 097 (red).

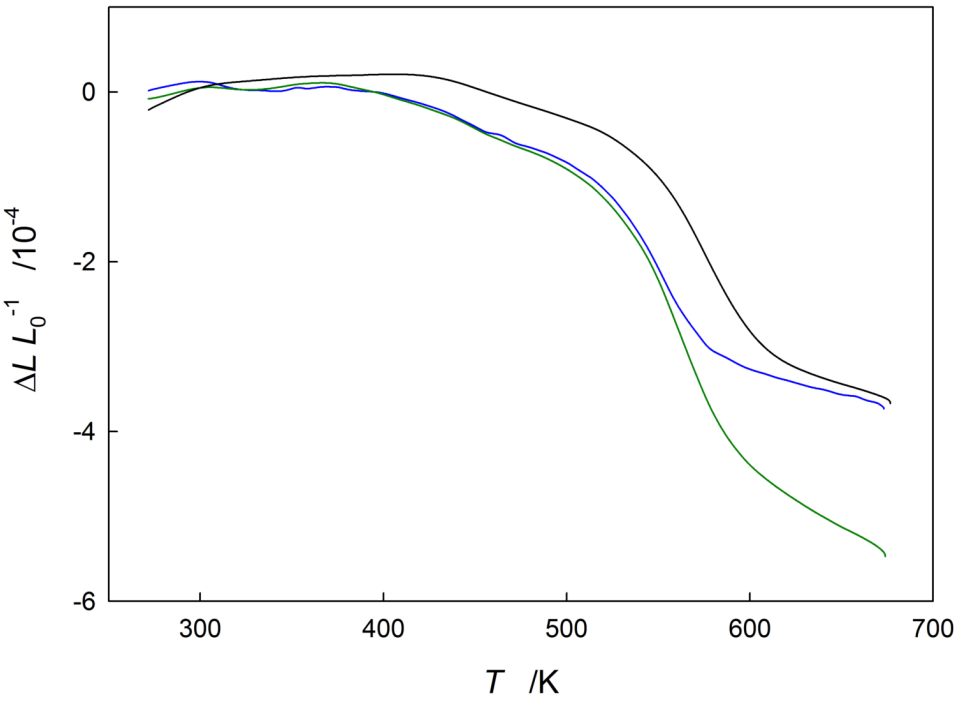

Figure 6.20: Ni4BC, ECAP, B_c4, transverse. Dilatometry of samples 033 (blue), 034 (green) and 035 (black).

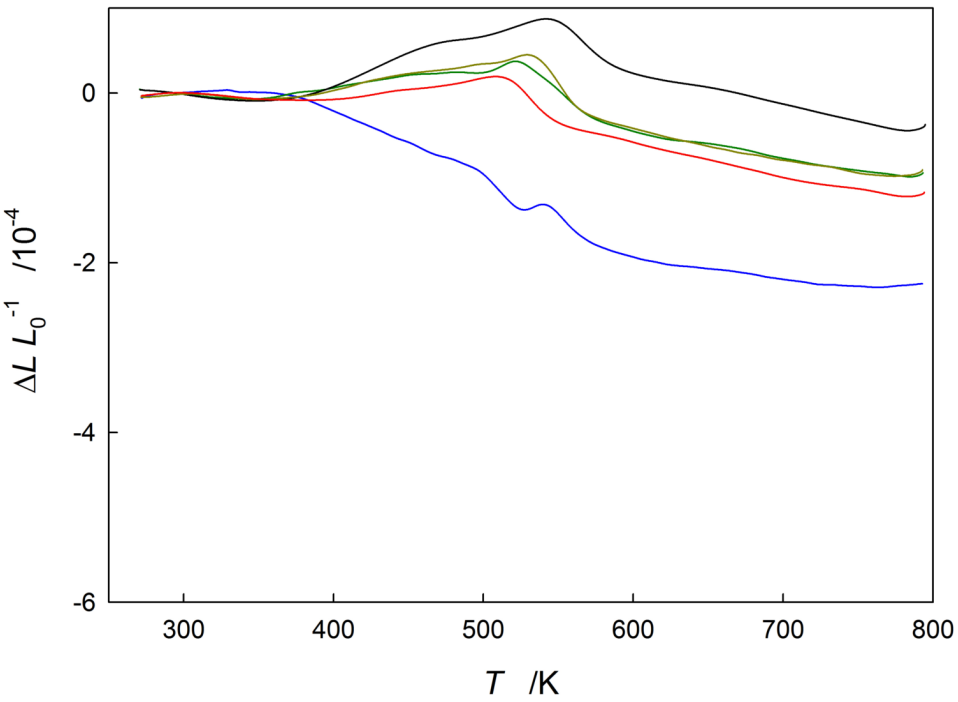

Figure 6.21: Ni12A, ECAP, A12, extrusion. Dilatometry of samples 0DB (blue), 0DC (green), 0DD (black), 0F4 (yellow) and 0F5 (red).

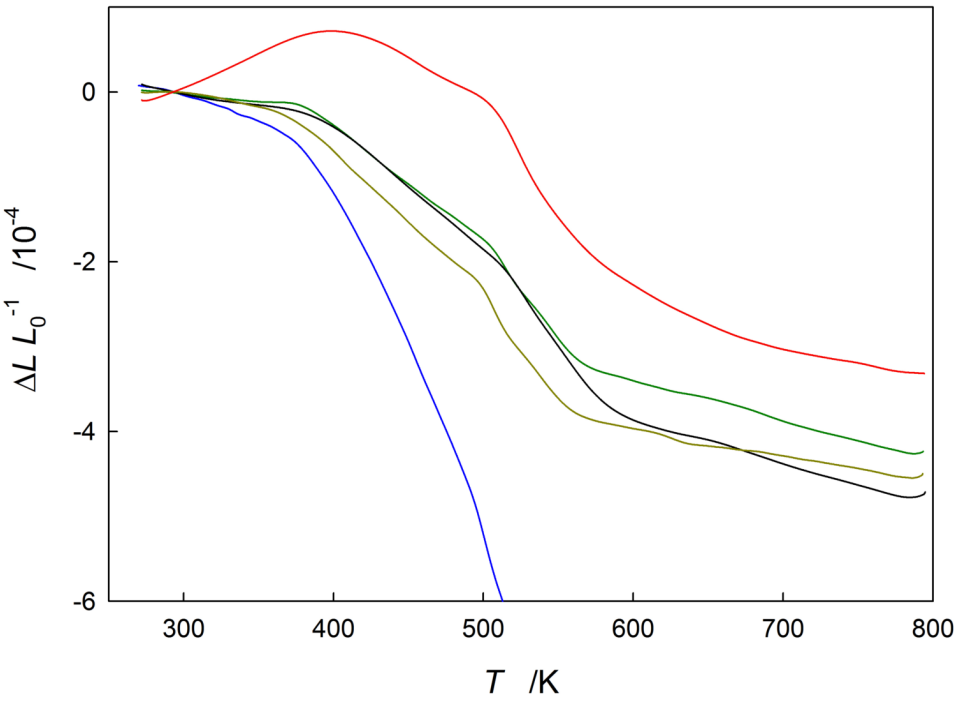

Figure 6.22: Ni12A, ECAP, A12, normal. Dilatometry of samples 0DE (blue), 0DF (green), 0E0 (black), 0F6 (yellow) and 0F7 (red).

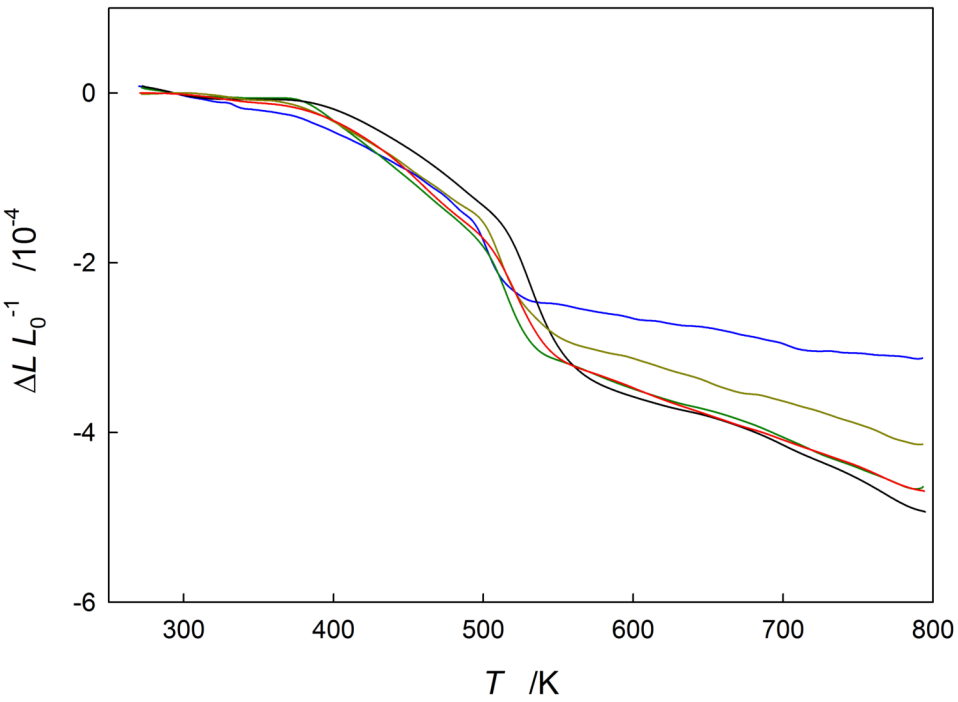

Figure 6.23: Ni12A, ECAP, A12, transverse. Dilatometry of samples 0D8 (blue), 0D9 (green), 0DA (black), 0F2 (yellow) and 0F3 (red).

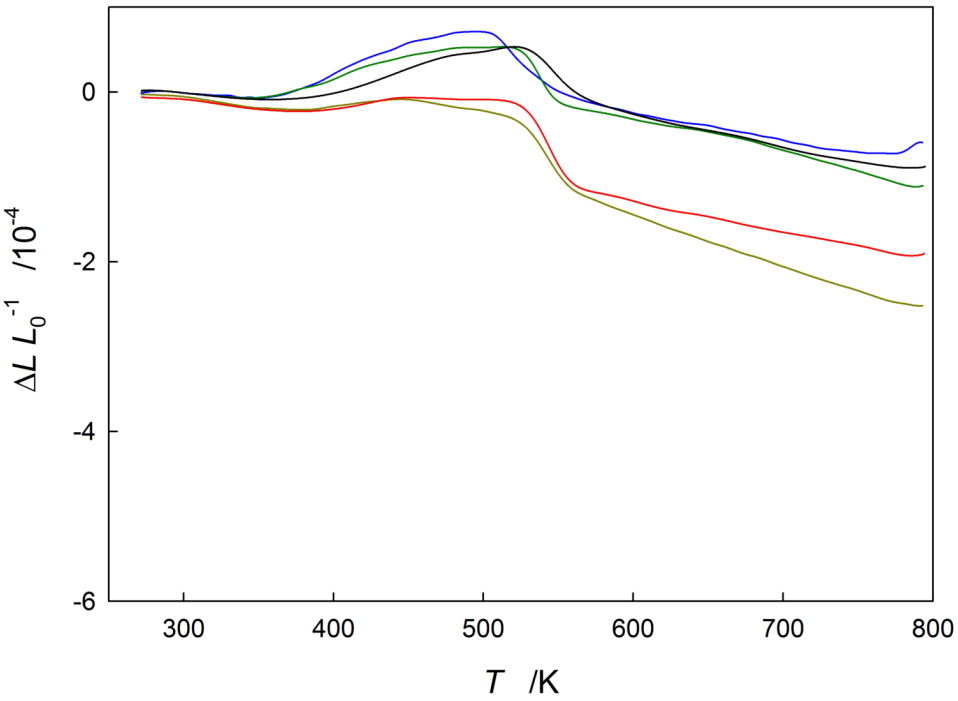

Figure 6.24: Ni12BC, ECAP, B_c12, extrusion. Dilatometry of samples 0E5 (blue), 0E6 (green), 0E7 (black), 0FA (yellow) and 0FB (red).

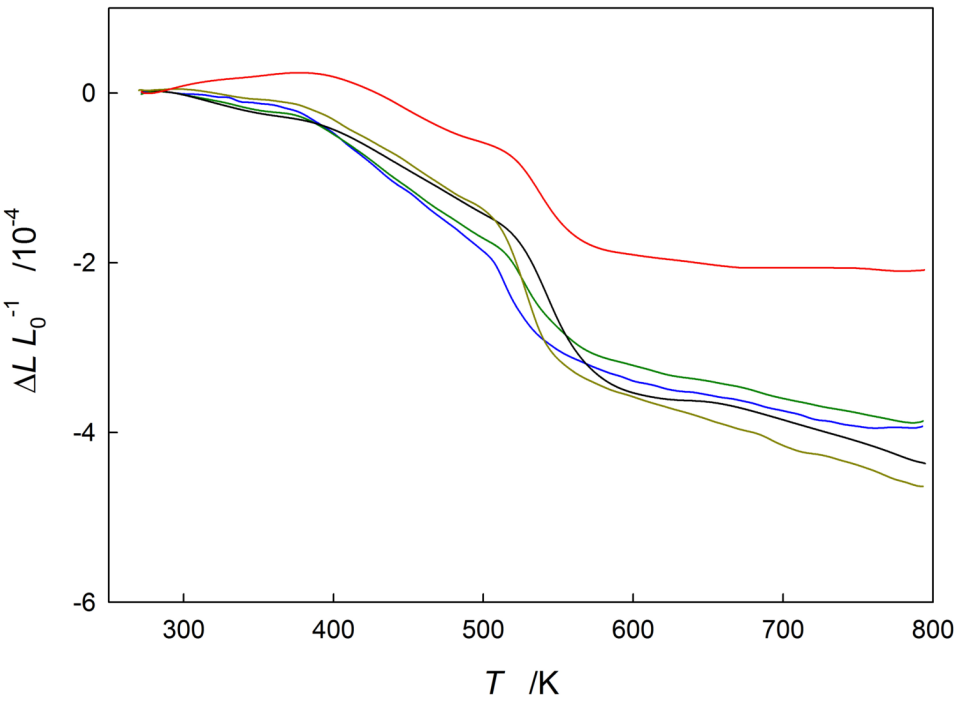

Figure 6.25: Ni12BC, ECAP, B_c12, normal. Dilatometry of samples 0E8 (blue), 0E9 (green), 0EA (black), 0FC (yellow) and 0FD (red).

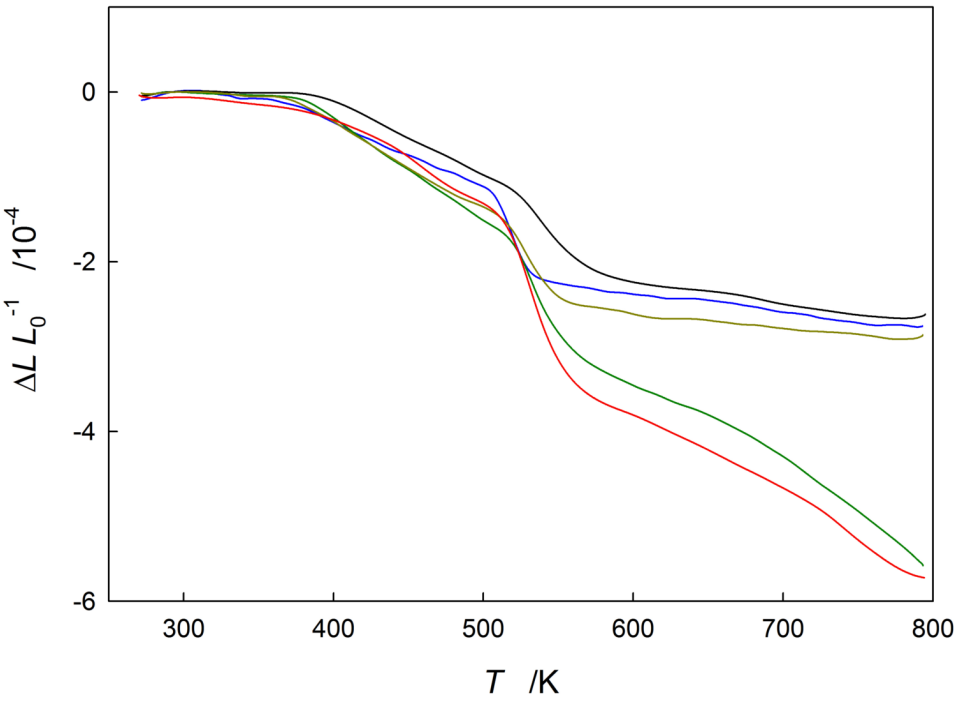

Figure 6.26: Ni12BC, ECAP, B_c12, transverse. Dilatometry of samples 0E1 (blue), 0E2 (green), 0E3 (black), 0F8 (yellow) and 0F9 (red).

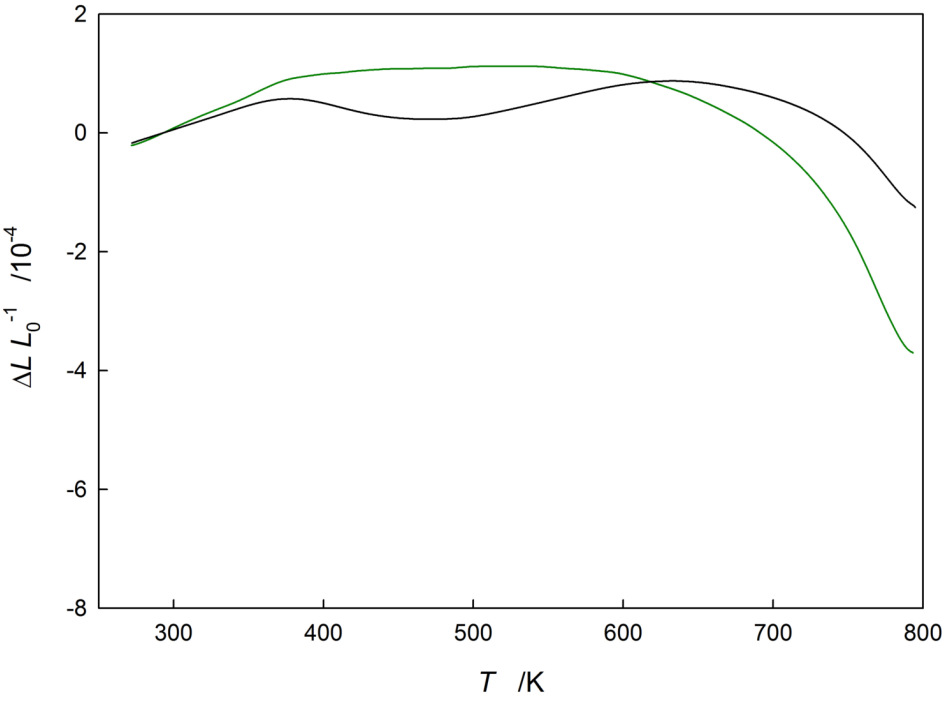

Figure 6.27: Ti4A, Titanium, ECAP, A4, extrusion. Dilatometry of samples 0F0 (green) and 0F1 (black).

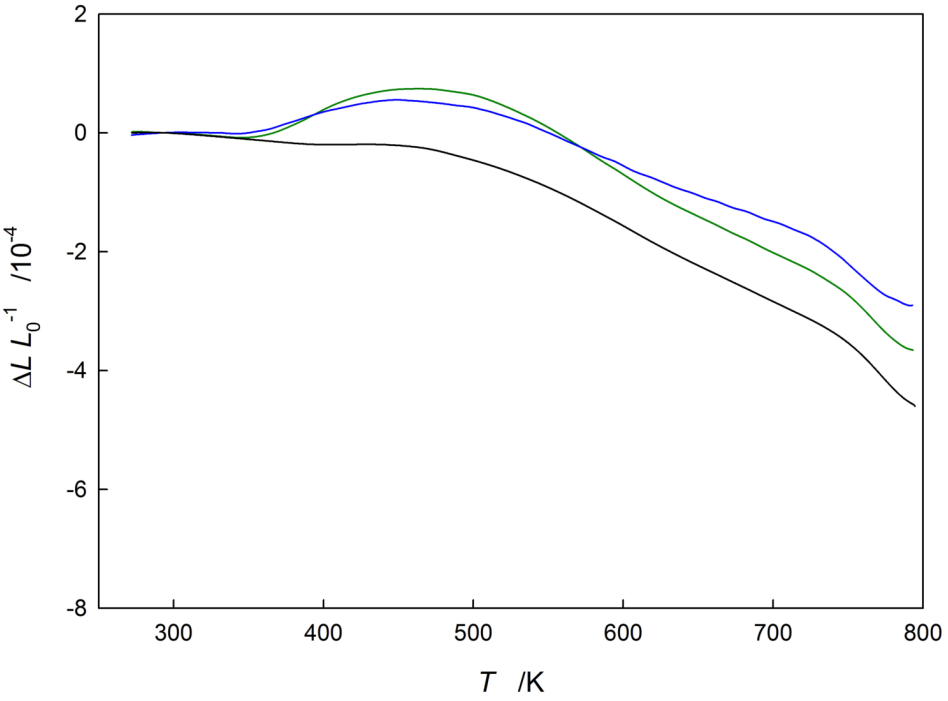

Figure 6.28: Ti4A, Titanium, ECAP, A4, normal. Dilatometry of samples 0EB (green), 0EC (blue) and 0ED (black).

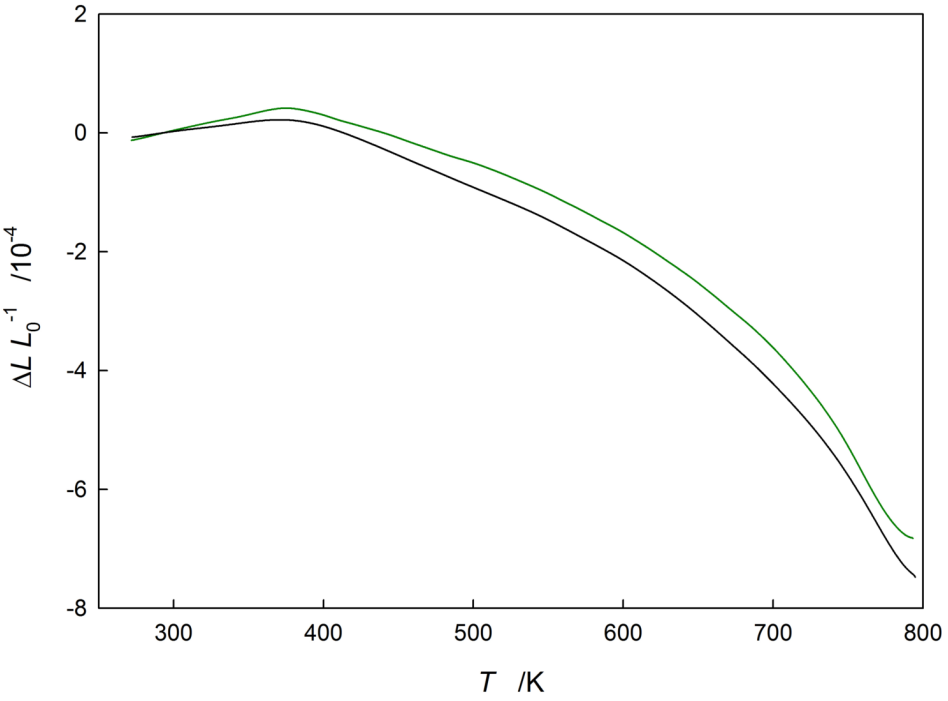

Figure 6.29: Ti4A, Titanium, ECAP, A4, transverse. Dilatometry of samples 0EE (green) and 0EF (black).

The following list contains the length changes derived from the difference dilatometry results shown above. The list contains the ongoing, hexadecimal numbering, the orientation (Or.), the heating rate φ, the length changes during the stages A, B and C, and the overall length change. For the definition of the orientations see the beginning of the section as well as figures 3.6 and 3.7.

N°	Or.	ε	φ /K min^{-1}	$\frac{\Delta L}{L_0}\Big\|_A$ /10^{-4}	$\frac{\Delta L}{L_0}\Big\|_B$ /10^{-4}	$\frac{\Delta L}{L_0}\Big\|_C$ /10^{-4}	$\frac{\Delta L}{L_0}$ /10^{-4}
Ni10Ten							
02C	T	20	3.00	-0.4964	-0.9086	-0.6849	-2.0899
02D	T	20	6.00	-1.0263	-1.3638	-1.0571	-3.4472
02E	T	20	3.00	-0.3507	-0.8806	-0.7867	-2.0180
02F	T	20	1.50	-0.3691	-0.9035	-0.9020	-2.1746
Ni10NTen							
030	T	20	6.00	0.2769	-1.3023	-1.0076	-2.0330
031	T	20	3.00	-0.5260	-1.7892	-1.6572	-3.9724
032	A	20	3.00	-1.4973	-1.9632	-1.4395	-4.9000
Ni4BC							
033	V	3	1.50	-0.8246	-1.3410	-1.6618	-3.8274
034	V	3	3.00	-0.9472	-2.6442	-1.9182	-5.5096
035	V	3	6.00	-0.3010	-2.4315	-0.8516	-3.5841
036	N	3	1.50	-0.2188	-0.6182	-3.1250	-3.9620
037	E	3	1.50	0.6970	-0.3706	-2.0019	-1.6755
038	N	3	3.00	0.0159	-1.0392	-2.0458	-3.0691
039	N	3	6.00	0.5036	-1.0914	-0.3823	-0.9701
03A	E	3	3.00	0.1931	-0.3737	-0.7015	-0.8821
03B	E	3	6.00	0.5770	-0.2570	-0.6771	-0.3571
03C	E	3	1.50	-0.3981	-0.6761	-2.1217	-3.1959
03D	N	3	6.00	0.2939	-0.4410	-1.3532	-1.5003
Ni5Tan							
03E	T	40	3.00	0.9860	-1.3690	-1.1502	-1.5332
03F	T	30	3.00	1.1600	-1.1604	-0.9647	-0.9651
040	T	20	3.00	0.4371	-2.7329	-1.8420	-4.1378

N°	Or.	ε	φ /K min^{-1}	$\frac{\Delta L}{L_0}\Big\|_{\mathrm{A}}$ /10^{-4}	$\frac{\Delta L}{L_0}\Big\|_{\mathrm{B}}$ /10^{-4}	$\frac{\Delta L}{L_0}\Big\|_{\mathrm{C}}$ /10^{-4}	$\frac{\Delta L}{L_0}$ /10^{-4}
041	T	12	3.00	1.0450	-1.2935	-1.4209	-1.6694
042	T	12	6.00	1.0445	-1.9162	-1.4806	-2.3523
043	T	20	6.00	0.9156	-1.5100	-0.9547	-1.5491
044	T	30	6.00	0.7954	-1.8068	-1.3005	-2.3119
045	T	40	6.00	0.9707	-2.0354	-2.0747	-3.1394
046	T	40	1.50	1.0575	-0.9632	-0.5125	-0.4182
047	T	30	1.50	1.1200	-1.1338	-1.0689	-1.0827
048	T	40	3.00	1.1057	-1.1653	-1.1590	-1.2186
049	T	40	6.00	1.0246	-1.5408	-1.0019	-1.5181
04A	T	30	3.00	0.8305	-1.2767	-2.4503	-2.8965
04B	T	30	6.00	0.2241	-1.3196	-2.6566	-3.7521
04C	T	20	3.00	1.4576	-1.0772	-1.0956	-0.7152
04D	T	20	6.00	0.2778	-1.2085	-1.1984	-2.1291
04E	T	20	3.00	0.4282	-1.4198	-1.2671	-2.2587
04F	T	20	6.00	-0.5125	-1.3972	-0.9125	-2.8222
050	T	40	1.50	1.0591	-1.1545	-1.4137	-1.5091
051	T	30	1.50	0.3832	-0.9432	-1.7226	-2.2826
052	T	30	6.00	-0.1772	-1.2781	-1.0312	-2.4865
053	A	30	3.00	-3.3839	-3.5419	-2.1829	-9.1087
054	A	30	6.00	-1.6983	-2.4202	-1.0593	-5.1778
055	A	40	3.00	-2.2953	-2.7042	-1.2224	-6.2219
056	A	40	6.00	-2.3808	-3.0444	-1.7960	-7.2212
Ni16Tan							
05B	A	5	6.00	-2.8566	-3.2126	-2.7151	-8.7843
05C	A	5	3.00	-2.7825	-2.6471	-2.5102	-7.9398
05D	A	5	1.50	-2.6951	-1.3664	-2.4388	-6.5003
05E	T	100	6.00	-0.1986	-0.8320	-3.7284	-4.7590
05F	T	100	3.00	0.5058	-0.6848	-1.9882	-2.1672
060	T	100	1.50	1.2780	-0.3955	-1.8231	-0.9406
061	T	100	5.00	-1.0209	-0.5288	-2.0621	-3.6118
062	T	100	2.50	0.7005	-0.0360	-1.7997	-1.1352
063	T	70	6.00	0.4662	-1.0867	-2.4949	-3.1154
064	T	70	3.00	0.5271	-0.4839	-1.8815	-1.8383
065	T	70	1.50	0.2547	-0.8552	-4.6043	-5.2048

N°	Or.	ε	φ /K min^{-1}	$\frac{\Delta L}{L_0}\Big\|_A$ /10^{-4}	$\frac{\Delta L}{L_0}\Big\|_B$ /10^{-4}	$\frac{\Delta L}{L_0}\Big\|_C$ /10^{-4}	$\frac{\Delta L}{L_0}$ /10^{-4}
066	T	35	6.00	0.6589	-1.1413	-1.9785	-2.4609
067	T	35	3.00	-1.2952	-1.1253	-2.6229	-5.0434
068	T	35	1.50	0.9095	-0.5391	-2.6305	-2.2601
Ni16CR							
069	T	100	6.00	-0.8685	-1.1859	-1.9639	-4.0183
06A	T	100	3.00	0.3512	-1.1880	-3.2365	-4.0733
06B	T	100	1.50	1.5055	-0.1972	-1.8039	-0.4956
06C	T	100	5.00	-0.8315	-0.9632	-1.7839	-3.5786
Ni16Tan							
071	T	70	5.00	-0.1001	-1.2623	-2.4144	-3.7768
072	T	35	5.00	0.3711	-1.5181	-4.3550	-5.5020
073	T	100	1.50	0.3111	-0.4575	-2.0120	-2.1584
Ni16CR							
074	T	70	6.00	0.4497	-0.5792	-1.7471	-1.8766
075	T	70	5.00	0.5687	-0.6463	-1.7113	-1.7889
076	T	70	3.00	0.2667	-0.5495	-1.9657	-2.2485
077	T	70	1.50	1.8014	-0.1870	-1.9619	-0.3475
Ni16Tan							
081	T	100	2.50	1.1043	-0.3687	-1.7504	-1.0148
082	T	100	3.00	0.4060	-0.9406	-4.1018	-4.6364
083	T	100	5.00	-1.3169	-1.1859	-4.1379	-6.6407
084	T	100	6.00	-0.7148	-1.0342	-2.0110	-3.7600
Ni16CR							
085	T	35	3.00	-0.3229	-0.7091	-2.0473	-3.0793
086	T	35	6.00	0.3856	-0.9415	-2.1061	-2.6620
Ni5Tan							
087	T	40	5.00	0.2614	-1.2824	-1.0287	-2.0497
088	T	40	5.00	0.9377	-1.0343	-1.3983	-1.4949
089	T	30	5.00	1.1410	-1.0100	-0.7283	-0.5973
Ni16Tan							
08A	T	100	3.75	1.3957	-0.6105	-1.4813	-0.6961
08B	T	100	4.00	0.5212	-1.3810	-3.4832	-4.3430
08C	T	100	4.50	1.0423	-0.7581	-1.3832	-1.0990
08D	T	100	10.00	-0.0173	-1.0119	-0.5405	-1.5697

N°	Or.	ε	φ /K min^{-1}	$\frac{\Delta L}{L_0}\Big\|_A$ /10^{-4}	$\frac{\Delta L}{L_0}\Big\|_B$ /10^{-4}	$\frac{\Delta L}{L_0}\Big\|_C$ /10^{-4}	$\frac{\Delta L}{L_0}$ /10^{-4}
08E	T	100	1.50	3.1684	-0.2686	-1.2879	1.6119
08F	T	100	3.00	0.1974	-0.6715	-1.9030	-2.3771
Ni4BC							
096	N	3	2.50	-0.7176	-0.8875	-1.4267	-3.0318
097	N	3	5.00	-0.5121	-1.9931	-3.2162	-5.7214
Ni10NTen							
098	A	20	1.50	-0.8598	-1.6108	-1.5362	-4.0068
099	A	20	3.00	-0.9716	-2.2757	-1.7439	-4.9912
Ni5BB							
0B3	T	40	1.50	0.7493	-0.9393	-1.8531	-2.0431
0B4	T	40	1.50	1.6624	-0.7404	-2.1914	-1.2694
0B5	T	40	3.00	0.4816	-1.3760	-2.9815	-3.8759
0B6	T	40	3.00	0.3790	-1.0080	-2.2245	-2.8535
0B7	T	40	3.00	0.2238	-1.8256	-2.9111	-4.5129
0B8	T	40	6.00	0.1026	-0.7522	-1.5219	-2.1715
0B9	T	40	6.00	0.5091	-1.4532	-1.6165	-2.5606
0BA	T	40	6.00	0.4990	-1.8689	-4.0328	-5.4027
0BB	T	30	3.00	0.6939	-1.3199	-1.9951	-2.6211
0BC	T	30	6.00	0.0228	-1.8235	-2.3508	-4.1515
0BD	T	30	3.00	1.0581	-0.9687	-1.6849	-1.5955
0BE	T	30	6.00	1.1673	-0.9953	-1.4430	-1.2710
Ni5TT							
0BF	A	30	1.50	-0.9260	-2.1583	-1.1664	-4.2507
0C0	A	20	1.50	-1.3125	-2.3271	-1.7856	-5.4252
0C1	A	12	3.00	-0.4053	-2.3357	-1.4453	-4.1863
0C2	A	12	6.00	-0.5196	-2.3397	-0.8018	-3.6611
0C3	A	20	3.00	-1.2635	-2.3378	-1.1269	-4.7282
0C4	A	30	3.00	-1.0509	-2.1668	-1.1999	-4.4176
0C6	A	30	6.00	-0.9532	-2.3750	-0.6041	-3.9323
0C7	A	20	6.00	-1.0982	-2.5011	-0.8030	-4.4023
0C8	T	30	3.00	0.3429	-1.1405	-0.6730	-1.4706
0C9	T	30	6.00	0.1299	-1.3456	-0.9936	-2.2093
Ni12A							
0D8	V	8	1.50	-1.5437	-1.0265	-0.3630	-2.9332

N°	Or.	ε	φ /K min^{-1}	$\frac{\Delta L}{L_0}\Big\|_A$ /10^{-4}	$\frac{\Delta L}{L_0}\Big\|_B$ /10^{-4}	$\frac{\Delta L}{L_0}\Big\|_C$ /10^{-4}	$\frac{\Delta L}{L_0}$ /10^{-4}
0D9	V	8	3.00	-1.8775	-1.5067	-0.5495	-3.9337
0DA	V	8	6.00	-1.5860	-2.0798	-0.3836	-4.0494
0DB	E	8	1.50	-0.7955	-0.5712	-0.6914	-2.0581
0DC	E	8	3.00	0.1930	-0.5512	-0.3560	-0.7142
0DD	E	8	6.00	0.6733	-0.4842	-0.2594	-0.0703
0DE	N	8	1.50	-4.7094	-3.6385	-2.0800	-10.4279
0DF	N	8	3.00	-1.7606	-1.5372	-0.4459	-3.7437
0E0	N	8	6.00	-2.1052	-1.8526	-0.3757	-4.3335
Ni12BC							
0E1	V	8	1.50	-0.9440	-1.2149	-0.2574	-2.4163
0E2	V	8	3.00	-1.4577	-1.7270	-0.7758	-3.9605
0E3	V	8	6.00	-1.0180	-1.1807	-0.1705	-2.3692
0E5	E	8	1.50	0.7248	-0.7013	-0.4851	-0.4616
0E6	E	8	3.00	0.5044	-0.7553	-0.3258	-0.5767
0E7	E	8	6.00	0.4973	-0.7700	-0.2850	-0.5577
0E8	N	8	1.50	-1.7271	-1.3089	-0.5965	-3.6325
0E9	N	8	3.00	-1.6995	-1.3709	-0.3918	-3.4622
0EA	N	8	6.00	-1.5472	-2.0067	-0.1988	-3.7527
Ni12A							
0F2	V	8	2.50	-1.4186	-1.5736	-0.5333	-3.5255
0F3	V	8	5.00	-1.8264	-1.5783	-0.5340	-3.9387
0F4	E	8	2.50	0.3818	-0.5862	-0.4612	-0.6656
0F5	E	8	5.00	0.2220	-0.7247	-0.3550	-0.8577
0F6	N	8	2.50	-2.2057	-1.6367	-0.3743	-4.2167
0F7	N	8	5.00	-0.0677	-2.0021	-0.7473	-2.8171
Ni12BC							
0F8	V	8	2.50	-1.3072	-1.2087	-0.2142	-2.7301
0F9	V	8	5.00	-1.3346	-2.3691	-0.7025	-4.4062
0FA	E	8	2.50	-0.1797	-1.0353	-0.6630	-1.8780
0FB	E	8	5.00	-0.0320	-1.1484	-0.3282	-1.5086
0FC	N	8	2.50	-1.3476	-2.0652	-0.5935	-4.0063
0FD	N	8	5.00	-0.6358	-1.2634	-0.1799	-2.0791
Ni5TT							
0FE	A	20	1.50	-1.4850	-2.0550	-1.2366	-4.7766

N°	Or.	ε	φ /K min^{-1}	$\frac{\Delta L}{L_0}\Big\|_{\mathrm{A}}$ /10^{-4}	$\frac{\Delta L}{L_0}\Big\|_{\mathrm{B}}$ /10^{-4}	$\frac{\Delta L}{L_0}\Big\|_{\mathrm{C}}$ /10^{-4}	$\frac{\Delta L}{L_0}$ /10^{-4}
0FF	A	20	3.00	-0.1023	-1.8284	-0.8703	-2.8010
100	A	20	6.00	-0.9411	-2.4398	-0.9346	-4.3155

Acknowledgments

The beginning of this work can be dated back to 2012 when I began the work on my diploma thesis at the Institute of Materials Physics in Graz. After finishing that thesis early 2013 I was offered the chance to continue my work at the institute seamlessly. That work eventually culminated in this very thesis finished early 2017. In these almost five years working at the Institute of Materials Physics I have received valuable support by a long list of people which I will try to name here.

Special thanks go to **Prof. Dr. Roland Würschum** who entrusted me with this project and supervised me while working at the Institute of Materials Physics.

Next I would like to thank **Prof. Dr. Reinhard Pippan** from the Erich Schmid Institute in Leoben for the ongoing cooperation which gives us easy access to an HPT facility. I'm also thankful for his invaluable insights into the nature of plastic deformation and ultrafine-grained metals.

I also give thanks to **Prof. Dr. Michael Zehetbauer** for reviewing this work and for being a member of the final examination board.

Furthermore, I'm very grateful to **Prof. Dr. Wolfgang Sprengel** for many fruitful discussions and especially for his support during the stressful measurements in Garching.

I would like to thank **Dr. Maciej Krystian** from the AIT Austrian Institute of Technology in Wiener Neustadt for the cooperation with our institute and access to their ECAP facility.

More in-house I'm grateful to **Univ.-Doz. Dr. Peter Pölt** from the Institute of Electron Microscopy and Nanoanalysis who granted me easy and unbureaucratic access to his electron microscopy instruments.

Also I want to give thanks to **Prof. Dr. Gerhard Wilde** from the Institute of Materials Physics in Münster for the cooperation which gave us access to nickel deformed by ECAP in the first place.

I'm especially grateful to **Dr. Michael Hofmann** from the FRM-II in Munich for his support in the neutron diffraction measurements, his trust and continued fruitful insight into the stress analysis by neutron diffraction.

Among my colleagues at the institute I would like to point out **Dipl.-Ing. Michael Neubauer** and **Dipl.-Ing. Peter Ranacher**. Both of whom I had the pleasure to co-supervise during their diploma theses on a numerical model of the dilatometry results and SQUID-measurements of ultrafine-grained nickel respectively.

Many thanks also go to my predecessor **Dr. Bernd Oberdorfer** who not only laid the groundwork for my work, but also continued to discuss interesting results whenever possible.

Moreover, I would like to thank **Dipl.-Ing. Eva-Maria Steyskal** from our institute for sparing time from her own work and working an a shared publication.

During his time at out institute **Dr. Martin Luckabauer** was always open for a quick discussion of my work or other, less related topics; for this I'm very grateful.

I would also like to thank all other members of the Institute of Materials Physics not explicitly mentioned above for the great time that I spent at the institute.

From the Erich Schmid Institute Leoben I'm also grateful to **Dr. Anton Hohenwarter** and **Dipl.-Ing. Peter Kutleša** for the preparation of specimens by HPT and many discussions about plastic deformation.

From the Institute of Electron Microscopy and Nanoanalysis I would like to thank **Sanja Simič** for letting me perform electron microscopy measurements in person or doing them whenever necessary. I would also like to thank **Dr. Stefan Mitsche** for the work he put into providing me with EBSD measurements.

From the Institute of Materials Physics Münster my thanks go to **Priv.-Doz. Dr. Sergiy Divinski** and **Dipl.-Phys. Simon Trubel** for providing a specimen prepared by ECAP and the EBSD measurements performed on it.

Finally, I want to thank my family and all of my friends for the support I received during my work on this thesis.

This study has been funded by the FWF Austrian Science Fund under the project numbered P25628-N20.